Doctoral Dissertation

Thermoelectric Properties of Nanostructured Eutectic Alloy Fabricated by Rapid Solidification

(急冷凝固法により作製されたナノ構造共晶合金の熱電特性)

MOHD NATASHAH BIN NORIZAN

January 2019

Graduate School of Engineering

Osaka University

Abstract

Thermoelectric is a technology dealing with direct conversion of thermal waste energy into electrical power. The efficiency of thermoelectric energy generator is restricted by dimensionless figure of merit (*ZT*). Thermal conductivity reduction is needed to achieve high *ZT* while maintaining or increasing the electrical properties. The purpose of this study is to propose a new material fabrication method to reduce thermal conductivity without degradation of electrical properties, using both melt-spinning (MS) rapid solidification technique and eutectic phase separation.

In the first chapter, thermoelectric conversion, theoretical background of thermoelectric properties, solidification techniques and eutectic phase separation were described and the literature data were reviewed. Based on the above, a newly propose fabrication method and the purpose of this study are introduce.

The second chapter explained the methodology to synthesize and characterize the material used in the research. The first section described the preparation methods of arc-melting (AM) and quench-melting (QM) technique for ingot, MS for rapidly cooled thin ribbon/flake, and spark plasma sintering (SPS) for the densification. The second section described the measurement technique of thermoelectric and physical properties.

The third chapter demonstrated the fabrication method for *p*-type Si/$CrSi_2$ eutectic alloy by using MS technique. The eutectic lamellar microstructure size is downsize to the nanometer range. Decreasing the rotation speed increase the average eutectic spacing, which confirm that this fabrication technique can control the size and produce nanostructure composite thermoelectric materials. It is confirm that the thermal conductivity can be reduce to its one-third, which result in the enhancement of *ZT* value.

The fourth chapter investigated the fabrication of *n*-type Si/$CrMnSi_2$ eutectic alloy by adopting MS technique and SPS process. High density bulk samples have been produce from ribbons or flakes. The MS-SPS sample microstructure was effectively refine by nearly one-tenth than AM-SPS sample even though grain growth occur through the sintering process. Through the microstructure refinement, thermal conductivity is decrease but the power factor is not deteriorate in spite of the high density of interface between Si and silicide phases. The

results confirm that the MS-SPS can produce clean interfaces, which is preferable as thermoelectric materials.

The fifth chapter investigated Bi-Sb alloy and InSb eutectic composite fabricated by MS-SPS. The submicrometer-sized composites are successfully obtain. The structure can reduce the thermal conductivity by 35 % and slightly increase *ZT* value. This confirm that the new fabrication technique can be apply to various thermoelectric material systems.

The sixth chapter summarized the overall development on the self-assembly fabrication processes using eutectic phase separation, rapid solidification and SPS. It is conclude that the new fabrication technique can provide fine nanostructure composites and is promising method to improve the thermoelectric performance.

TABLE OF CONTENTS

CHAPTER **Page**

CHAPTER I

Introduction

1.1 Background

In modern times, energy demand and population growth have increased with progress in science and technology [1]. As a result, the problem of exhaustion of energy resources and global warming caused by greenhouse gases generated by combustion of fossil fuels has become serious [2–4]. Therefore, expectations are growing for technologies related to energy saving and effective utilization of new energy, aiming at reducing fossil fuel consumption [5]. While attention is focused on technology related to the effective use of renewable energy including sunlight and wind power, about 66% of primary energy is currently waste heat, its unused heat (waste heat) efficient utilization has attracted attention from the viewpoint of high energy efficiency [6]. Therefore, this research focused on thermoelectric (TE) power generation that can convert energy directly from heat to electricity.

TE power generation is a technology to produce electric power by adopting a TE conversion material utilizing the Seebeck effect of generating a thermoelectromotive force when a temperature difference is provided between a metal or a semiconductor material [7]. Schematic diagram of TE conversion module is showed in Fig. 1. TE power generation system has excellent points such as maintenance free, low running cost, no vibration or no noise, no scale effect [8]. Under other conditions, problems include cost, toxicity, and scarcity of constituent elements in addition to low conversion efficiency, which is a big problem for large-scale practical application [9]. Hence, considerable incentive for researcher to develop new material composed of eco-friendly, low-cost and more earth-abundant element. The author attempted in this thesis to investigate the TE properties of TE materials based on silicone (Si) and bismuth (Bi). This type of material are expected to be most promising novel TE materials. Furthermore, enhancement of TE performance by the fabrication of nanoscale eutectic alloy that are self-assembled using rapid solidification technique is further explored.

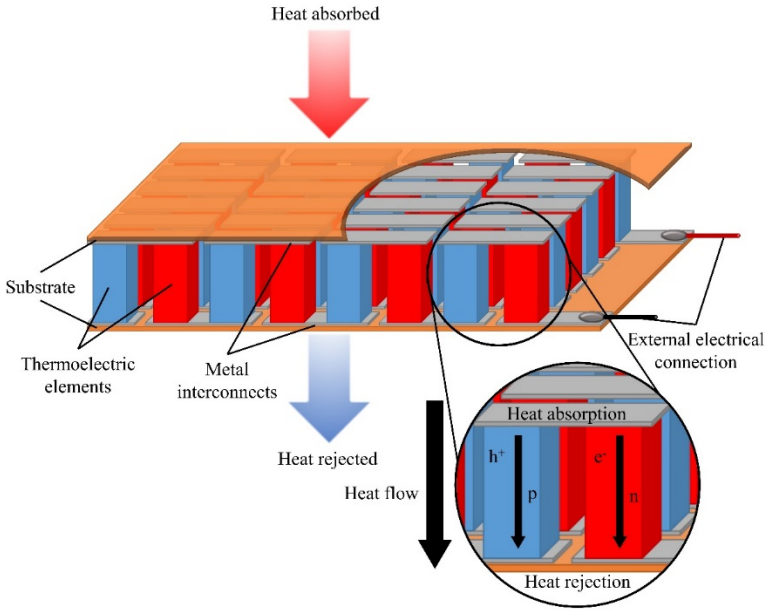

Figure 1.1 Schematic diagram of a thermoelectric conversion module [7].

1.2 Thermoelectric Phenomena

The thermoelectric conversion material is based on three thermodynamic interactions of Seebeck, Peltier, and Thomson effect. Thermoelectric power generation and cooling were performed using these effects. These phenomena will be described as below.

1.2.1 Seebeck Effect

When two different conductors, 1 and 2 are connected to form a closed circuit loop as shown in Fig. 1.2 and the junction temperatures of these two loops are different as T and $T + dT$, the current I flows through this closed circuit. When an arbitrary position a – a' cross section of this circuit is cut off, an electromotive force dV_{12} is generated between both ends of the cut. This incident is called Seebeck effect and S_{12} is called the Seebeck coefficient (thermoelectric power).

$$dV_{12} = S_{12}dT \tag{1.1}$$

The thermoelectric power per 1 K of temperature difference is called relative thermoelectric power, and generally S_{12} shows temperature dependence, so the electromotive force V_{12} of the closed circuit at the high temperature side of the T_H and the low temperature side of the T_C is expressed by the following equation.

$$V_{12} = \int_{T_C}^{T_H} S_{12}(T)dT \tag{1.2}$$

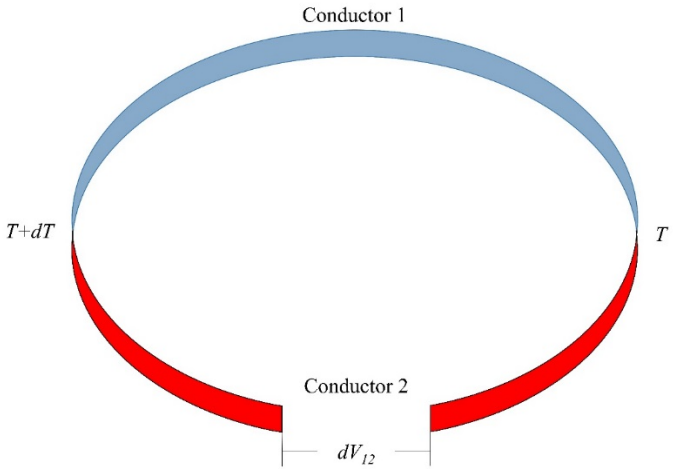

Figure 1.2 Thermoelectric closed circuit joining two dissimilar conductors

1.2.2 Peltier Effect

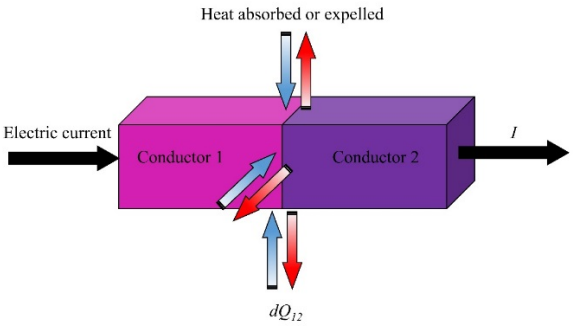

Figure 1.3 Thermoelectric closed circuit joining two dissimilar conductors

When the current, I passes through a connection between two different types of conductors, the release or absorption of heat depends on the direction of the current at this boundary. The amount of heat and the sign of it depends on the nature of the bonding material

and the amount of heat depends on the time and the I. As shown in Fig. 1.3, the amount of heat Q_{12} generated when the I flows through the intersection of the two kinds of conductors is expressed by the following equation.

$$dQ_{12} = \pi_{12} I dT \tag{1.3}$$

π_{12} is called the Peltier coefficient, and heat absorption and heat generation are switched when the current flows in the reverse direction.

1.2.3 Thompson Effect

In the same conductor in which the temperature distribution is present, the carrier diffuses from high temperature part to low temperature part and heat carriers are transported against the internal electric field commensurate with the diffusion of this carrier, so that heat is released from the conductor. If an external electric field causes a current to flow in the same direction as the internal electric field, the internal electric field carries out transportation that increases the current to absorb heat. As shown in Fig. 1.4, the heat quantity dq released by the current I in the region of the length dx in the temperature gradient in the conductor is expressed by the following equation.

$$dq = \tau_1 I \frac{\partial T}{\partial x} dx dT \tag{1.4}$$

τ_1 is the Thomson coefficient.

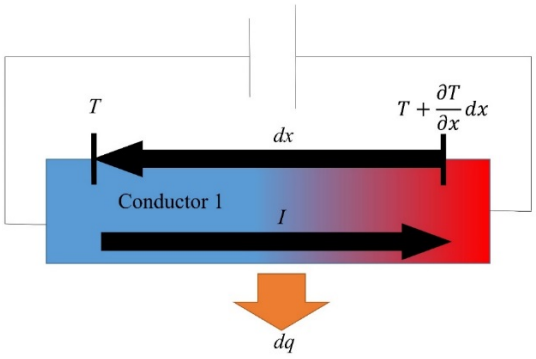

Figure 1.4 Thomson absorption heat generated by current when a temperature gradient exists on the same conductor

1.2.4 The Kelvin Relationships

Seebeck effect, Peltier effect, Thomson effect is related with thermodynamic law. As shown in Fig. 1.5, consider a closed circuit where there is a temperature difference at the joint. The Peltier heat absorption $\pi_{12}dI$ and the heat radiation $\pi_{21}dI$ generated at the joint are connected by the following relational expression.

$$\pi_{21} = \pi_{12} + \frac{\partial \pi_{12}}{\partial T} dT \tag{1.5}$$

Also, since there is a temperature difference in the same conductor, heat absorption $\tau_1 dIdT$ and heat radiation $\tau_2 dIdT$ due to Thomson effect occur. Since the power consumption of this closed circuit is $S_{12}dIdT$, the first thermodynamic law of this circuit can be expressed as follows.

$$-\pi_{12}dI + \pi_{21}dI - \tau_1 dIdT + \tau_2 dIdT = S_{12}dIdT \tag{1.6}$$

From Eq. 1.6, the following expression is obtained.

$$\frac{\partial \pi_{12}}{\partial T} - (\tau_1 - \tau_2) = S_{12} \tag{1.7}$$

Next, we derive the relational expression when we consider the reversible process of Seebeck coefficient, Peltier effect, Thomson effect separately from non-reversible process of heat conduction and Joule's heat. When heat is absorbed and absorbed in the Fig circuit. 1.6 As these are reversible processes, the following equation may express the condition that the entropy as a whole changes to zero.

$$\frac{\pi_{21}}{T + dT} dI - \frac{\pi_{12}}{T} dI + \frac{\tau_2 - \tau_1}{T} dIdT = 0 \tag{1.8}$$

Using the relational expression between the Peltier coefficients, it can be rearranged as follows.

$$\frac{d\pi_{12}}{dT}\frac{dT}{T+dT}-\frac{\pi_{12}}{T}\frac{dT}{T+dT}=(\tau_1-\tau_2)\frac{dT}{T} \tag{1.9}$$

Here dT is less than T, assuming that dT is large enough to be ignored for T, the following is obtained.

$$\frac{d\pi_{12}}{dT}-\frac{\pi_{12}}{T}=\tau_1-\tau_2 \tag{1.10}$$

Using the relation derived from the first law of thermodynamics, the following relational expression is obtained.

$$S_{12}=\frac{\pi_{12}}{T} \tag{1.11}$$

The above relational expression is called Kelvin's relational expression.

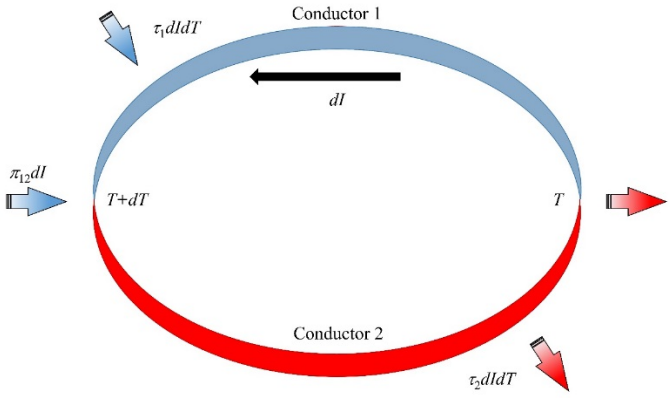

Figure 1.5 Heat absorption/heat dissipation in thermoelectric conversion

1.3 Thermoelectric Figure of Merit

When conductor is applied with temperature gradient, charge carriers at hot side acquire extra kinetic energy than those at cold side until the potential gradient prevent more diffusion. A dynamic equilibrium ensure that no net transfer of charge while only a transfer of kinetic (heat) energy. Hence, conductor hot side will change to positively charged because electrons transported away otherwise negatively charged assuming that whole transport is predominant.

As shown in the Fig. 1.6, when the electrode is coupled with *p*-type and *n*-type TE materials and there is a difference in temperature, $T_H - T_C$, electric current (I) occurs at the junctions. Absorbed heat at hot junction Q_{np} and released heat at cold junction Q_{pn} are expressed as

$$Q_{np} = S_{pn} I T_H \text{ and } Q_{pn} = S_{pn} I T_C . \tag{1.12}$$

Transported heat from hot junction to cold junction, Q_m, can be written:

$$Q_m = K(T_H - T_C) \tag{1.13}$$

where K is a specific coefficient for materials. The electrical current is shown as

$$I = \frac{S_{pn}(T_H - T_C)}{R + r} \tag{1.14}$$

where r is the absolute internal resistance of TE device.

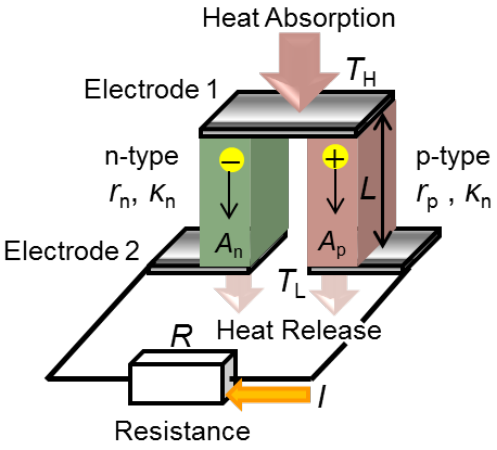

Figure 1.6 Schematic illustration of TE generator

The resistance r can be defined as following eq. 1.15 using the length of the materials, L, the internal resistance r_n and r_p, the electrical resistivity ρ_n and ρ_p, and the cross section area A_n and A_p for n- and p-type TE material, respectively.

$$r = r_{\mathrm{n}} + r_{\mathrm{p}} + = \left(\frac{\rho_{\mathrm{n}}}{A_{\mathrm{n}}} + \frac{\rho_{\mathrm{p}}}{A_{\mathrm{p}}} \right) L \tag{1.15}$$

Additionally, the thermal conductance K_{pn} can be defined as following equation:

$$K_{\mathrm{pn}} = K_{\mathrm{n}} + K_{\mathrm{p}} = \kappa_{\mathrm{n}} A_{\mathrm{n}} + \kappa_{\mathrm{p}} A_{\mathrm{p}} \tag{1.16}$$

where κ_{n} and κ_{p} are the *n*-type and *p*-type TE material thermal conductivity, respectively.

Then, applied heat Q_{total} can be expressed as

$$Q_{\mathrm{total}} = Q_{\mathrm{pn}} + Q_{\mathrm{m}} - \frac{1}{2} I^2 r = \alpha_{\mathrm{pn}} I T_{\mathrm{H}} + K\left(T_{\mathrm{H}} - T_{\mathrm{C}}\right) - \frac{1}{2} I^2 r \tag{1.17}$$

.

The energy efficiency η is obtained using Q_{total} and available energy $P = I^2 R$:

$$\eta = \frac{P}{Q_{\mathrm{total}}}$$

$$= \frac{S_{\mathrm{pn}}{}^2 \left(T_{\mathrm{H}} - T_{\mathrm{C}}\right) \dfrac{1}{r\left((R/r)+1\right)^2}}{S_{\mathrm{pn}}{}^2 T_{\mathrm{H}} \left(T_{\mathrm{H}} - T_{\mathrm{C}}\right) \dfrac{1}{r\left((R/r)+1\right)^2} + K\left(T_{\mathrm{H}} - T_{\mathrm{C}}\right) - \dfrac{1}{2} \dfrac{1}{r\left((R/r)+1\right)^2} S_{\mathrm{pn}}{}^2 \left(T_{\mathrm{H}} - T_{\mathrm{C}}\right)^2} \tag{1.18}$$

$$= \frac{T_{\mathrm{H}} - T_{\mathrm{C}}}{T_{\mathrm{H}}} \frac{\dfrac{R/r}{\left((R/r)+1\right)^2}}{1 + \dfrac{K\left((R/r)+1\right)}{S_{\mathrm{pn}}{}^2 T_{\mathrm{H}}} - \dfrac{1}{2} \dfrac{T_{\mathrm{H}} - T_{\mathrm{C}}}{T_{\mathrm{H}}} \dfrac{1}{(R/r)+1}} .$$

Thus, the TE efficiency is determined by following parameters: (i) temperatures of junctions, T_{H} and T_{C}, (ii) materials intrinsic parameters K, r, and S_{pn}, and (iii) the ratio of internal and external resistance R/r.

In the case that these parameters except for K are constant, K should be as small as possible to maximize the efficiency η.

$$K = \left(\kappa_n A_n + \kappa_p A_p\right)\left(\frac{\rho_n}{A_n} + \frac{\rho_p}{A_p}\right) = \kappa_n \rho_n + \kappa_p \rho_p + \kappa_n \rho_p \frac{A_n}{A_p} + \kappa_p \rho_n \frac{A_p}{A_n} \tag{1.19}$$

To minimize K, K was differentiated with respect to the ratio of area (A_p/ A_n), then the following equation is obtained.

$$\left(\frac{A_p}{A_n}\right)^2 = \frac{\kappa_n}{\rho_n}\frac{\rho_p}{\kappa_p} \tag{1.20}$$

The thermal conductance K can be determined by choosing (A_p/ A_n) fulfill the equation (1.21):

$$K = \left(\sqrt{\kappa_n \rho_n} + \sqrt{\kappa_p \rho_p}\right)^2 . \tag{1.21}$$

Using equation (1.22), TE figure of merit and efficiency, independent to sizes of materials, can be obtained as

$$Z_{pn} = \frac{{S_{pn}}^2}{K} = \frac{{S_{pn}}^2}{\left(\sqrt{\kappa_n \rho_n} + \sqrt{\kappa_p \rho_p}\right)^2} \tag{1.22}$$

$$\eta = \frac{T_H - T_C}{T_H} \frac{\dfrac{R/r}{\left((R/r)+1\right)^2}}{1 + \dfrac{(R/r)+1}{Z_{pn} T_H} - \dfrac{1}{2}\dfrac{T_H - T_C}{T_H}\dfrac{1}{(R/r)+1}} . \tag{1.23}$$

On the other hand, to maximize η, if η was differentiated with respect to the ratio of resistance (R/ r), following relationship is obtained.

$$\left(\frac{R}{r}\right)_{opt} = \sqrt{1 + Z_{pn}\frac{T_H + T_C}{2}} = \sqrt{1 + ZT_m} \tag{1.24}$$

Here, $T_m = (T_H + T_L)/2$ is mean value of absolute temperature in the device. Then the maximum efficiency η_{max} is expressed as below:

$$\eta_{max} = \frac{T_H - T_C}{T_H} \frac{\sqrt{1+ZT_m} - 1}{\sqrt{1+ZT_m} + T_C / T_H} . \quad (1.25)$$

The relation between η_{max} and ZT_m is outline in Fig. 1.7 for T_C = 300 K. In reaching higher TE efficiency, higher Z value and larger temperature difference is needed. Application with ZT_m > 1 ~ 1.5 will benefit in accomplish the efficiency of η > 0.1, from view of commercial use.

From the Eq. (1.22), the absolute ZT is determined by Eq. (1.26), using the material absolute Seebeck coefficient (S), electrical resistivity (ρ) or electrical conductivity (σ), and thermal conductivity (κ).

$$ZT = \frac{S^2}{\kappa\rho} T = \frac{S^2\sigma}{\kappa} T \quad (1.26)$$

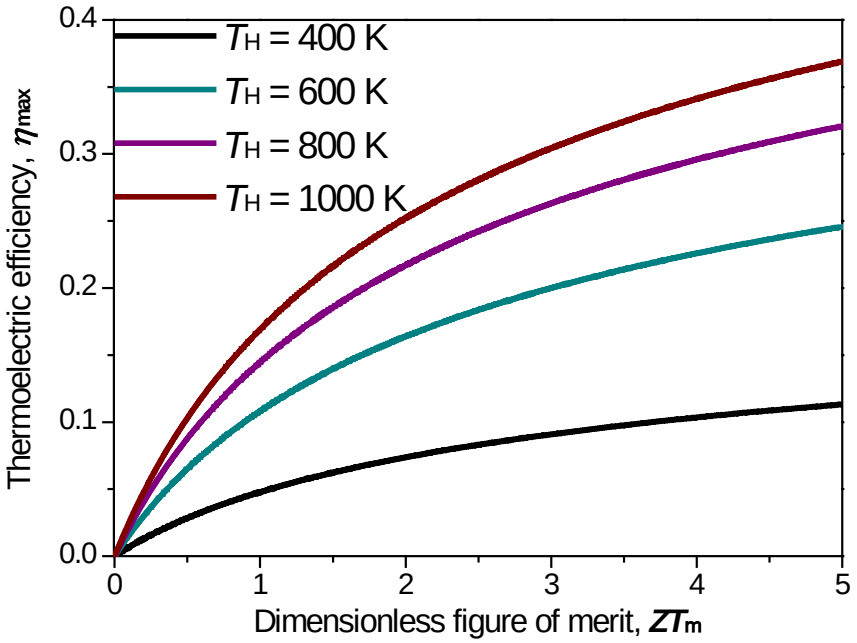

Figure 1.7 Dimensionless figure of merit, ZT_m, dependences of maximum efficiency, η_{max}, in the case of T_C = 300 K

1.4 Improvement of Thermoelectric Performance

To improve ZT, it is a needs to increase electrical properties (S, ρ) and subsequently, decreasing the κ. Doping manipulation for materials is a key practise to the considerable change

in the TE properties and crystallographic [10]. Shown in Fig. 1.8, S decreases and the concentration gain of the carrier increases in both κ and σ (= ρ-1). Therefore, high power factor ($S^2\,\sigma$) and ZT are achieved in correlate to the region of massively doped semiconductor [11].

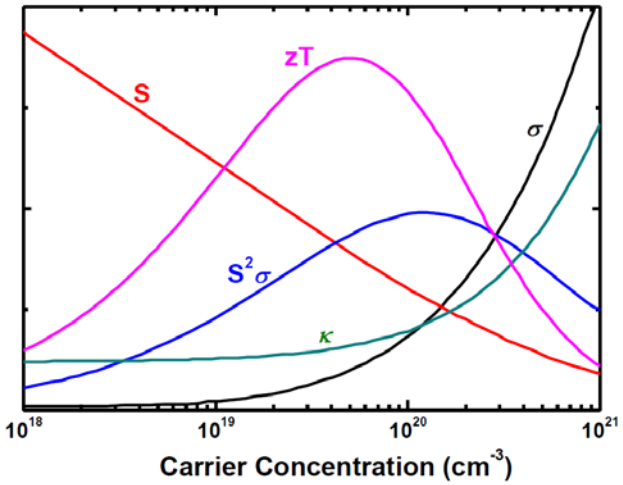

Figure 1.8 Carrier concentration dependences of S, σ, $S^2\sigma$, κ, and ZT by assuming acoustic phonon scattering and single parabolic band

1.4.1 Carrier Concentration

Only a single type of carrier is needed in order to make sure S is higher. Mixed p-type and n-type conduction force both charge carriers shifting to cold side, annihilate the Seebeck voltages. Correlation between S and carrier concentration conceivable seen by comparably simple models of electron transport. S for degenerate semiconductors or metals is specified by [12]:

$$S = \frac{8\pi^2 \kappa_B^2 T}{3eh^2} m^* \left(\frac{\pi}{3n}\right)^{\frac{2}{3}} \tag{1.27}$$

where m^* is effective mass and n is concentration of carrier. Eq. (1.27) indicates that low n semiconductors and even insulators have high S. Nevertheless, low n also effects in small σ; as seen in Eq. (1.28). The ρ and σ are correlated to n over carrier mobility μ:

$$\frac{1}{\rho} = \sigma = ne\mu \tag{1.28}$$

1.4.2 Thermal Conductivity

The thermal conductivity in TE originates from holes and electrons transporting heat (κ_e) and phonons transmitted through the lattice (κ_l). The Wiedemann-Franz law directly correlates κ_e [11]:

$$\kappa = \kappa_e + \kappa_l \tag{1.29}$$

$$\kappa_e = \frac{\pi^2 n \kappa_B^2 T \tau}{3m}, \sigma = \frac{ne^2\tau}{m} \tag{1.30}$$

$$L = \frac{\kappa_e}{\sigma T} = \frac{\kappa_e}{ne\mu T} = \left(\frac{\kappa_B}{e}\right)^2 \frac{\pi^2}{3} \approx 2.45\ x\ 10^{-8}[W\Omega K^2] \tag{1.31}$$

where L is the free electrons Lorenz factor.

The Lorenz factor can vary predominantly with n. Precise calculation of κ_e is essential, as κ_l is frequently calculated by subtracting κ and κ_e (Eq. 1.29) from the σ experimental results. Uncertainty in κ_e occurs in materials with low carrier concentration where the Lorenz factor can be reduced by about 20 percent from the free electron value. In κ_e, more uncertainly, mixed conduction leads to a bipolar term in κ [11,13–15]. Wiedemann-Franz law discloses an inherent materials conflict for achieving high TE efficiency as high ZT requires high σ but low κ. For materials with very high σ such as metals or very low κ_l, the S alone primarily determines ZT, as can be described using Eq. (1.32), where

$$\frac{\kappa_l}{\kappa_e} \ll 1 \tag{1.32}$$

$$ZT = \frac{\frac{S^2}{L}}{1 + \frac{\kappa_l}{\kappa_e}} \tag{1.33}$$

Efforts in reducing the lattice part of the κ essentially to its minimum value are being done in many areas of research related to new TE materials. Crystal bonding will pass the excitation to the neighboring atoms if an atom in the crystal lattice is thermally excited. Heat is transported through the bulk through this mechanism. Because of the periodic structure of

the crystal lattice, these vibration effects can be described by quasi-particles called phonons. Phonons move through the crystal, carrying a certain amount of energy in form of heat. Considering the phonons, the representation of the κ_l is able to be obtained by solving the Boltzmann equation for phonons with the same procedure as that of charged carriers, electrons. The κ_l is derivative from the transport properties of phonon. The transport of phonon also can be defined by the relaxation time approximation. Thus, the κ_l is expressed as [11,13,14]

$$\kappa_l = \int \tau \frac{E^2}{T} v_x^2 \left(-\frac{\partial f_B}{\partial E}\right) G(E) dE \tag{1.34}$$

where $G(E)$, E, v_x and τ are the phonon density of states, the energy, the group velocity, and the relaxation time of phonon scattering, respectively. The distribution of phonons in thermal equilibrium state is given by the Bose distribution as follow:

$$f_B(E) = \frac{1}{exp\left(\frac{E}{K_B T}\right) - 1} \tag{1.35}$$

The τ can be reveal for numerous scattering mechanisms by

$$\frac{1}{\tau} = \frac{1}{\tau_{PP}} + \frac{1}{\tau_{PC}} + \frac{1}{\tau_{PA}} + \frac{1}{\tau_{PG}} + \cdots \tag{1.36}$$

where τ_{PP}, τ_{PA}, τ_{PC}, and τ_{PG} are phonon to phonon scattering by Umklapp process, phonon to alloying scattering, phonon to carrier scattering, and phonon to grain boundary scattering, respectively. If M, ξ, δ, γ, θ_D, m^*, N, v_s, $y(1\text{-}y)$, ΔM, Δr, and L are average mass per atom, Fermi energy, cubic root of the average atomic volume, Gruneisen parameter, number of atom in a unit cell, Debye temperature, effective mass, sound velocity, product of alloy composition, difference atomic mass, difference atomic radius, and mean free path, then either relaxation time can be explained as

$$\frac{1}{\tau_{PP}} \frac{280\sqrt[3]{3}\pi^{\frac{5}{3}}}{27\sqrt[3]{2}} \frac{\bar{h}N\gamma}{M\delta^{\frac{2}{3}}} \left(\frac{T}{\theta_D}\right)^{\frac{1}{3}} \xi \tag{1.37}$$

$$\frac{1}{\tau_{PC}} = \frac{E^2 m^* v_S}{4\pi \bar{h}^4 \rho \phi} \langle \xi - ln \frac{1 + exp\left[\phi - \frac{\xi F}{16\phi^2} + \xi/2\right]}{1 + exp\left[\phi - \frac{\xi F}{16\phi^2} - \xi/2\right]} \rangle \tag{1.38}$$

$$\phi = \frac{m^* v_s^2}{2\kappa_B T} \tag{1.39}$$

$$\tau_{PA} = \frac{1}{4\pi} \frac{\delta^3}{v_S^3} \left(\frac{\kappa_B T}{\bar{h}}\right)^4 y(1-y) \langle \left(\frac{\Delta M}{M}\right)^2 + \varepsilon_S \left(\frac{\Delta r}{r}\right)^2 \rangle \xi^4 \tag{1.40}$$

$$\tau_{PG} = \frac{v_S}{L} \tag{1.41}$$

On the other hand, according to a model reported [16], low κ_l can be estimated in the materials which please the conditions as a large average mass of its constituent atoms, a low melting point, and a large unit cell. Further, the minimization of the κ_l is very useful in improving the *ZT* value. Analytically, the κ_l is proportional to T^{-1} at high temperature and proportional to T^3 at low temperature, has maximum at around 0.05 θ_D.

1.4.3 Grain-Size Effects

Average size of grains contributes significantly to the κ of a material. Its effect can be consequent from the concept that the grain boundaries are thermal resistors in series with the grains. This shown in the following Eq. 142:

$$\kappa = \frac{\kappa_i}{1 + \frac{R_\kappa \kappa_i}{d}} \tag{1.42}$$

Where *d* is average grain size, κ_i is intrinsic conductivity or the κ of a single crystal, and R_κ is the thermal boundary resistance. Another term that is useful when investigating the effect of grain size on κ of polycrystalline materials is the Kapitza length l_κ. It is defined as material thickness of κ that provides the same change in temperature as a given boundary. It is given in the following form:

$$l_\kappa = \frac{\kappa}{G_\kappa} \tag{1.43}$$

Where $G\kappa$ is the Kapitza conductance. Grain size effect on the κ should be minor if the grain size is considerably higher than the Kapitza length, $d > l_\kappa$. Phonon scattering at the interface becomes significant as the size of the grains match the Kapitza length and will reduce the κ compared to the same material with bigger grains.

For certain materials the effect of the grain size on κ decreases with increasing temperature. At maximum temperatures, the grain size has little or no effect on the κ. Smaller grains do not result in lower values of total κ at very high temperatures when compared to the same material with bigger grains [17].

1.5 Thermoelectric Materials

Over the past 30 years, alloys based on Bi_2Te_3, PbTe, SiGe, and BiSb which is traditional small ban gap materials systems have been widely studied. Here, the TE properties of those compounds are introduced simply.

Bi_2Te_3 is a narrow-gap semiconductor with an indirect gap of around 0.15 eV. It crystallizes in the rhombohedral space group *R*-3*m*. The structure made up of five atomic layers (Te1-Bi-Te2-Bi-Te1), comprises plates, stacked by van der Waals interactions along the c-axis in the unit cell. The state-of-the-art Bi_2Te_3 materials with the TE figure of merit $ZT \approx 1$ are synthesized by alloying with Sb for *p*-type and Se for *n*-type materials [18].

In contrast to Bi_2Te_3, PbTe crystallizes in the NaCl crystal structure. That premiere TE material for mid-range temperature around 600 to 800 K applications. A band gap of 0.32 eV allows it to be optimized for power-generation applications and can be doped either *n*- or *p*-type with appropriate dopants. The maximum *ZT* value for PbTe has been reported to be 0.8–1.0 at approximately 650 K. The κ_l of PbTe is approximately 2.2 $Wm^{-1}K^{-1}$ at room temperature and falls at higher temperature with a T^{-1} dependence. Significant recent work has focused on improving the thermoelectric properties of PbTe by nanostructuring [19].

Neither Si nor Ge is a good thermoelectric material, as the κ_l is very large (150 $Wm^{-1}K^{-1}$ for Si and 63 $Wm^{-1}K^{-1}$ for Ge). The κ_l can be substantially reduced by alloy formation between

the two elements. The best alloy composition is $Si_{0.7}Ge_{0.3}$; κ about 10 $Wm^{-1}K^{-1}$. The reduction of κ_l ctivity manly came from phonon to phonon and phonon toelectron scattering. Since the 1960s, efforts have been made to improve the *ZT* of SiGe alloys, with the peak *ZT* of *n*-type SiGe reaching 1 at 900-950 °C [20].

For cooling below room temperature, BiSb alloys have been used in the *n-type* legs, couple with *p-type* legs of $(Bi,Sb)_2(Te,Se)_3$. These alloys have been extensively studied and optimized for their uses as thermoelectric materials to perform a variety of thermoelectric refrigeration and power-generation applications. In order to improve the performance of these materials, the attempts have been done to increase *ZT* values by controlling the carrier concentration and reducing the lattice thermal conductivity [21].

Despite the advantageous TE properties of the above-mentioned materials, however, most of these heavy element contain high-toxicity and/or expensive elements that limit their application on a large scale. Therefore, researchers have a considerable incentive to develop alternative materials consisting of environmentally friendly, low-cost and abundant elements.

1.6 Current Research

Si has attracted attention as a promising candidate sustainable thermoelectric material. In addition to its advantages of low-cost and environmental friendly, Si the second-most abundant element in the earth's crust. Bulk Si possess outstanding electrical properties including charge carrier transport which are deniable for high-efficiency thermoelectric material. Unfortunately, bulk Si also exhibits a relatively high κ_l (> 140 $Wm^{-1}K^{-1}$ at room temperature) leading to limited *ZT* of ~0.02 at room temperature [22].

For many years, the main approach for developing high-efficiency Si based thermoelectric material was focused on the suppression phonon transport which acts as a main contributor to the lattice thermal conductivity. Initially, the phonon transport properties of a Si bulk material can be rectified and suppressed by controlling the type and amount of doping impurities and to forming solid solutions, such as various PbTe based composites and Si-Ge system. Lattice thermal conductivity of these solid solutions decreased thanks to a mechanism of point defect phonon scattering. However, the introduction of point defects does not only suppress a material's phonon transport, but also led to severe degradation in carrier transport

of carrier concentration. Thus, the overall enhancement of *ZT* has been limited by trade-off between the phonon and carrier transports [23].

Nanostructuring approach has been introduced for developing advanced Si based thermoelectric materials. Nanostructures offer a material with complex crystal structures including high density of grain boundaries (nanostructured structure), small point defects (nanoparticles) embedded in a majority phase (matrix) and nanostructured composites (nanocomposites). Such complex structures have experimentally been proven that they introduced scattering mechanisms that scattered phonon very effectively, leading to a drastic reduction of lattice thermal conductivity. Several low dimensional Si structures such Si nanowires [24–26] and Si thin films [27,28] showed significant increase in *ZT* which exhibited not only large reduction in lattice thermal conductivity but also enhancements in electrical properties. However, such low dimensional structures are not suited to the requirement of high temperature application due to unfavorable mechanical and long-term thermal stability [29]. Furthermore, this methods are not suitable for mass production and fabrication of bulk TE materials

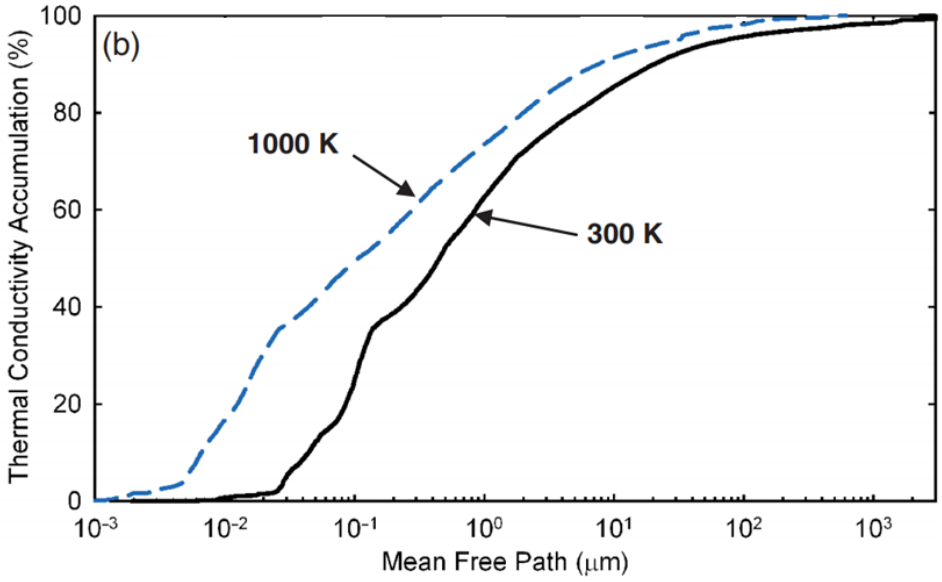

Figure 1.9 Percentage of thermal conductivity accumulation of Si at 300 K and 1000 K [30]

For example, Fig. 1.9 show the theoretical modeling on the contribution of phonon scattering to the lattice thermal conductivity was carried out as a function of the mean-free path for Si. The calculations showed that 90 percent of thermal conductivity in Si is due to phonons with a mean free path greater than 20 nm. [30] Consequently, if the grain size was reduced to

20 nm, the thermal conductivity of the lattice could be reduced by 90 percent. The carrier mobility should not be affected as the electron mean free path of the in Si was calculated to be only a few nanometers [31]. The guidelines for the dimensions of nanoparticles vary for different material systems, but the critical feature sizes of nanoscale (5 to 50 nm) are necessarily left. Composite structures with controlled distribution of nano-scale particles are expected to be discreet in size and possibly in composition in order to fully optimize the thermoelectric properties of a material [32].

In bulk materials, Si nanocrystals formed by metallurgical powder methods have a thermal conductivity of about 10 $Wm^{-1}K^{-1}$ at room temperature and a relatively high ZT of about 0.7 at temperatures of almost 1200 K. However, this type of processing of Si nanoparticles leads to the formation of oxides, the segregation of impurities and amorphous areas on the grain boundaries. These factors tend to reduce the carrier mobility with a decrease in grain size, leading to a poor thermoelectric power factor. Additionally, these sample fabrications require complex procedures and much labor such as long ball-milling time. It is hypothesized that self-assembled nanostructures prevent these problems because the interface that is naturally formed tends to be relatively clean and smooth.

1.7 Eutectic Phenomena

A eutectic system is a homogeneous combination of substances that melts or solidifies at a single temperature below the melting point of either component. For each alloy, there is a certain composition in which only one solidification temperature exists, not a range as shown in Fig. 1.10. The temperature of this alloy is the minimum temperature of melting. In a non-eutectic alloy, the formation of the two phases takes place over a certain period of time during the temperature range of solidification. The composition and percentage of the two phases can be expected with the phase diagram during this time. With eutectic material, this is not possible. In an (ideal) infinitesimal time the melt becomes solid from the liquid. Then the two (or more) phases of eutectic material growth simultaneously. Due to their excellent casting behavior, often similar to that of a pure metal, and the advantageous composite properties demonstrated when solid, casting alloys are often almost eutectic.

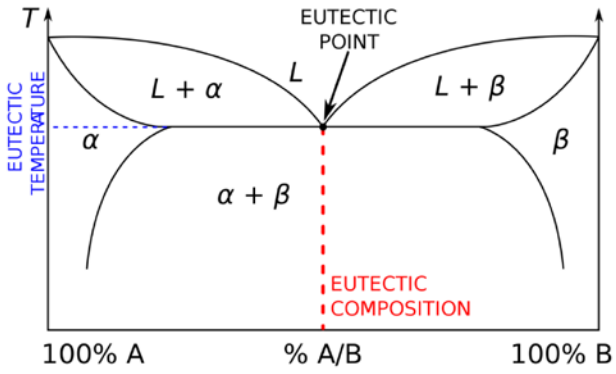

Figure 1.10 Eutectic composition in phase diagram

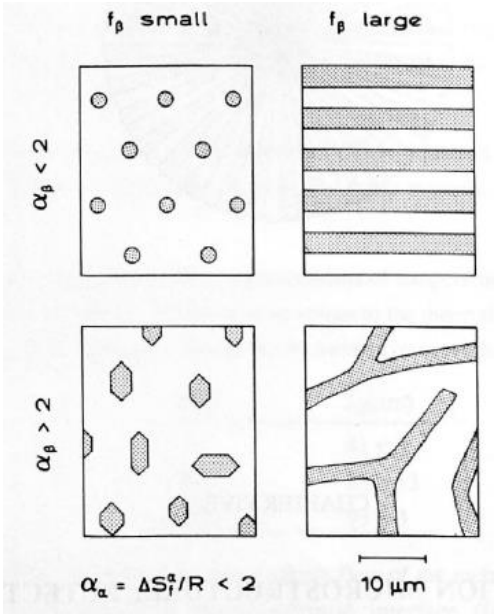

Figure 1.11 Types of binary eutectic morphology, the transversal image on the left and the longitudinal crossings of the discretionally solidified microstructure on the right [33]

Since they comprise more than one phase, eutectics can show a wide variety of geometric arrangements. These geometric shapes can be regular, irregular or fibrous. These eutectic morphologies are shown in Fig. 1.11. The eutectic structure is regular in the upper part of the figure. This occurs when both phases have low fusion entropy. When the low - volume fraction phase has a high fusion entropy, the structure is irregular, which is shown in the lower parts. Two pictures left in Fig. 1.11 have a structure of fibrous. This happens when there is a small fraction of a single phase in volume. In contrast, the lamellae are the preferred growth with a higher volume fraction. We can assume that the eutectic will probably be fibrous if the

volume fraction of one phase is between zero and 0.28. If it is between 0.28 and 0.50, the eutectic will tend to be lamellar.

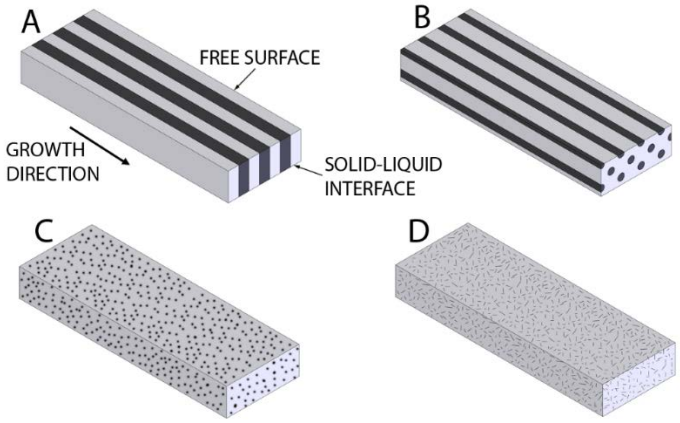

Figure 1.12 Four eutectic structures: A) lamellar B) rod-like C) globular D) acicular.

The simplest morphology for the solid / liquid interface is assumed to determine the growth behavior of the two eutectic phases during the growth of a regular lamellar eutectic as shown in Fig. 1.12. In this case, the problem can be treated in two dimensions. In Fig. 1.13, the alloy is imagined to grow in a crystal that at rate V' is moved vertically downwards.

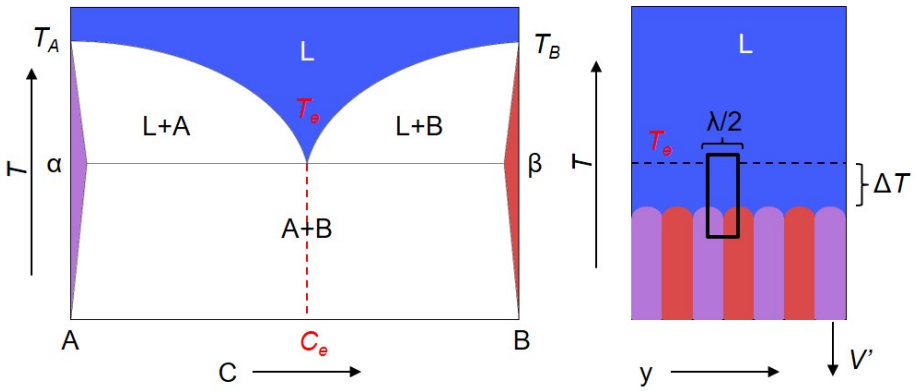

Figure 1.13 Eutectic phase diagram and regular growth of lamellae

This amounts to moving the solid / liquid interface in a stable thermal environment at a rate $V=V'$. The eutectic compositional alloy grows below the eutectic temperature with an essentially isothermal interface at temperature $T^*=T_e-\Delta T$. From the phase diagram, it can be seen that the two solid phases have a very different composition, while C_e is an intermediate composition. The mean composition of the solid must obviously be the same as the melt

composition in a stable condition. This demonstrates that eutectic growth is largely a question of mass transportation.

During growth, the solid phases reject the solvent into the liquid. Therefore, the α phase rejects B atoms in the melt and the β phase rejects A atoms. The rejected solvent in one stage is necessary for the growth of the other. Consequently, lateral diffusion at the right angle of the lamellae along the solid / liquid interface becomes dominant and leads to a decrease in the buildup of the solute before both stages. A periodic dissemination field shall be established. Since the maximum concentration differences at the interface (compared to the eutectic composition) are much smaller than in the case of single-phase growth, the increasing temperature of the interface is close to the eutectic equilibrium. The eutectic theory [34] gives the following relationship between the undercooling (ΔT), the growth rate (V) and the lamellar spacing (λ) for an isothermal solidification front as,

$$\Delta T = K_1 V\lambda + K_2 V\lambda \tag{1.46}$$

where K_1 and K_2 can be calculated from phase diagram and thermodynamic data. The relationship between the lamellar spacing (λ), growth rate (V) and constant related to material properties (K) is,

$$\lambda = \frac{K}{\sqrt{V}} \tag{1.46}$$

The diffusion field minimizes the structure's λ-value, which results in a faster growth shown in Fig 1.14.

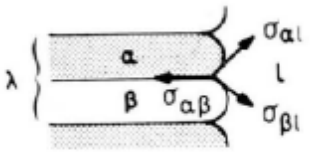

Figure 1.14 Diffusion effect at the solid / liquid interface [33]

The paths of the rejected B component from the A component were shown in the Fig. 1.15 (a) during the solidification. Therefore, the concentration in the liquid is not constant, but depends on the Fig. 1.15 (b). This variation in concentration can only be found in the liquid at

the solid / liquid interface but decreases in the direction of growth over an interphase. The eutectic spacing is determined by the balance between an attractive force resulting from the diffusion field and a repulsive force between the three - phase connections resulting from small λ capillarity effects.

The growing interface can be considered to be in a thermodynamic balance at the local level. This means that the measurable interface temperature, T_q*, which is constant along the solid / liquid interface (over λ /2), matches the balance at all interface points. Fig. 1.15 (c) is the function of local concentration and curvature. The amount of the solute (ΔT_c) and the undercooling curvature (ΔT_r) must be the same as the ΔT undercooling interface. A negative curvature is required, as shown in the center of the β lamella, when the undercooling of the solute, ΔT_c, is higher than ΔT. The discontinuity of the undercooling solvent is only a discontinuity of the temperature of the equilibrium and not a true temperature discontinuity.

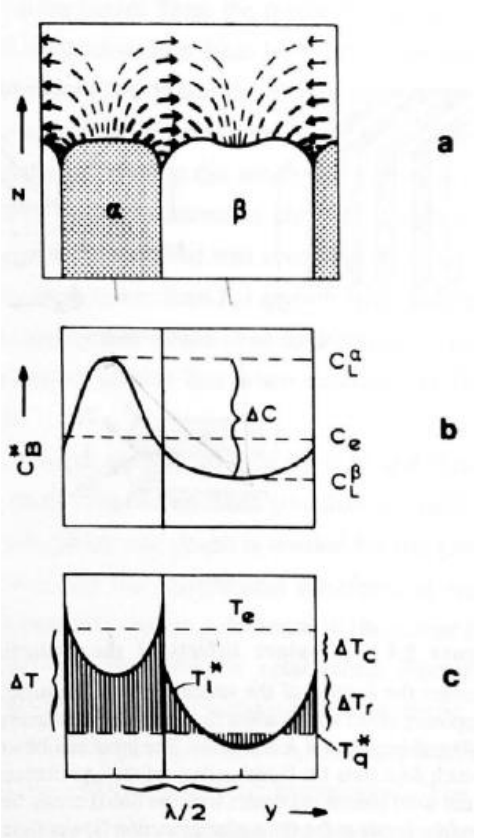

Figure 1.15 Eutectic interface concentration and temperature [33]

The corresponding liquid temperature for certain regions of the α-phase varies from values greater than T_e to values below the actual interface temperature, T_q* for the central

region of the β-phase. The difference must be compensated for by the local curvature to keep the local balance at the interface. As T_q* is constant due to the high thermal conductivity and small phase dimensions, a negative curvature(depression) can appear in the center of a lamella to compensate for a high local solute-controlled undercooling interface that is often associated with a large distance, λ. The curvature of the α/l (or β/l) interface, which is necessary to match the angles at the three phase interface, changes the temperature of the equilibrium by a quantity, ΔT_r, which is a function of y.

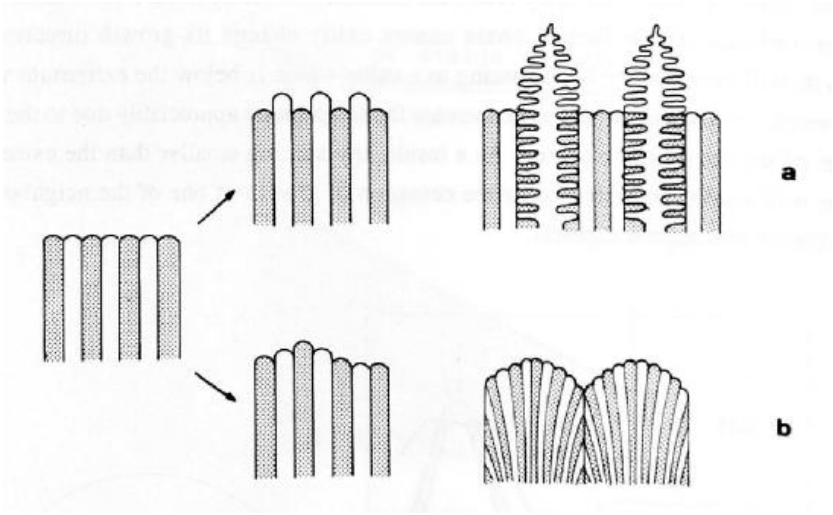

Figure 1.16 Type of eutectic interface instability [33]

Two types of morphological instability can be found in binary eutectics: single phase or two phase, as shown in Fig. 1.16. The usually flat solid / liquid interface can become unstable and lose its planar form. In Fig. 1.16, there are two types of instability, one phase (a) instability or two phase (b) instability. The instability of one phase occurs when one phase advances the other phase. This can happen if the alloy's chemical composition is off-eutectic. In this case, there is a small temperature interval for solidification that allows this stage to solidify earlier than the others. Since this stage is growing earlier, the structure may be dendritic. The reason for the latter effect is that in this case, due to the long-range boundary layer built up in front of the solid/liquid interface, one phase is heavily undercooled constitutionally. This can be explained by the fact that the liquid alloy is always higher than the eutectic temperature in an off-eutectic composition: the corresponding primary phase is more undercooled and tends to grow faster than the eutectic, as shown in Fig. 1.17. In the case of instability of both phases, a third element (impurity) may destabilize the morphology of the solid/liquid interface that can lead to an appearance of two phase eutectic cells, or even eutectic dendrite.

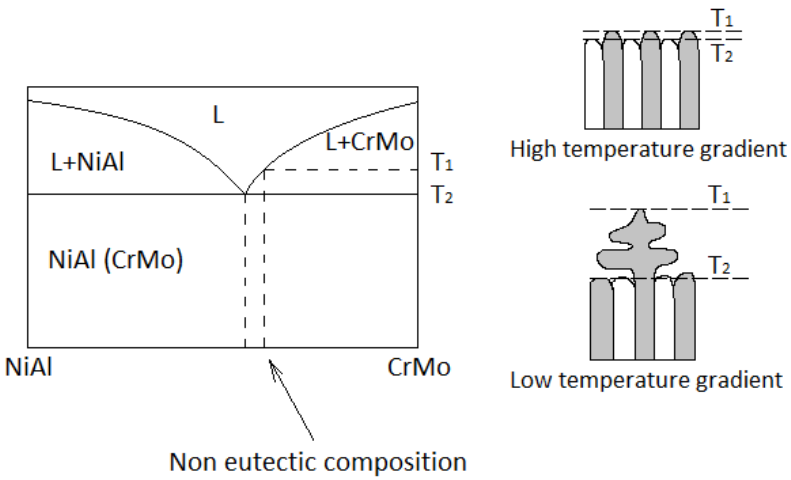

Figure 1.17 Effect of non-eutectic composition and gradient of temperature [33]

Eutectic alloys are generally fine microstructured composites that are self-assembled with some structural regularity directly from a melt. Its size decreases with an increase in the growth rate in cooling conditions at a minimum [35].

1.8 Rapid Solidification Technique

The normal cooling rates are produced by casting with a cooling rate of 10 K/s to 10^2 K/s [36]. Rapid solidification technology has been developed to produce uniform films of metastable phases with a cooling rate of 10^5 K/s. Semiconducting and metal alloys were amorphously molded [37].

This technique comprises of melting and injecting the sample on rapidly rotating rollers under certain pressure. The drop solidifies and thin uniform films of amorphous phases can be acquired while passing through the roller. Increasing the speed of the rotation and the injection pressure will reduce the film thickness. If the melt has solidified from the rollers during the time of exit, the quenching rate T can be estimated [38],

$$T = \Delta T/\Delta t \approx (T_t - T_g)v/d \qquad (1.49)$$

where T_g and T_t, respectively, glass and initial melt temperature, $\Delta t(\approx d/v)$ is the contact time between roller and melt, v is the linear velocity of the roller and d is the melt distance during solidification.

The advantages of this solidification method are: (a) the thickness of the quenched films is uniform. (b) Production of an endless strip of quenched material. (c) Applicable to ductile materials as well as to brittle semiconductors. (d) There is little internal stress because the shaping of the film occurs when it is still fluid.

1.9 Purpose of Study

The *ZT* development of bulk Si and Bi remains challenging recently. Although thermal conductivity can be greatly reduced through nanostructure, the effects of high density grain boundaries such as oxide formation, impurity segregation and amorphous areas simultaneously degrade the electrical properties of the nanostructured material. As was mentioned previously, for a large *ZT* enhancement, it is crucial to minimize or eliminate the phonon and carrier transport's trade-off. For this, it is a need for thermal conductivity to reduce while maintaining or increasing the electrical properties at the same time, meaning that high *ZT* is achievable. For further *ZT* enhancement of Si and Bi based composite thermoelectric materials, the goal of decreasing thermal conductivity through nanostructured structure may not be sufficient.

The purpose of this study is to investigate the behavior of the eutectic compound, which has a very fine structure using phenomena of natural phase separation. Furthermore, by using melt-spinning technique for the eutectic system, samples with nano-sized structure without contamination can be developed. Although there are many reports about eutectic structure and fabrication using the melt spinning method but there is no report which use both. In the present dissertation, Si and Bi based material eutectic system are investigate due to low toxicity, low cost and earth abundance.

First, the study focus on improving the thermoelectric performance of Si-based materials. It is known that nanostructuring has achieved a dramatic reduction in thermal conductivity along with high *ZT*. Due to the strong phonon dispersion at the grain border and other effects, nanostructure was considered to improve the *ZT* value. However, downstream methods like ball milling have problems such as contamination and mass production difficulties. Thus, we demonstrate the fabrication method for *p*-type Si/$CrSi_2$ eutectic alloys by MS. This technique can control the size by changing the rotation speed to increase or decrease the average eutectic spacing in order to produce nanostructure size.

Secondly, methods for densifying the ribbon sample without changing the microstructure are investigate. For good TE energy conversion applications, it is necessary to produce high density bulk sample together with combining *p*-type and *n*-type with similar material systems. Both the *p*-type and the *n*-type in the operating temperature range should be similar. Therefore, we studied conversion of *n*-type Si/$Cr_{0.8}Mn_{0.2}Si_2$ eutectic alloy by MS and therefore sintering by SPS.

Finally, the study investigate the fabrication method on other thermoelectric material eutectic system. It is known that a bismuth antimonide (BiSb) alloy is a semimetal compared to previous study of Si which is semiconductor. We therefore investigate the thermoelectric properties of *n*-type $Bi_{0.88}Sb_{0.12}$/InSb by MS and consequently sintering by SPS to study some information on the relationship between thermoelectric transport and microstructure properties with system other than Si and silicide.

1.10 Reference

[1] Gruda N and Tanny J 2015 Protected crops – recent advances, innovative technologies and future challenges *Acta Hortic.* **1107** 271–8

[2] Tollefson J and Weiss K R 2015 Nations approve historic global climate accord *Nature* **528** 315–6

[3] Ali R, Mansur T M N T, Baharudin N H and Hassan S I S 2016 Environmental impacts of renewable energy *Electric Renewable Energy Systems* (Elsevier) pp 519–46

[4] Branchini L, Cagnoli P, De Pascale A, Lussu F, Orlandini V and Valentini E 2015 Environmental Assessment of Renewable Fuel Energy Systems with Cross-Media Effects Approach *Energy Procedia* **81** 655–64

[5] Van de Graaf T and Verbruggen A 2015 The oil endgame: Strategies of oil exporters in a carbon-constrained world *Environ. Sci. Policy* **54** 456–62

[6] Tritt T M, Böttner H and Chen L 2008 Thermoelectrics: Direct Solar Thermal Energy Conversion *MRS Bull.* **33** 366–8

[7] Snyder G J and Toberer E S 2008 Complex thermoelectric materials *Nat. Mater.* **7** 105–14

[8] Zheng X F, Yan Y Y and Simpson K 2013 A potential candidate for the sustainable and reliable domestic energy generation–Thermoelectric cogeneration system *Appl. Therm. Eng.* **53** 305–11

[9] Sharma S, Dwivedi V K and Pandit S N 2014 A review of thermoelectric devices for cooling applications *Int. J. Green Energy* **11** 899–909

[10] Rowe D 2012 Thermoelectrics And Its Energy Harvesting: Materials, Preparation, And Characterization In Thermoelectrics pp 1–12

[11] Ioffe A F, Stil'bans L S, Iordanishvili E K, Stavitskaya T S, Gelbtuch A and Vineyard G 1959 Semiconductor Thermoelements and Thermoelectric Cooling *Phys. Today* **12** 42–42

[12] Cutler M, Leavy J F and Fitzpatrick R L 1964 Electronic Transport in Semimetallic Cerium Sulfide *Phys. Rev.* **133** A1143–52

[13] Rowe D M 2006 *Thermoelectrics Handbook* ed D M Rowe (CRC Press)

[14] Nolas G S, Sharp J and Goldsmid H J 2001 *Thermoelectrics* vol 45 (Berlin, Heidelberg: Springer Berlin Heidelberg)

[15] Bell L E 2008 Cooling, Heating, Generating Power, and Recovering Waste Heat with Thermoelectric Systems *Science (80-.).* **321** 1457–61

[16] Slack G A and Ross R G 1985 Thermal conductivity under pressure and through phase transitions in solid alkali halides. II. Theory *J. Phys. C Solid State Phys.* **18** 3957–80

[17] Limarga A M and Clarke D R 2011 The grain size and temperature dependence of the thermal conductivity of polycrystalline, tetragonal yttria-stabilized zirconia *Appl. Phys. Lett.* **98** 211906

[18] Mamur H, Bhuiyan M R A, Korkmaz F and Nil M 2018 A review on bismuth telluride (Bi 2 Te 3) nanostructure for thermoelectric applications *Renew. Sustain. Energy Rev.* **82** 4159–69

[19] Sootsman J R, Kong H, Uher C, D'Angelo J J, Wu C-I, Hogan T P, Caillat T and Kanatzidis M G 2008 Large Enhancements in the Thermoelectric Power Factor of Bulk PbTe at High Temperature by Synergistic Nanostructuring *Angew. Chemie Int. Ed.* **47** 8618–22

[20] Wang X W, Lee H, Lan Y C, Zhu G H, Joshi G, Wang D Z, Yang J, Muto A J, Tang M Y, Klatsky J, Song S, Dresselhaus M S, Chen G and Ren Z F 2008 Enhanced thermoelectric figure of merit in nanostructured n -type silicon germanium bulk alloy *Appl. Phys. Lett.* **93** 1–4

[21] Ibrahim A M and Thompson D A 1985 Thermoelectric properties of BiSb alloys *Mater. Chem. Phys.* **12** 29–36

[22] Weber L and Gmelin E 1991 Transport properties of silicon *Appl. Phys. A Solids Surfaces* **53** 136–40

[23] Xie J, Ohishi Y, Miyazaki Y, Yusufu A, Muta H, Kurosaki K and Yamanaka S 2015

Thermoelectric properties of Si/SiB3 sub-micro composite prepared by melt-spinning technique *J. Appl. Phys.* **118** 065103

[24] Hochbaum A I, Chen R, Delgado R D, Liang W, Garnett E C, Najarian M, Majumdar A and Yang P 2008 Enhanced thermoelectric performance of rough silicon nanowires *Nature* **451** 163–7

[25] Boukai A I, Bunimovich Y, Tahir-Kheli J, Yu J, Goddard III W A and Heath J R 2008 Silicon nanowires as efficient thermoelectric materials *Nature* **451** 168–71

[26] Neophytou N, Wagner M, Kosina H and Selberherr S 2010 Analysis of Thermoelectric Properties of Scaled Silicon Nanowires Using an Atomistic Tight-Binding Model *J. Electron. Mater.* **39** 1902–8

[27] Tang J, Wang H-T, Lee D H, Fardy M, Huo Z, Russell T P and Yang P 2010 Holey Silicon as an Efficient Thermoelectric Material *Nano Lett.* **10** 4279–83

[28] Galli G and Donadio D 2010 Thermoelectric materials: Silicon stops heat in its tracks *Nat. Nanotechnol.* **5** 701–2

[29] Miura A, Zhou S, Nozaki T and Shiomi J 2015 Crystalline–Amorphous Silicon Nanocomposites with Reduced Thermal Conductivity for Bulk Thermoelectrics *ACS Appl. Mater. Interfaces* **7** 13484–9

[30] Henry A S and Chen G 2008 Spectral Phonon Transport Properties of Silicon Based on Molecular Dynamics Simulations and Lattice Dynamics *J. Comput. Theor. Nanosci.* **5** 141–52

[31] Bux S K, Blair R G, Gogna P K, Lee H, Chen G, Dresselhaus M S, Kaner R B and Fleurial J P 2009 Nanostructured bulk silicon as an effective thermoelectric material

Adv. Funct. Mater. **19** 2445–52

[32] Bux S K, Fleurial J-P and Kaner R B 2010 Nanostructured materials for thermoelectric applications *Chem. Commun.* **46** 8311

[33] Kühn G 1986 W. Kurz, D. J. Fisher, Fundamentals of Solidification. Trans Tech Publications, Switzerland-Germany-UK-USA, 1986 (Erstauflage 1984), 242 Seiten, zahlreiche Abbildungen und Tabellen, Sachwortindex, SFr 54.00, ISBN 0-87849-523-3 *Cryst. Res. Technol.* **21** 1176–1176

[34] Hunt K A J and J D 1966 Lamellar and Rod Eutectic Growth *Met. Soc. AIME* **236** 1129–41

[35] Tiller W A 1958 *Liquid Metals and Solidification* (Cleveland: ASM)

[36] Elmer J W, Allen S M and Eagar T W 1989 Microstructural development during solidification of stainless steel alloys *Metall. Trans. A* **20** 2117–31

[37] Chen H S and Miller C E 1970 A Rapid Quenching Technique for the Preparation of Thin Uniform Films of Amorphous Solids *Rev. Sci. Instrum.* **41** 1237–8

[38] Foote W J 1970 A New Flange Design for O-Ring Seals *Rev. Sci. Instrum.* **41** 1237–1237

CHAPTER II

Experimental Method

2.1 Sample Preparation

All experiments in this work were performed at Kurosaki-Muta laboratory, Osaka University. In the present study, for chapter 3, master ingot were prepared by conventional arc-melting technique. For the work in chapter 4, master ingot were prepared by using the quench-melting technique. Polycrystalline thin ribbons were prepared by melt-spinning technique, while the bulk samples were sintered by spark plasma sintering after preparing the master ingot.

2.1.1 Arc-Melting (AM)

Arc-melting (AM) is a method used for melting metals that are normally to form alloys. The simple model of AM system is shown in Figure 2.1. The heating process is through an electric arc struck among a tungsten (W) rod and metals positioned in a vessel in the copper (Cu) hearth. The Cu hearth has low reactivity with other materials. In vacuum AM, the chamber is first evacuated and then filled with argon (Ar) gas in order to avoid oxidation as Ar being an inert gas does not react with molten metal. The metals can be heated to a temperature up to 2000ºC.

As there are two crucibles in the hearth, a set of two alloys can be prepared in a single evacuation. The system consist of three main part which is the power source, vacuum unit and chiller. A vacuum of 10^{-6} m bar can be attained by the vacuum unit with diffusion and rotary pumps. The Cu hearth and the electrodes are cool down by the cold circulation water from the chiller. After master ingots are melted and solidified, it can be turned over by a tweezer inside the chamber without breaking the vacuum and then re-melted again. The re-melting process is repeated three times or more to attain a fully compositional homogeneity.

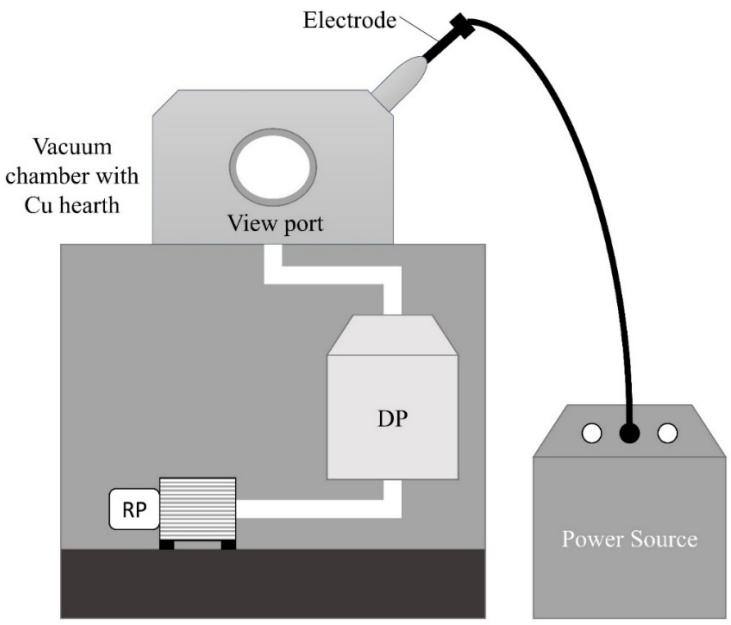

Figure 2.1 Schematic model of arc melting.

2.1.2 Quench-Melting (QM)

The preparing technique of glasses by means of rapid quenching of a melt is historically the most established and it is still the most widely used in the preparation of amorphous chalcogenide materials. The method consists of weighting and mixing the high purity constituents followed by melting in sealed evacuated quartz ampoules by vertical furnace. The melt is continuously rocked to ensure homogenization. Subsequently, the melt will vitrify when cooled by quenching in ice water.

2.1.3 Melt-Spinning (MS)

Melt spinning (MS) is a rapid solidification technique that are used in preparation of many advanced functional materials [1]. The mechanism of the melt spinning is shown in Figure 2.2. By induction heating, small amount of alloy were liquefied inside a crucible. Subsequently, the melted alloy were ejected thru a fine nozzle with pressurization over the controlled-rotating copper roller.

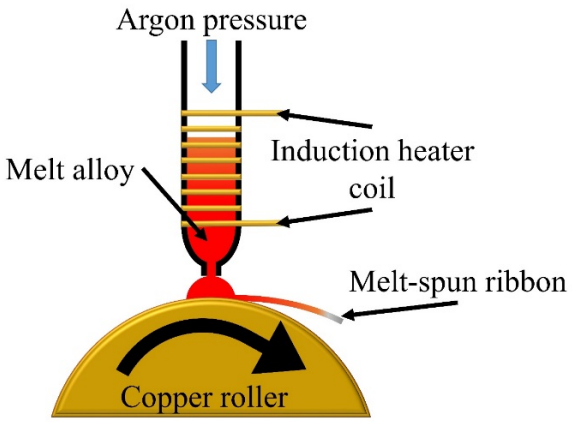

Figure 2.2 The melt-spinning system schematic model

There are several parameters to control, i.e., the atmosphere in the chamber, internal pressure, injection pressure, output current, rotational speed, nozzle diameter, and distance between the nozzle and the copper roller. These parameters determine the size, shape, and thickness of obtained ribbons. Table 2.1 show the listed parameters used in this study. The crucible material is selected according to its low porosity, thermal conductivity, resistance to thermal shock and chemical compatibility.

Table 0.1 The parameters of melt spinning system

Parameter	**Condition**
Roller rotation speed	10 m/s – 52 m/s
Melting atmosphere	Ar atmosphere
Atmospheric pressure	15 kPa – 20kPa
Injection pressure	10 kPa – 20kPa
Distance between roll and nozzle	0.2 mm
Nozzle type	hexagonal boron nitride (h-BN)
Diameter of nozzle	ϕ0.6 mm
Output current	10 A – 15 A

In the cross section, the nozzles are typically circular, which ranges from 50 to 1250 um. They are made by refractory materials. The nozzle materials that are typically used are hexagonal boron nitride (h-BN), graphite, alumina, silicon carbide (SiC), and sapphire. In this study, the h-BN nozzle was adopted to prevent the reaction between the samples and the nozzle. The particular purpose of these nozzles relies on the type of metal to be prepared while the ejection pressure relies intensively on the desired melt delivery rate. Desired melt delivery rate is of great importance for the election pressure. The adoption of higher ejection pressure leads

to the development of the wetting pattern. With this, an improved thermal contact within the substrate and melt puddle can obtained. When the nozzle diameter decrease, there would be an increase of the required ejection pressure. Typically, the solidification rates would be ~100m/s. Transforming the melt to the amorphous structure has been made possible due to the high solidification rates.

2.1.4 Spark Plasma Sintering (SPS)

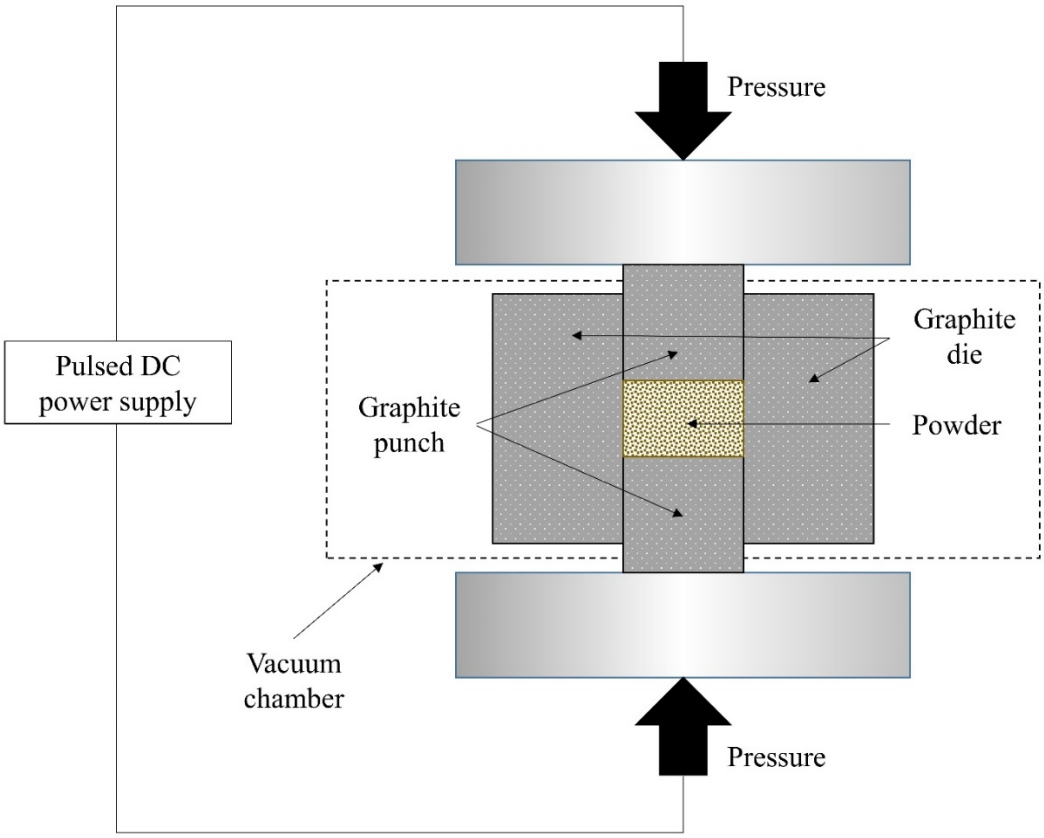

Figure 2.3 The schematic model of spark plasma sintering system

A method to synthesize bulk sample from powder by applying one axis force and pulsated direct electrical current is called spark plasma sintering (SPS). SPS has many benefits compared to ordinary sintering approaches for instance hot isostatic pressing (HIP) and hot-pressing, i.e., rapid and uniform sintering, low grain growth, high energy efficiency, and easy operation [2]. Figure 2.3 demonstrations a schematic model of the SPS method. The powder is weighted into a graphite die. Pulsed direct current is then adapted to the die under pressure. Part of the die surrounding the powder works as resistance paths for applying pulsed direct

current. Heat produced at this resistance can increase temperature of the sample effectively. The air pockets existing among each particle in the powder act as capacitors with the application of alternating current. The temperature gradients within sample must be low in order to homogeneously sinter the sample. Thus, electrical conductivity of the material is the important factor for SPS.

2.2 Characterization Methods

In this work, the thermoelectric and physical properties were characterized by using the laser flash analysis, ZEM-3, X-ray powder diffraction (XRD), field emission scanning electron microscopy (FE-SEM), and energy dispersive X-ray spectrometry (EDS).

2.2.1 X-ray Powder Diffraction (XRD)

To measure phase characterization of sample, powder X-ray diffraction (XRD, Rigaku RINT2000) is used. From the XRD results, unit cell volume, the lattice parameter, and theoretical density can be assessed. Purity phase and present of any impurity phase in the compound can be determine by using material diffraction data set as most materials have unique diffraction patterns. When X-ray strike onto the surface of a crystal, they are moderately scattered by atoms once while some quantity of them passes through. The positioning among atom layers need to be in radiation wavelength and the sample need to be crystalline structure for an X-ray to diffract. When constructive interference (two or more diffract beams wave are in phase with each other) arises, the diffraction pattern will displays a peak. Destructive interference (out of phase) arises and there is no peak. As a high frequency of steady structure is required for diffraction, amorphous entity will not appear in a diffraction pattern while crystalline solids will diffract. A whole number of wavelengths needs to have travelled while inside the substance for the wave which is in phase with the wave to redirect from the surface. This can be express in an equation well-known as Bragg's Law [3];

$$2d \sin\theta = n\lambda \tag{2.1}$$

where d is the little spacing in a crystalline sample, λ is the wavelength, while n is diffraction order integer.

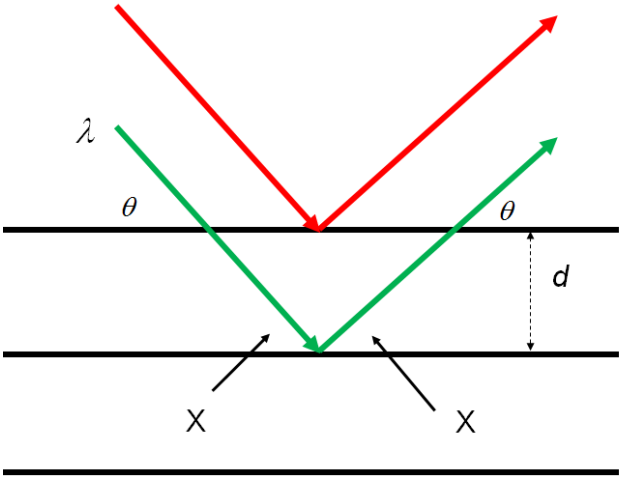

Figure 2.4 Relationship among the wavelength λ, angle θ, and atomic spacing d.

A powder XRD apparatus consists of an X-ray detector, X-ray source, a way to vary angle and a specimen stage as shown in Figure 2.5. At angle θ, the X-ray is directed to the specimen. The detector opposing the source, detects the X-ray intensity. Angle of the detector will always remain 2θ above the source path, while the incident angle increases during the operation.

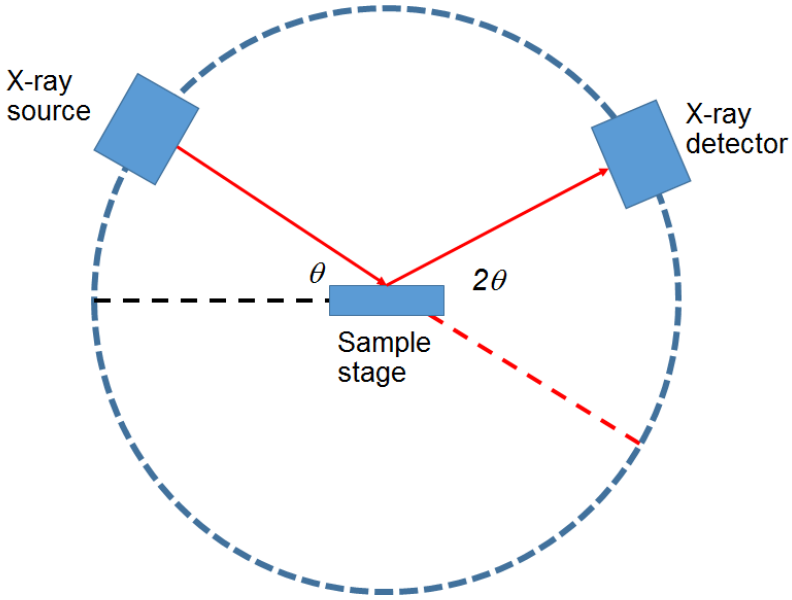

Figure 2.5 Diagram of X-ray diffraction tool

2.2.2 Field Emission Scanning Electron Microscopy (FE-SEM)

Surface morphology can be observe using the scanning electron microscopy (SEM). In this study, images of solid surface were obtained with the field emission scanning electron microscopy (FE-SEM). The equipment apply a concentrated beam of high-energy electrons to produce range of signals at the dense samples surface. Schematic model of the SEM is displayed in Figure 2.6 [4]. Accelerated electrons in SEM, transport a considerable quantities of kinetic energy. Once incident electrons are decelerated in the dense sample, this energy is degenerate as a range of signals created by electron to sample interfaces. Particular signals comprise of secondary electrons, diffracted backscattered electrons (EBSD), backscattered electrons (BSE), and so on. The secondary electrons are usually used for showing contrasts in configuration in multiphase samples. Image showing the morphology of the surface is generated by scanning the specimen and gathering the secondary electrons using a detector.

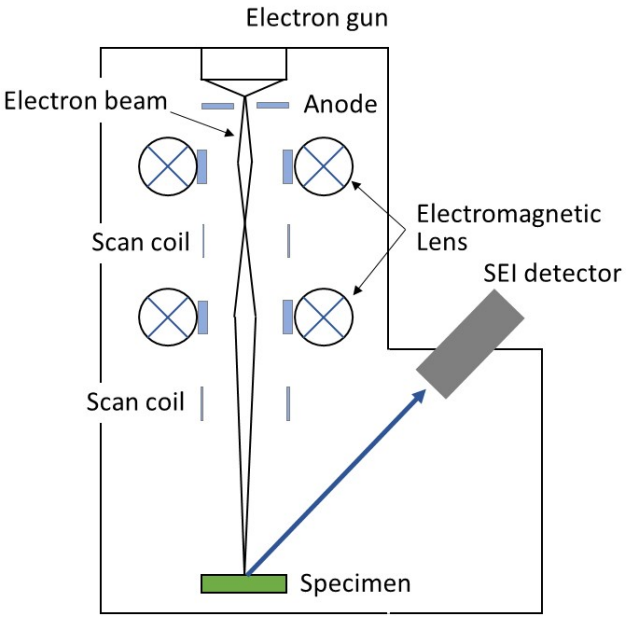

Figure 2.6 Diagram model of scanning electron microscopy

2.2.3 Energy-Dispersive X-Ray Spectroscopy (EDS)

Energy dispersive X-ray spectroscopy (EDS or EDX) is a chemical microanalysis method used in concurrence with the SEM is called. The EDS identifies X-rays released from specimen throughout bombardment thru an electron beam to identify the elemental composition of examined volume. Phases or features as little as 1 μm or less can be evaluated.

Electrons are emitted from atoms comprising the specimen surface once the specimen is bombarded by the SEM electron beam. The resulting electron vacancies are occupied by electrons from a greater state, and an X-ray is released to balance the energy change amongst two electrons' states. X-ray energy depends on the element.

EDS X-ray detector compute the relative abundance of released X-rays versus their energy. It creates a charge pulse that is proportional to the energy of the X-ray when an incident X-ray strikes the detector. The charge pulse is altered to a voltage pulse by a charge-sensitive preamplifier. The signal is sent to a multichannel analyzer where the pulses are arranged by voltage. For each incident X-rays energy determined from the voltage measurement is sent to a computer for display and further data estimation. To determine the elemental composition of the specimen volume, the spectrum of X-ray energy versus counts is calculated. In Figure 2.7, the process of EDS is simply described.

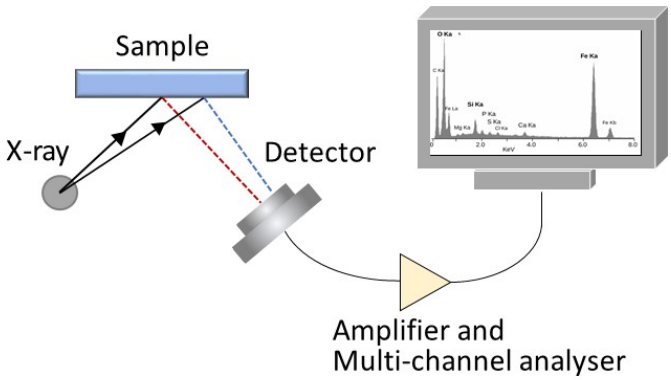

Figure 2.7 Schematic illustration of EDS

2.2.4 ZEM-3

Thermopower measuring device (ULVAC ZEM-3) was implemented in a helium atmosphere to measure the electrical properties. The diagram of ZEM-3 is showed in Figure 2.8. To characterized the electrical resistivity, ρ, the standard four probe technique with a consistent current is used. The equation of the electrical resistivity is:

$$\rho_{sample} = \frac{V_{sample}}{V_{ref}} R_{ref} \frac{A_{sample}}{L_{sample}} \tag{2.2}$$

where V_{sample} is the voltage within the two probes positioned on the specimen, V_{ref} is the voltage dropped through the standard resistor, R_{ref} is a standard resistor together with the apparatus, A_{sample} is the specimen cross section, and L_{sample} is the length separating two thermocouples on the specimen. The Seebeck coefficient (S) is given by the subsequent equation:

$$S = \frac{V_{sample}}{T_H - T_L} \tag{2.3}$$

where, T_L and T_H are the absolute temperatures measured at two points from V_{sample} was measured. The average value of three measured temperature gradients ΔT of 20, 30, and 40 K among two blocks at temperature T measured as the results value.

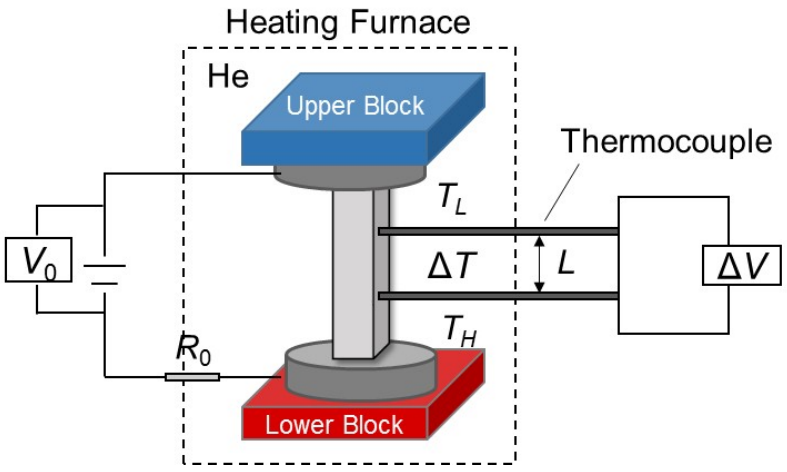

Figure 2.8 Schematic illustrating of ZEM-3 for measuring electrical properties

2.2.5 Laser Flash

With the distribution of temperature changing, there is a trouble that heat transfer is short. Thermal diffusivity is a concept that the fundamental quantity makes the entrance into the heat transfer situation that is unsteady. There is a formula with the relation to the steady-state thermal conductivity.

$$\kappa = dCD \tag{2.4}$$

where D is the thermal diffusivity, C the specific heat and d the sample density. In this equation, it can be found that D, thermal diffusivity, can help to compute κ (thermal conductivity). To obtain the value of D, the experiment has to use a laser flash in Netzsch LFA457 instrument. In addition, D is to judge the speed of the body changing temperature. For the purpose of measure a material's thermal diffusivity, it is demanded to heat single side of the specimen and to measure the temperature trend of the other side.

It needs a period of time to heat the sample and increase temperature on the rear surface. This time is useful to determine the through-plane diffusivity and calculate the through-plane thermal conductivity under the given density and specific heat. Figure 2.9 makes a particular explanation of the through-plane measurement.

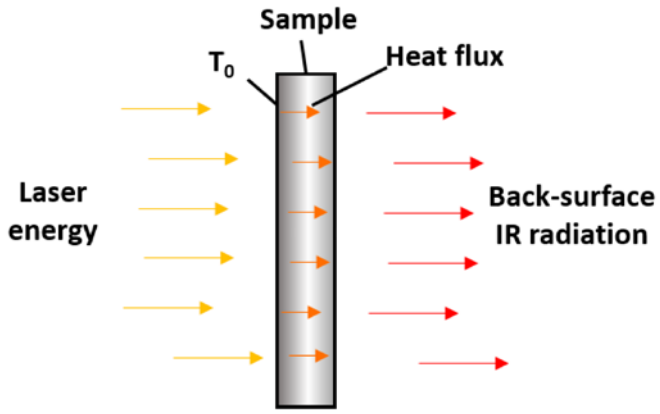

Figure 2.9 Schematic illustration of through-plane measurement

The experiment takes a disk as a sample which is 12.7 mm in diameter, a standard one, and has a thickness range within 1mm to 3 mm. The Netzsch LFA457 Laser Flash system makes the disk aligned in a tantalum tube furnace, namely the position between a neodymium glass laser and an indium antimonite (lnSb) IR detector. If a thermocouple touches the disk, it will control the disk as well as its surroundings when temperature changes within the range of 300K to 1273K. When there is a stable state on the condition that the specimen reaches to the expected temperature, the laser, within a few minutes, shoots several times over a span, and, at the same time, an instrument records relative data of individually laser "shot". The laser beam shoots energy which the front surface of the specimen assimilates, thus, a heat pulse goes over specimen thickness. In addition, the increase of temperature is next to nothing. The temperature is in the most ideal range, which is beneficial from changeable filters between the furnace and the laser. It can be found that the back surface of the specimen is focused by a lens onto the

detector. Besides, there is an amplified trend of the temperature increase signal vs. time, which is logged by a high speed AID converter. It provides an illustration of a temperature rise curve in practice in Figure 2.10.

The equipment is completely automated so that it can command systems. Moreover, it also records, analyzes and reports thermal diffusivity and specific heat, calculating thermal conductivity. Before test, a graphite film is utilized to cover the sample without a naturally high value of emissivity or absorptivity. As a result, graphite enhances not only the energy that the laser side absorbs but also the temperature of the sample backside.

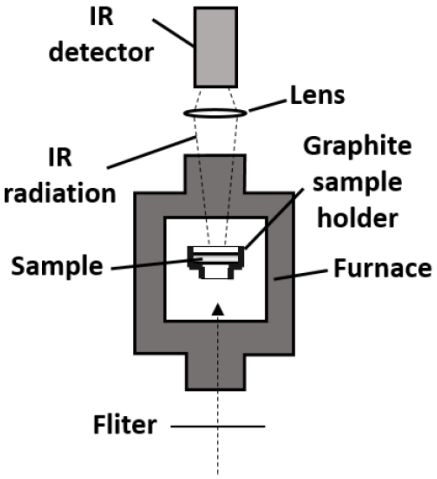

Figure 2.10 Schematic illustration of laser flash instrument

If the primary temperature dissemination inside a thermally insulated solid of uniform thickness L is $T(x, 0)$, the temperature circulation at any future time t is given as subsequent, where α is the thermal diffusivity.

$$T(x,t) = \frac{1}{L}\int_0^L T(x,0)dx + \frac{2}{L}\sum_{n=1}^{\infty}\exp\left(\frac{-n^2\pi^2\alpha l}{L^2}\right)\cos\frac{n\pi x}{L}\int_0^L T(x,0)\cos\frac{n\pi x}{L}dx \qquad (2.5)$$

If a pulse of radiant energy Q is promptly and uniformly absorbed in the small depth g at the front surface $x = 0$ of a thermally insulated solid of uniform thickness L, the temperature distribution at that moment is given by $T(x,0) = Q/DCg$ for $0 < x < g$ and $T(x,0) = 0$ for $g < x < L$. With this primary condition, equation (2.7) can be drafted.

$$T(x,t)=\frac{Q}{DC_{\mathrm{p}}L}\left[1+2\sum_{n=1}^{\infty}\cos\frac{n\pi x}{L}\frac{\sin(n\pi g/L)}{n\pi g/L}\exp\left(\frac{-n^2\pi^2\alpha l}{L^2}\right)\right] \tag{2.6}$$

As g is a very small amount for opaque materials, it follows that $\sin(n\pi g/L) \approx n\pi g/L$. At the rear surface where $x = L$, the temperature antiquity can be written by equation (2.7).

$$T(L,t)=\frac{Q}{DC_{\mathrm{p}}L}\left[1+2\sum_{n=1}^{\infty}(-1)^n\exp\left(\frac{-n^2\pi^2\alpha l}{L^2}\right)\right] \tag{2.7}$$

Two dimensionless factors, ω and V can be clear as next interactions, where T_{M} denotes the highest temperature at the rear surface.

$$V(L,t)=T(L,t)/T_{\mathrm{M}} \tag{2.8}$$

$$\omega=\pi^2\alpha l/L^2 \tag{2.9}$$

The combination of (2.7), (2.8), and (2.9) produces the equation (2.10).

$$V=1+2\sum_{n=1}^{\infty}(-1)^n\exp\left(-n^2\omega\right) \tag{2.10}$$

Equation (2.10) is outline in Figure 2.11. From equation (2.10) and Figure 2.11, thermal diffusivity α is realized: when ω is equivalent to 1.38, V is equivalent to 0.5 and the following correlation is attained.

$$\alpha=\left(1.38L^2/\pi^2t_{1/2}\right) \tag{2.11}$$

The parameter $t_{1/2}$ is the time requisite for the back surface to reach half of the maximum temperature increase.

Without attempting a rigorous analysis, an effective temperature T_{e} is picked as the time average of the mean of the front and back surface reaches one-half of its maximum value. The dimensionless parameter $V(L,t)$ at the rear surface was given by equation (2.12). The dimensionless parameter $V(0,t)$ at the front surface obtained in a similar manner is given by the following.

$$V(0,t) = 1 + 2\sum_{n=1}^{\infty} \exp(-n^2\omega) \tag{2.12}$$

The mean value of $V(L,t)$ and $V(0,t)$ is

$$\frac{V(0,t)+V(L,t)}{2} = 1 + 2\sum_{n=1}^{\infty} \exp(-4n^2\omega) \tag{2.13}$$

and the effective value of V is expressed as equation (2.15).

$$V_e = 1 + \frac{2}{\omega_{1/2}} \int_0^{\omega_{1/2}} \sum_{n=1}^{\infty} \exp(-4n^2\omega) d\omega$$

$$= 1 + \frac{2}{4(1.38)} \left[\sum_{n=1}^{\infty} \frac{1}{n^2} \left(1 - \exp(-4n^2 \times 1.38)\right) \right] \tag{2.14}$$

$$= 1.6$$

Finally, the effective temperature is given by

$$T_e = V_e T_M = 1.6 T_M \tag{2.15}$$

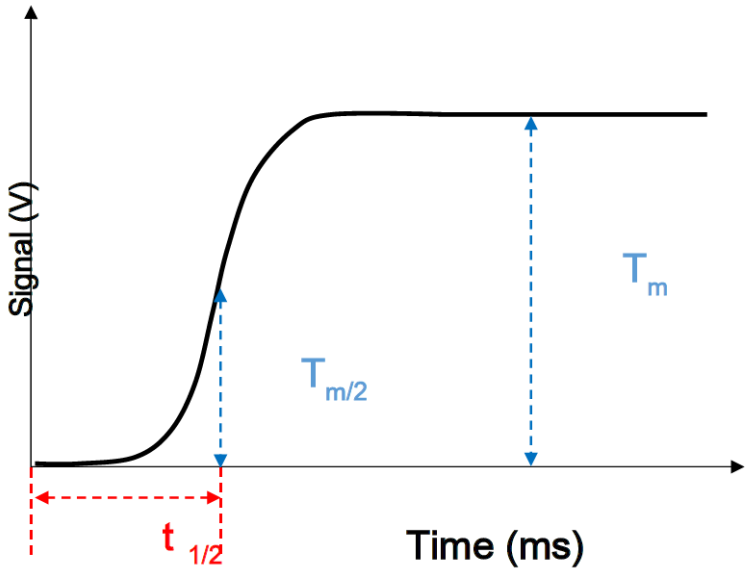

Figure 2.11 Dimensionless plot of rear surface temperature history

2.3 Reference

[1] Inoue C S A *Bulk Metallic Glasses* (Taylor & Francis)

[2] Guyot P, Rat V, Coudert J F, Jay F, Maître A and Pradeilles N 2012 Does the Branly effect occur in spark plasma sintering? *J. Phys. D. Appl. Phys.* **45** 092001

[3] Barber D J 1992 J. P. Eberhart Structural and Chemical Analysis of Materials—X-ray, electron and neutron diffraction—X-ray, electron and ion spectroscopy–Electron microscopy. (Translated by J. P. Eberhart), Chichester and New York (J. Wiley and Sons), 1991, xxx + 545 pp. Price £95.00 *Mineral. Mag.* **56** 135

[4] Burge R E 1980 An introduction to microscopy by means of light, electrons, X-rays or ultrasound *J. Biomed. Eng.* **2** 156

CHAPTER III

Thermoelectric Properties of *p*-Type Si/$CrSi_2$ Eutectic Alloy Fabricated by Melt-Spinning Technique

3.1 Introduction

Silicon (Si)-based materials are successful examples of the enhancement of the thermoelectric Silicon (Si)-based materials are successful examples of the enhancement of the thermoelectric performance by nanostructuring [1–6]. Bulk Si crystals have a poor *ZT* for practical use because of their high κ values of more than 100 W/mK at room temperature, despite their favorable *S* and ρ values [7].

Recent papers have reported a dramatic reduction in the thermal conductivity, κ, together with high figure of merit, *ZT*, by nanostructuring in low-dimensional systems such as Si nanowires [8–10] and Si thin films with nanoholes [11,12]. In bulk materials, the Si nanocrystals [13–15] that are formed by powder metallurgical methods have been reported to have a thermal conductivity of approximately 10 W/mK at room temperature and a relatively high *ZT* of approximately 0.7 at temperatures of ~1,200 K. However, this type of Si nanoparticle processing leads to oxide formation, the segregation of impurities and amorphous areas at the grain boundaries. These factors tend to reduce the carrier mobility with a decrease in grain size, leading to a poor thermoelectric power factor ($=S^2/\rho$). Additionally these sample fabrication requires complex procedure and much labor such as the long ball milling time. It is hypothesized that self-assembled nanostructures avoid these problems because the naturally formed interface tends to be relatively clean and smooth. Nanocrystalline composites of Si and silicide are known to self-form from amorphous thin films composed of Si and a metallic element, and a low thermal conductivity of 2.2 W/mK has been reported [16] in a molybdenum (Mo)-Si nanocrystal. However, a bulk Si-based nanomaterial self-assembly process has not been reported to date. We focused on the Si-chromium (Cr) system, which has a typical eutectic point between Si and chromium disilicide ($CrSi_2$), as shown in the phase diagram [17] in Fig. 3.1. $CrSi_2$ is a p-type degenerate semiconductor that has attracted attention as a prospective thermoelectric material for many years [18–20]. The p-type doping of $CrSi_2$ has been reported to achieve higher performance than n-type doping due to the high anisotropy of the resulting

electrical conductivity [21] and its thermal stability in air below 1,050 K, making it a promising candidate for high-temperature applications [22]. The Seebeck coefficient and the electrical conductivity of nanocomposite thin films of $CrSi_2$ and Si have been reported [23,24], but carrier-doping into the Si phase has not been conducted.

In this work, an approach for the fabrication of Si-based nanostructured bulk materials is described that is based on a self-assembly process from melting alloys. Generally, eutectic alloys are fine microstructured composites that are self-assembled directly from a melt with some structural regularity. Their feature size decreases with an increase in the growth rate with a minimum undercooling condition [25]. To reduce the size of the eutectic microstructure to the nanometer scale, a rapid solidification technique is applied to a eutectic system of Si and metal silicide.

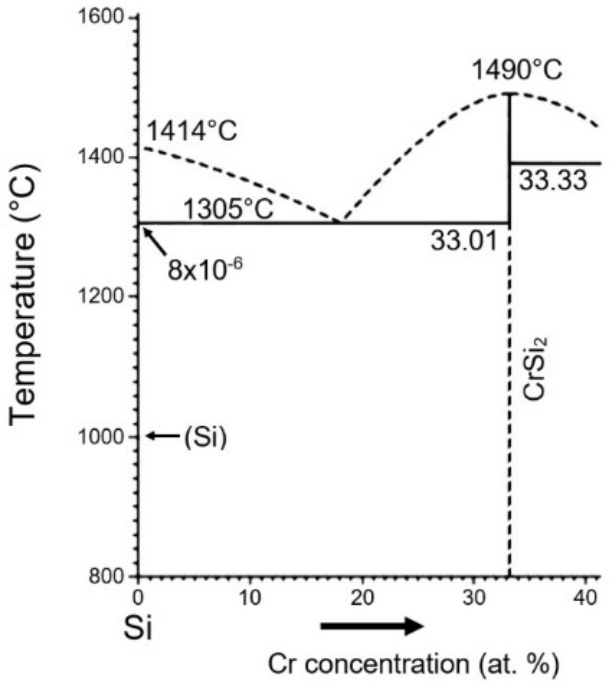

Figure 3.1 Binary phase diagram of the Si-Cr system (Si-rich side only)

3.2 Experimental Procedures

The melt spinning method is used with a cooling rate that exceeds 10^5 K/s [26], and the cooling rate increases with the wheel rolling speed. Master ingots with a nominal composition of $Cr_{14.9}(Si_{1-x}B_x)_{85.1}$ were first prepared by arc melting (AM) in an argon (Ar) atmosphere from high-purity semiconductor-grade Si (99.999999999%), Cr (99.9%), and boron (B) (99.9%).

The mass loss rates were less than 0.1% throughout the arc melting process. A portion of the obtained arc-melted sample was melted by induction heating in a hexagonal boron nitride (h-BN) tube with a 0.6 mm diameter nozzle to prevent reactions between the sample and the nozzle. Melt spinning (MS) was performed with the melted sample ejected under an Ar atmosphere at a pressure of 20 kPa onto a copper (Cu) single-roll system that was operated at wheel linear speeds of 10 m/s to 52 m/s. The MS ribbon fabricated at the speed of 52 m/s was annealed at 723 K for 72 h for evaluation of the structure stability.

The samples were characterized by powder x-ray diffraction (XRD) analysis using an x-ray diffractometer (Ultima IV, Rigaku Co.) with Cu Kα radiation and secondary electron images using a field-emission scanning electron microscope (FE-SEM, JEOL JSM-6500F) and attached energy dispersive X-ray (EDX) analysis. The thermoelectric properties along the longitudinal direction of the ribbons, i.e., perpendicular to the direction of the eutectic growth, were measured. The electrical resistivity (ρ) and Seebeck coefficient (S) of the samples were determined simultaneously in a He atmosphere at temperatures ranging from room temperature to 773 K by a four-point technique and a static direct-current method using a ZEM-3 instrument system (ULVAC-RIKO, Inc.) with a test holder for ribbon measurement in the in-plane direction. The sample was attached to test holder and mounted between the electrodes. The upper electrode serve as a heating element. A platinum (Pt) foil is positioned to electrically connect the electrodes with the sample's surface. Two ceramics hex nuts were used to tighten the foil to the base and Silver (Ag) paste was used to contact the foils with the sample. The test holder base was made of Alumina and does not influenced with the electrical measurements, and the electrical contacts were established only between the electrodes and the sample. A schematic representation of the system with the test holder is shown in Fig 3.2. For the determination of ρ, a cross-section of the sample was evaluated using the mass, the density, and the length of the sample. The sample density was estimated from the volume fraction of Si and $CrSi_2$ phases. The densities of each phase were assumed to Si: 2.33 g/cm3, $CrSi_2$: 4.98 g/cm3. The effect of B on the densities was neglected. The thermal diffusivity was collected with an AC calorimetric method [27] using a LaserPIT (ULVAC-RIKO, Inc.) system at room temperature. The heat capacity, Cp, was obtained from previously reported values for Si [28] and $CrSi_2$ [19]. In this experiment, the contact surface were probed for electrical properties and thermal diffusivity measurement. Typically, one sample was selected from the ribbons and measured several times repeatedly. The uniformity of sample thickness was confirmed by SEM observation.

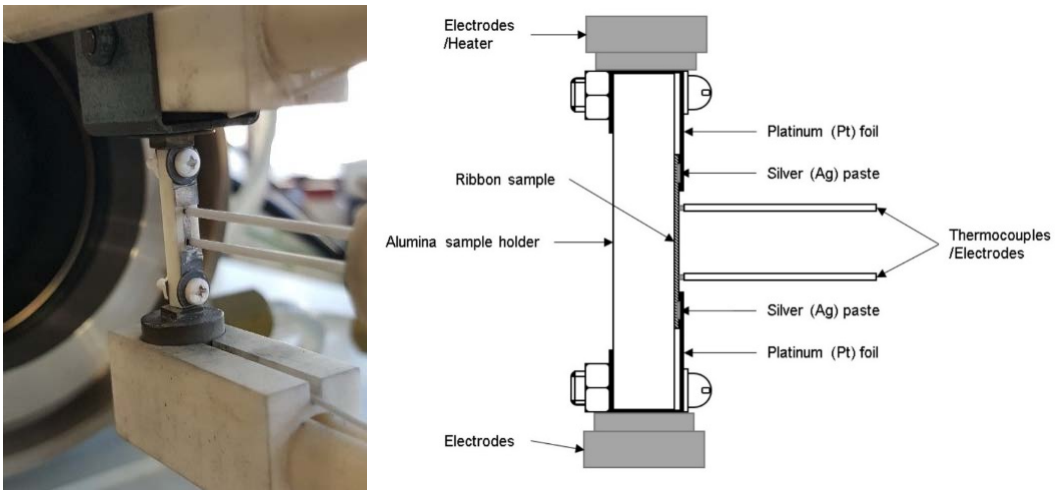

Figure 3.2 Schematic view of the sample inside the ZEM-3 measurement system

3.3 Results and Discussion

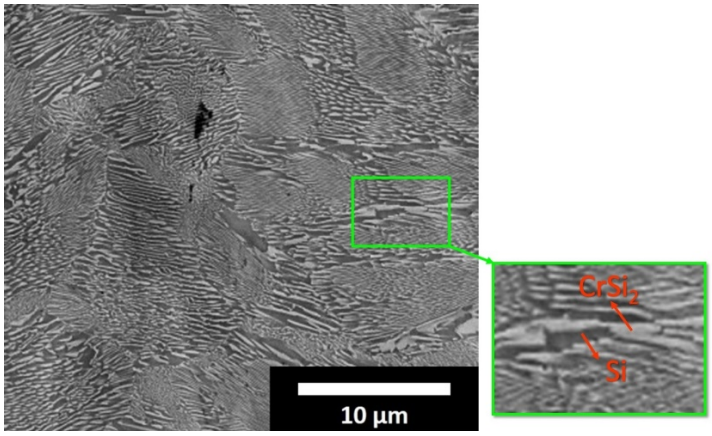

Figure 3.3 Scanning electron micrograph of the $Cr_{14.9}(Si_{0.99}B_{0.01})_{85.1}$ alloy prepared by arc melting (AM)

Our preliminary studies indicate that the eutectic composition is $Cr_{14.9}Si_{85.1}$, although values from 12–18 Cr at.% have been reported [29–31]. The $Cr_{14.9}(Si_{0.99}B_{0.01})_{85.1}$ alloy prepared by arc melting had a fine eutectic structure with a typical grain size of ~1 µm, as the scanning electron microscope (SEM) image shows in Fig. 3.3. Except for the black holes, EDX analysis indicates that the white areas in the SEM image correspond to $CrSi_2$ and the gray areas to Si. B was not detected due to the low fraction and small atomic number. The volume fraction of Si was estimated by image analysis method using SEM image. The estimated value is 67%, which agrees with the calculated fraction from the molar ratio and densities (Si: 2.33 g/cm^3, $CrSi_2$: 4.98 g/cm^3).

Fig. 4 shows the powder XRD patterns of the $Cr_{14.9}(Si_{0.99}B_{0.01})_{85.1}$ bulk sample prepared by arc melting and ribbon samples prepared by melt spinning. The powder XRD pattern confirms that the melt-spun sample is a two-phase alloy consisting of Si and $CrSi_2$ while the arc-melted sample contains a small amount of chromium diboride (CrB_2). A few small peaks corresponding to $CrSi_2$ [32] were observed in addition to a peak for Si [33], indicating that composites composed of Si and $CrSi_2$ were successfully formed. The peaks of the melt-spun sample were significantly broader than those of the arc-melted alloy. The broad XRD peaks represent a small crystallite size or strain in the grain for the eutectic Si-$CrSi_2$ sample.

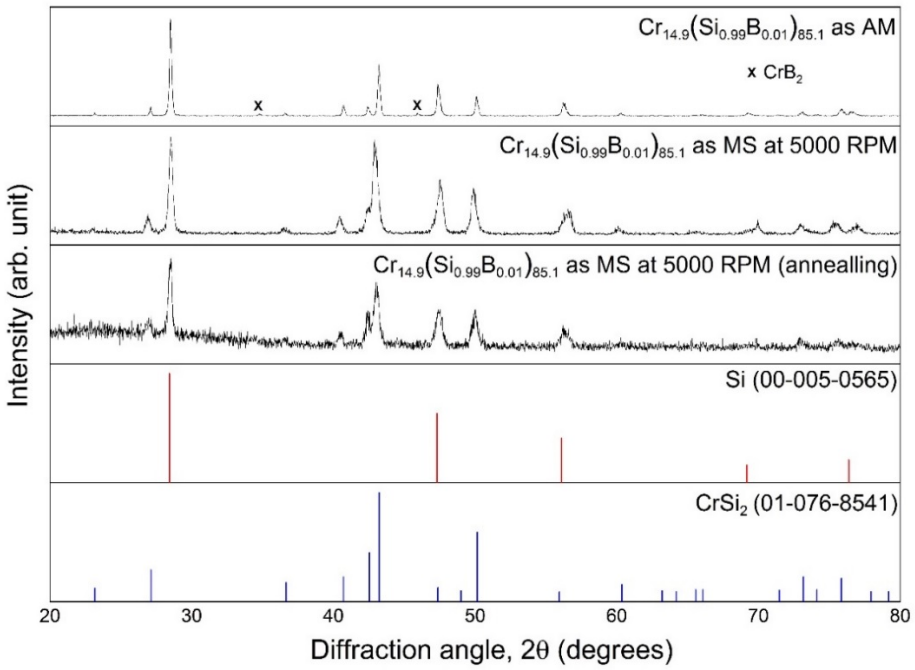

Figure 3.4 Scanning electron micrograph of the $Cr_{14.9}(Si_{0.99}B_{0.01})_{85.1}$ alloy prepared by arc melting (AM)

The melt-spun samples have a long ribbon-like shape with a thickness of 1–40 μm, which decreases with an increase in the roll speed, and a width of 1–3 mm was obtained, as shown in Fig. 3.5 (a). Fig. 5 (b)–(h) show SEM images of the $Cr_{14.9}(Si_{0.99}B_{0.01})_{85.1}$ sample that was melt-spun at 52 m/s. The images were obtained at a fracture cross-section that was perpendicular to the longitudinal direction of the ribbon, as shown in Fig. 3.5 (b), 3.5 (c), and 3.5 (d), on a polished plane parallel to the ribbon surface, as shown in Fig. 3.5 (e) and 3.5 (f), and surface after a post-annealing treatment (723 K, 72 h) as shown in Fig. 3.5 (g) and 3.5 (h). The side of the ribbon that contacts the copper roller is defined as the contact surface, and the other side is defined as the free surface. The cross-section image shows a stripe pattern that

represents alternating layers of the $CrSi_2$ and Si phases that occupy approximately 90% of the sample that is near the free surface in Fig. 3.5 (c), while the neighborhood of the contact surface has a more complicated structure of randomly oriented short $CrSi_2$ rods in a Si matrix in Fig. 3.5 (d). Images of the plane parallel to the surfaces show maze-like patterns of $CrSi_2$ strips in the Si matrix, with a remarkably fine and uniform spacing of approximately 30 nm.

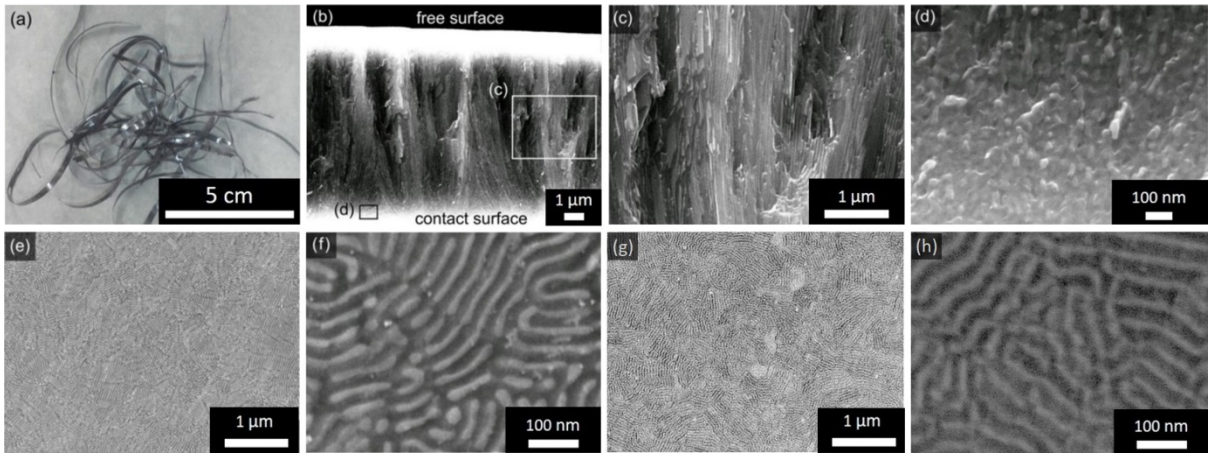

Figure 3.5 Scanning electron micrograph of the $Cr_{14.9}(Si_{0.99}B_{0.01})_{85.1}$ alloy prepared by arc melting (AM)

These images show that most of the melt-spun sample is composed of a well-organized lamellar structure aligned vertically to the ribbon surface, indicating the occurrence of unidirectional solidification from the contact surface to the free surface of the ribbon. The lamella spacing observed in the sample prepared at the highest speed of 52 m/s is 20–35 nm, corresponding to a Si-layer thickness of 12–20 nm, which increases with the depth from the contact surface. It is noted that the lamellar structure has high stability upon solidification, so that no transition to an amorphous phase occurs, as has frequently been observed in melt-spun eutectic alloys. The average eutectic spacing of the samples increases with a decrease in the wheel speed. In a sample melt-spun at less than 10 m/s, virtually no aligned lamellar structure can be observed; instead, a micrometer-sized structure with disordered interfaces is dominant. The structure is shown in Fig. 3.5 (g) and 5 (h), does not change after the post-annealing treatment (723 K, 72 h). Therefore, the structure appears to be stable at the condition.

The temperature dependences of ρ, S and the power factor of the sample that was melt-spun at 52 m/s are plotted in Fig. 3.6. For comparison, measurements of bulk samples prepared by the arc melting of $Cr(Si_{0.99}B_{0.01})_2$, $Si_{99}B$ and eutectic $Cr_{14.9}(Si_{0.99}B_{0.01})_{85.1}$ alloy are also

plotted. The arc-melted sample has a relatively high thermoelectric power factor (=S^2/ρ) of 2.0 mW/mK^2 with a positive Seebeck coefficient at room temperature, which is much higher than the reported value for a $CrSi_2$ bulk material of approximately 1.5 mW/mK^2. The resistivity of the melt-spun sample at room temperature is 4.4 μΩm as shown in Fig. 3.6 (a), which contrasts with the expectation that the resistivity of nanostructured materials is larger than that of bulk materials because of carrier scattering at the grain boundary. Considering the simultaneous decrease in *S* as shown in Fig. 3.6 (b), this low resistivity can be explained by an increase in the carrier concentration. In view of the disappearance of CrB_2 peaks in the XRD pattern of melt-spun sample, we speculate that the increase of carrier concentration caused oversaturation of B in the Si and $CrSi_2$ phases. Broadness of the XRD peaks is almost same, which correspond to the fact that the structure does not change by the annealing. It is confirmed by SEM observation. CrB_2 phase was not detected in the annealed sample. However, the electrical resistivity and Seebeck coefficient increased, indicating the carrier concentration decreased by the annealing. It may be caused by a decrease of solute B amount.

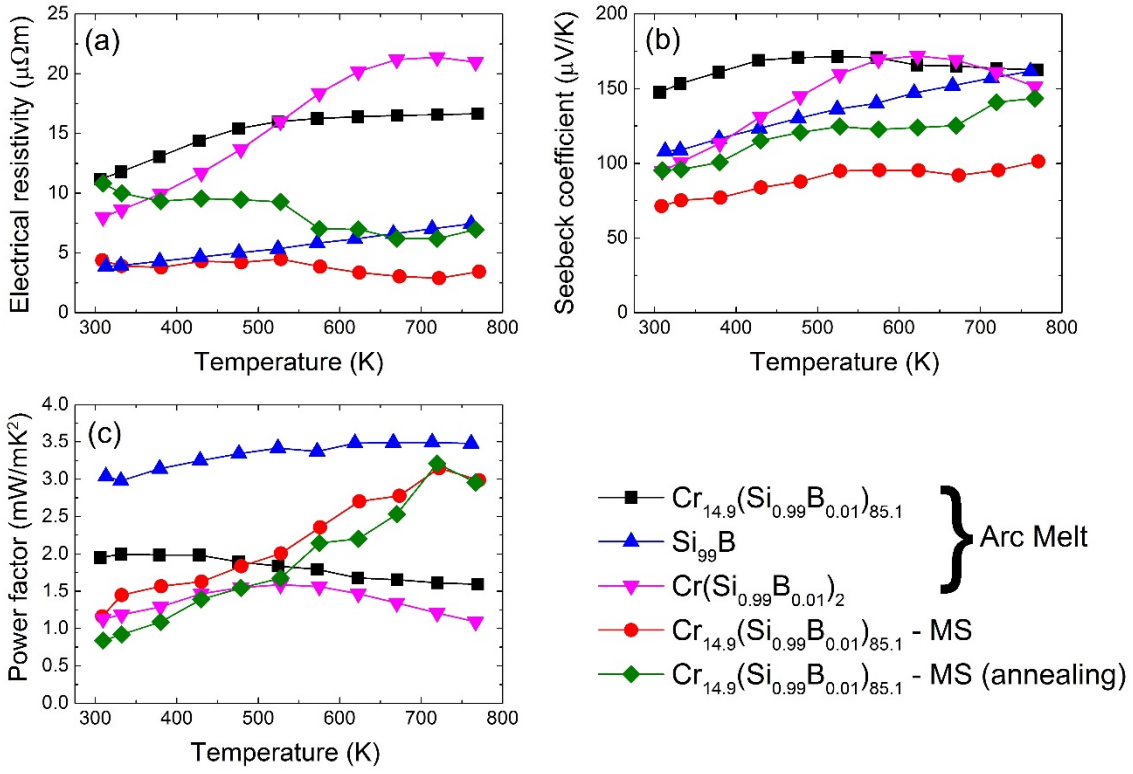

Figure 3.6 Temperature-dependent (a) electrical resistivity, (b) Seebeck coefficient, and (c) power factor of the melt-spun and the arc-melted $Cr_{14.9}(Si_{0.99}B_{0.01})_{85.1}$ eutectic alloy, $Si_{99}B$ and $CrSi_2$

The power factor of the melt-spun sample is 1.2 mW/mK^2 at room temperature as shown in Fig. 3.6 (c), which is lower than that of the bulk sample. However, the temperature dependence is positively opposite to that of the bulk sample, the value increased with increasing the temperature and reached 3.0 mW/mK^2 at 773 K. The power factor is relatively large as a Si-based nanostructured material. Generally the nanostructuring decreases the power factor due to the increased carrier scattering by grain boundary and segregation. The high power factor of the melt-spun sample can be explained by the better optimized carrier concentration and/or the weak carrier scattering at interface between the Si and $CrSi_2$ phases. The interfaces naturally formed by phase separation, hence appear to keep clean for the samples. Such desirable structure can be achieved by this fabrication technique.

Table 3.1 summarizes the power factor, κ, and figure of merit, ZT, at room temperature for the arc-melted sample and the sample melt-spun at 52 m/s. The thermal conductivity of arc-melted alloy was found to be 34 W/mK at room temperature, which is reasonable for a compound consisting of heavily doped Si with a thermal conductivity of ~50 W/mK and $CrSi_2$ with a thermal conductivity of ~10 W/mK, considering that the volume fraction of the Si phase is 67% in the alloy. In the melt-spun samples, κ decreases significantly and the value is 12 W/mK, which is 1/3 that of the arc-melted sample with the same composition. The κ still maintaining at the value of 12 W/mK after the post-annealing treatment. It is noted that the melt-spun sample at 10 m/s exhibits approximately the same κ as the arc-melted sample. The result suggests that the reduction in κ is caused by the phonon scattering at grain boundary and interface, depending on the grain size and the cooling rate. The reduction in power factor at room temperature is relatively small as shown in Fig. 3.6 (c), on the contrary, increases at high temperature. These results indicates that the nanostructuring using the rapid solidification of a melt with a eutectic composition is a promising method to improve the thermoelectric performance, which achieve strong reduction in thermal conductivity while maintaining the power factor.

Table 3.1 Seebeck coefficient (S), electrical resistivity (ρ), thermal conductivity (κ), power factor (PF), and figure of merit (ZT) for the $Cr_{14.9}(Si_{0.99}B_{0.01})_{85.1}$ prepared by arc melting (AM) and melt spinning (MS)

Preparation method	S (μV/K)	ρ (μΩm)	κ (W/mK)	PF (mW/mK^2)	ZT
Arc melting	148 (300 K) 163 (773 K)	11.2 (300 K) 16.7 (773 K)	34 (300 K)	2.0 (300 K) 1.6 (773 K)	0.017 (300 K)
MS at 52 m/s	71 (300 K) 101 (773 K)	4.4 (300 K) 3.4 (773 K)	12 (300 K)	1.2 (300 K) 3.0 (773 K)	0.030 (300 K)

The decrease in κ directly enhances the *ZT*, and the value of 0.03 obtained at room temperature is high for a Si-based bulk nanomaterial without Ge. The best *ZT* at room temperature reported for bulk nanocrystalline Si has been 0.023 [13]. Considering the temperature dependence of thermal conductivity of bulk Si [13] and $CrSi_2$ [19], which monotonically decreases with increasing temperature up to 800 K, the *ZT* value is expected to increase with temperature according to the temperature dependence of the power factor.

Densification of the ribbon sample without the microstructure change should be considered for thermoelectric energy conversion applications. Rapid and low-temperature sintering technique, such as a spark plasma sintering method [34], is required.

3.4 Conclusion

Using the melt spinning, $Si/CrSi_2$ eutectic alloys form an unprecedented fine lamellar structure that is aligned in a vertical manner to the ribbon surface with a spacing range of 20–35 nm. It is demonstrated that the thermal conductivity can be reduced to 1/3 of that of the bulk eutectic alloy of the same composition, thus increasing *ZT*. The power factor does not decrease but rather increases significantly at higher temperatures. The obtained *ZT* value is 0.03 at room temperature and is estimated to increase at higher temperature. The effect of inhomogeneity inside the sample was difficult to evaluate. It requires further studies. This study thus demonstrates the utility of a rapid solidification technique for application to Si-based eutectic alloys for the fabrication of high-performance thermoelectric materials.

3.5 Reference

[1] Rao A M, Ji X and Tritt T M 2006 Properties of Nanostructured One-Dimensional and Composite Thermoelectric Materials MRS Bull. 31 218–23

[2] Snyder G J and Toberer E S 2008 Complex thermoelectric materials Nat. Mater. 7 105–14

[3] Szczech J R, Higgins J M and Jin S 2011 Enhancement of the thermoelectric properties in nanoscale and nanostructured materials J. Mater. Chem. 21 4037–55

[4] Dresselhaus M S, Chen G, Tang M Y, Yang R G, Lee H, Wang D Z, Ren Z F, Fleurial J-P and Gogna P 2007 New Directions for Low-Dimensional Thermoelectric Materials Adv. Mater. 19 1043–53

[5] Zebarjadi M, Esfarjani K, Dresselhaus M S, Ren Z F and Chen G 2012 Perspectives on thermoelectrics: from fundamentals to device applications Energy Environ. Sci. 5 5147–62

[6] Mori M, Shimotsuma Y, Sei T, Sakakura M, Miura K and Udono H 2015 Tailoring thermoelectric properties of nanostructured crystal silicon fabricated by infrared femtosecond laser direct writing Phys. status solidi 212 715–21

[7] Weber L and Gmelin E 1991 Transport properties of silicon Appl. Phys. A Solids Surfaces 53 136–40

[8] Hochbaum A I, Chen R, Delgado R D, Liang W, Garnett E C, Najarian M, Majumdar A and Yang P 2008 Enhanced thermoelectric performance of rough silicon nanowires Nature 451 163–7

[9] Boukai A I, Bunimovich Y, Tahir-Kheli J, Yu J, Goddard III W A and Heath J R 2008 Silicon nanowires as efficient thermoelectric materials Nature 451 168–71

[10] Neophytou N, Wagner M, Kosina H and Selberherr S 2010 Analysis of Thermoelectric Properties of Scaled Silicon Nanowires Using an Atomistic Tight-Binding Model J. Electron. Mater. 39 1902–8

[11] Galli G and Donadio D 2010 Thermoelectric materials: Silicon stops heat in its tracks Nat. Nanotechnol. 5 701–2

[12] Tang J, Wang H-T, Lee D H, Fardy M, Huo Z, Russell T P and Yang P 2010 Holey Silicon as an Efficient Thermoelectric Material Nano Lett. 10 4279–83

[13] Bux S K, Blair R G, Gogna P K, Lee H, Chen G, Dresselhaus M S, Kaner R B and Fleurial J-P 2009 Nanostructured Bulk Silicon as an Effective Thermoelectric Material Adv. Funct. Mater. 19 2445–52

[14] Zhu G H, Lee H, Lan Y C, Wang X W, Joshi G, Wang D Z, Yang J, Vashaee D, Guilbert H, Pillitteri A, Dresselhaus M S, Chen G and Ren Z F 2009 Increased Phonon Scattering by Nanograins and Point Defects in Nanostructured Silicon with a Low Concentration of Germanium Phys. Rev. Lett. 102 196803

[15] Ohishi Y, Miyazaki Y, Muta H, Kurosaki K, Yamanaka S, Uchida N and Tada T 2015 Carrier Transport Properties of p-Type Silicon–Metal Silicide Nanocrystal Composite Films J. Electron. Mater. 44 2074–9

[16] Ohishi Y, Kurosaki K, Suzuki T, Muta H, Yamanaka S, Uchida N, Tada T and Kanayama T 2013 Synthesis of silicon and molybdenum-silicide nanocrystal composite films having low thermal conductivity Thin Solid Films 534 238–41

[17] Gokhale A B and Abbaschian G J 1987 The Cr−Si (Chromium-Silicon) system J. Phase Equilibria 8 474–84

[18] Nishida I and Sakata T 1978 Semiconducting properties of pure and Mn-doped chromium disilicides J. Phys. Chem. Solids 39 499–505

[19] Dasgupta T, Etourneau J, Chevalier B, Matar S F and Umarji A M 2008 Structural, thermal, and electrical properties of CrSi2 J. Appl. Phys. 103 113516

[20] Nishida I 1972 The crystal growth and thermoelectric properties of chromium disilicide J. Mater. Sci. 7 1119–24

[21] Jing X, Li Y and Xu Y 2013 Large anisotropy of electrical conductivity induced high thermoelectric performance of p -type CrSi 2 J. Alloys Compd. 581 413–7

[22] Ma J, Gu Y, Shi L, Chen L, Yang Z and Qian Y 2004 Synthesis and thermal stability of nanocrystalline chromium disilicide J. Alloys Compd. 376 176–9

[23] Schumann J, Gladun C, Mönch J-I, Heinrich A, Thomas J and Pitschke W 1994 Nanodispersed CrxSi1−x thin films: transport properties and thermoelectric application Thin Solid Films 246 24–9

[24] Burkov A T, Vinzelberg H, Schumann J, Nakama T and Yagasaki K 2004 Strongly nonlinear electronic transport in Cr-Si composite films J. Appl. Phys. 95 7903–7

[25] Tiller W A 1958 Liquid Metals and Solidification (Cleveland: ASM)

[26] Anantharaman T R and Suryanarayana C 1987 Rapidly solidified metals: a technological overview (Aedermannsdorf, Switzerland: Trans Tech Publications)

[27] Takahashi F, Mori T, Hamada Y and Hatta I 2001 AC Calorimetric Thermal Diffusivity Measurement in Relatively Thick Samples by a Distance-Variation Method Jpn. J. Appl. Phys. 40 4741–4

[28] Franck E U 1990 J. D. Cox, D. D. Wagman, V. A. Medvedev: CODATA - Key Values for Thermodynamics, aus der Reihe: CODATA, Series on Thermodynamic Properties. Hemisphere Publishing Corporation, New York, Washington, Philadelphia, London 1989. 271 Seiten, Preis: £ 28.00 Berichte der Bunsengesellschaft für Phys. Chemie 94 93–93

[29] Chad V M, Faria M I S T, Coelho G C, Nunes C A and Suzuki P A 2008 Microstructural characterization of as-cast Cr–Si alloys Mater. Charact. 59 74–8

[30] Du Y and Schuster J C 2000 Experimental reinvestigation of the CrSi-Si partial system and update of the thermodynamic description of the entire Cr-Si system J. Phase Equilibria 21 281–6

[31] Chang Y A 1968 Phase relations in the system chromium-silicon Trans. Metall. Soc. AIME 242 1509–15

[32] 2008 JCPDS Card Nos. 01-076-8541 (CrSi2)

[33] 1953 JCPDS Card Nos. 00-005-0565 (Si)

[34] Bathula S, Jayasimhadri M and Dhar A 2015 Mechanical properties and microstructure of spark plasma sintered nanostructured p-type SiGe thermoelectric alloys Mater. Des. 87 414–20

CHAPTER IV

Thermoelectric Properties of *n*-Type Si/$CrMnSi_2$ Eutectic Alloy Fabricated by Melt-Spinning and Spark Plasma Sintering Technique

4.1 Introduction

Previously, we have synthesized nanometer-sized Si-chromium disilicide ($CrSi_2$) composite using melt-spinning (MS) method only [1]. The composition was set to the eutectic one. Using both the natural phase separation at eutectic composition and liquid quenching by MS, very fine structure was obtained. Although the *p*-type Si/$CrSi_2$ nano-eutectic TE materials has been successfully fabricated, it is necessary to densify and combine *p*-type and *n*-type with similar material systems for good TE modules [2]. To maximize the conversion efficiency, the TE compatibility factor value, $s = |(1+ZT)^{0.5}-1|/(ST)$, of the *p*-type and *n*-type materials should be similar within the operating temperature range. The compatibility factor should not change by more than a factor of two [3,4]. In the Si-$CrSi_2$ composite, Si can be easily converted to *n*-type by doping with phosphorous (P). On the other hand, pure $CrSi_2$ is a *p*-type degenerated semiconductor [5], difficult to convert the conduction type. It is reported that when manganese (Mn) atoms are introduced in the $CrSi_2$ crystal, Mn becomes a donor and decreases the hole concentration [6]. In fact, *n*-type conduction has been reported by substitution of Cr atom with Mn composition of 12 at%, 14 at% and 18 at% [7].

In this study, firstly we prepared $Cr_{1-x}Mn_xSi_2$ samples of three different compositions to determine appropriate Cr/Mn ratio for *n*-type materials. Next, we prepared composites of P-doped $(Cr_{0.8}Mn_{0.2})_ySi_{100-y}$ with different compositions in order to determine the correct eutectic composition. The reported eutectic composition for Si-Cr system differs in the rage of 12–18 Cr % [8–10]. Finally, we fabricated the nano-eutectic *n*-type Si-$Cr_{0.8}Mn_{0.2}Si_2$ TE materials using MS technique. The melt-spun sample was consequently sintered by spark plasma sintering (SPS). The TE properties of the composites bulk samples were measured, and effects of the fabrication processes on the TE properties were examined.

4.2 Experimental Procedures

As starting materials, high-purity semiconductor-grade Si, P (6N), Cr (3N), and Mn (3N) were used to prepare a master ingot with a nominal composition of $Cr_{1-x}Mn_xSi_2$ (x = 0.15, 0.20, 0.25) and $(Cr_{0.8}Mn_{0.2})_y(Si_{0.99}P_{0.01})_{100-y}$ (y = 15.5, 16.0, 16.5) by arc melting (AM) under an argon (Ar) atmosphere. The obtained arc-melted ingot was melted in a hexagonal boron nitride (h-BN) tube with a 0.6 mm diameter nozzle by induction heating. The MS technique was used with the melted ingot ejected under an Ar atmosphere of 10 kPa onto a copper roller that was operated at a wheel linear speed of 2000 RPM and 4000 RPM. The obtained ribbon samples are represented as MS2000 and MS4000, where the number indicates the rotation speed of the roller. Subsequently, MS4000 ribbons were pulverized in a tungsten carbide mortar and the obtained powder was placed into a graphite die for SPS. The sintering was conducted in Ar flow at 1173 K for 3 min under axial pressure of 100 MPa. The bulk sample is denoted as MS4000-SPS. A sample with same composition and same SPS conditions was prepared by AM and SPS to compare the morphology, represented as AM-SPS.

The samples were characterized by powder X-ray diffraction (XRD) analysis using an X-ray diffractometer (Ultima IV, Rigaku Co.) with Cu Kα radiation. The lattice parameters of $Cr_{1-x}Mn_xSi_2$ phase were calculated from the observed XRD peak positions based on Cohen's method [11]. The microstructure of the sample was observed using a field-emission scanning electron microscope (FE-SEM, JEOL JSM-6500F) and energy dispersive X-ray spectrometry (EDX). The thermoelectric properties along the longitudinal direction of the ribbons, i.e., perpendicular to the direction of the eutectic growth, were measured. The electrical resistivity (ρ) and Seebeck coefficient (S) of the samples were determined simultaneously in a He atmosphere at temperatures ranging from room temperature to 773 K by a four-point technique and a static direct-current method using a ZEM-3 instrument system (ULVAC-RIKO, Inc.).

For the determination of ρ, a cross-section of the ribbon sample was estimated using the mass, the density, and the length of the sample. The sample setting is previously reported in details [12].The thermal diffusivity, α, for the MS4000 ribbon samples was collected with an AC calorimetric method using a LaserPIT (ULVAC-RIKO, Inc.) at room temperature. 7 ribbon samples were examined. For AM-SPS and MS4000-SPS bulk samples, the thermal diffusivity was measured by laser flash method (Netzsch LFA-457) from room temperature to 773 K. The specific heat capacity, C_P, for $Cr_{0.8}Mn_{0.2}Si_2$ sample was measured by differential

scanning calorimetry (DSC, Netzsch STA449C Jupiter). C_P for Si-$Cr_{0.8}Mn_{0.2}Si_2$ composite samples was calculated using the measured C_P of $Cr_{0.8}Mn_{0.2}Si_2$ and reported C_P of Si [13]. The thermal conductivity, κ, was determined using a formula of $\kappa = \alpha C_P d$, where d is a sample density. The temperature dependence of the sample density and effect of small amount of P element on C_P were not considered.

4.3 Results and discussion

4.3.1 Conversion of $CrSi_2$ to *n*-type by Mn substitution

We have fabricated $Cr_{1-x}Mn_xSi_2$ ingots by arc melting. Fig. 4.1 shows the XRD patterns for $Cr_{1-x}Mn_xSi_2$ (x = 0.15, 0.20, 0.25) samples. The XRD peaks of hexagonal $CrSi_2$-phase were observed mainly in all the samples, while the peak of $MnSi_{1.74}$ was detected in sample with x = 0.25. A single-phase $CrSi_2$-$MnSi_2$ solid solution was obtained in x = 0.15 and 0.20. In the sample of x = 0.25, the Mn did not completely dissolve in $CrSi_2$ phase and generate $MnSi_{1.74}$. Other impurity phase such as pure Si phase is not detected by the XRD analysis.

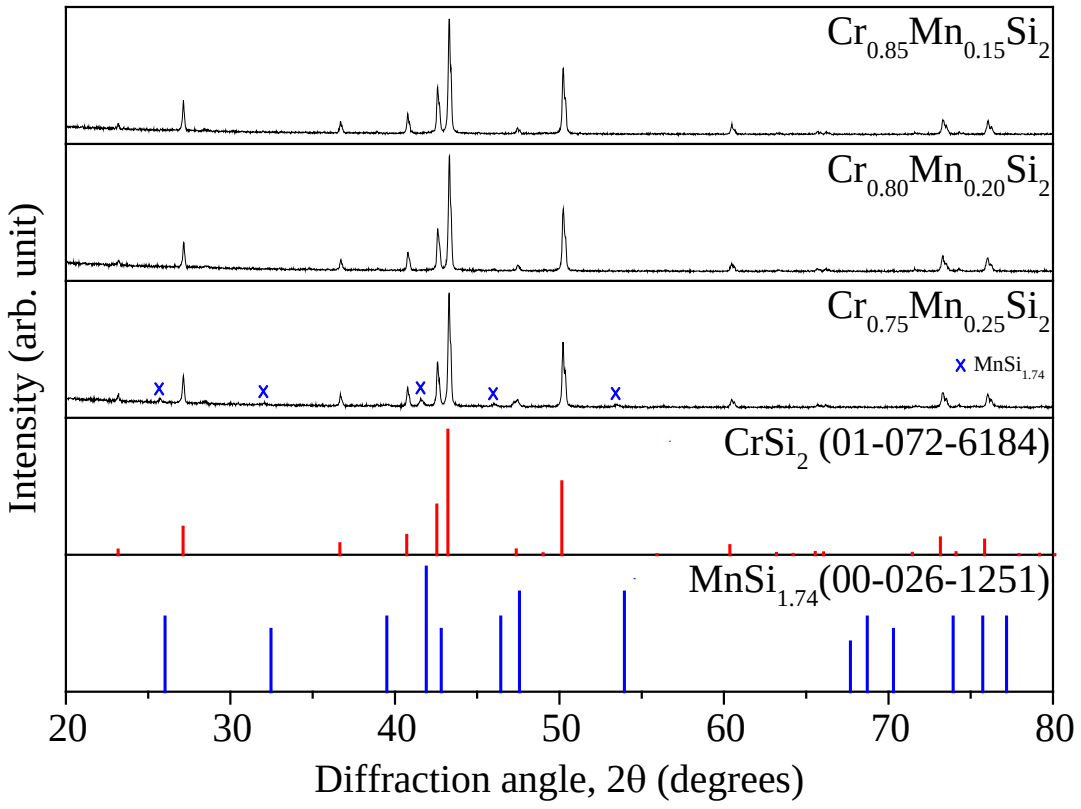

Figure 4.1 Powder XRD pattern of $Cr_{1-x}Mn_xSi_2$ (x = 0.15, 0.20, 0.25) samples

Fig. 4.2 shows the lattice parameter of $CrSi_2$ phase in the three samples, calculated from the observed XRD peaks in Fig. 4.1. The reported lattice parameter of $CrSi_2$ is 4.428 Å [7,14], agrees well with the present result. As shown in the figure, the lattice parameter proportionally decreases with Mn content up to $x = 0.20$, indicating Mn is completely solved in $CrSi_2$ phase. The solid solubility limit of Mn has been studied by Nishida et al. [7], reported to $x = 0.225$ for $Cr_{1-x}Mn_xSi_2$. From the results of XRD analysis and lattice parameter in the present study, the solid solubility limit of Mn is considered to lie between $x = 0.20$ and $x = 0.25$, which is corresponding to the previous result.

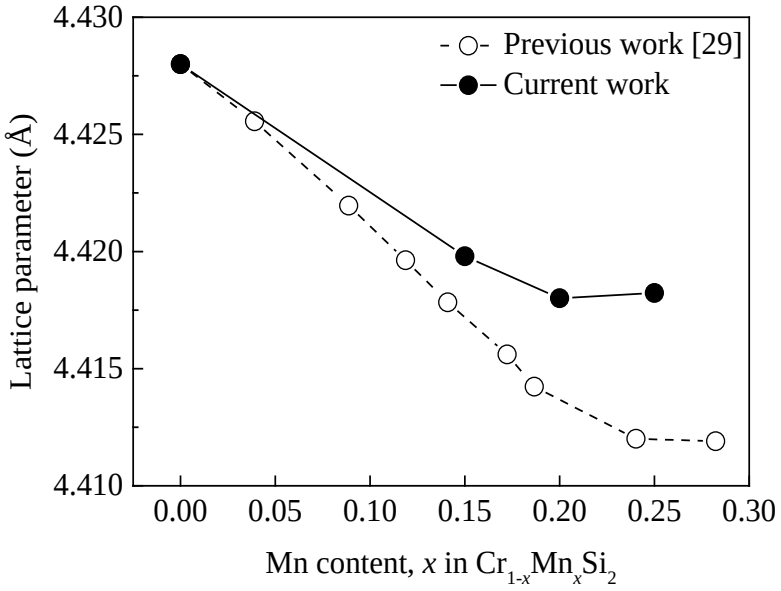

Figure 4.2 Relationship between proportion of Mn and lattice parameter

The temperature dependence of Seebeck coefficient and electrical resistivity for $Cr_{1-x}Mn_xSi_2$ ($x = 0.15, 0.20, 0.25$) samples are shown in Fig. 4.3. For all the samples, the Seebeck coefficient is negative from room temperature to approximately 500 K, showing *n*-type conduction under the temperature. However, the sign changes to positive as the temperature rises. Pure $CrSi_2$ is known to be a degenerated *p*-type semiconductor [15]. Theoretically, the Seebeck coefficient, under mixed contribution of electrons and holes is defined as [16,17]:

$$S = \frac{S_h\sigma_h - S_e\sigma_e}{\sigma_h + \sigma_e} \tag{4.1}$$

where $\sigma_{e,h}$ the conductivity and $S_{e,h}$ the Seebeck coefficient (with the subscripts *e* and *h* referring to electrons and holes, respectively). At room temperature, electrons are the majority carriers and holes are the minority carriers inside the sample. As the temperature increase, thermal carrier excitation occurs and hole conduction become dominant in the sample due to the higher carrier mobility of holes than electrons [7]. When Mn content increased, the *n*-to-*p* transition temperature is slightly shifted to higher side. The temperature dependence qualitatively agrees with the previous result [7]. However, the different results obtained for the Seebeck coefficient and electrical resistivity as reported [7] may be due to the difference in sample's synthesize technique which lead to some of the Mn-atoms vaporizing during the process of the arc-melting, hot-pressing and annealing. This may reduce the electron carrier concentration, which cause the *n*-to-*p* transition temperature shifted to lower side and correspond to the electrical resistivity and Seebeck coefficients behavior.

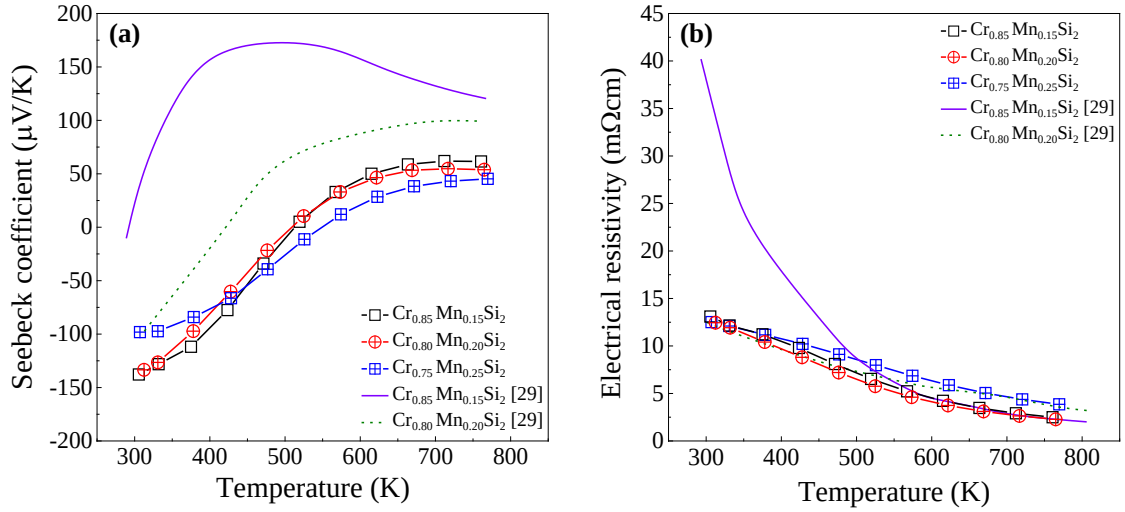

Figure 4.3 Temperature dependence of (a) Seebeck coefficient and (b) electrical resistivity for Cr_{1-x}-Mn_xSi_2 (x = 0.15, 0.20, 0.25) samples

Looking at each composition, the absolute value of the Seebeck coefficient shows a lower value for samples with x = 0.25 compared to x = 0.15, 0.20. This is thought to be due to the $MnSi_{1.74}$ impurity phase which is known as p-type semiconductor. Existence of the impurity phase is supported from the XRD analysis. In this experiment the difference in Seebeck coefficient between x = 0.15 and 0.20 samples was hardly to see, differs within the measurement error range of 7 % for a ZEM-3 equipment. As for electrical resistivity, there is not so large difference among these three samples. The electrical resistivity has apparently risen by Mn addition from 0.6 mΩcm for non-doped $CrSi_2$ at room temperature [7]. This is caused

by reduction of the hole carrier concentration and lower electron carrier mobility. The electrical resistivity of all samples decline as temperature increase, which is the typical semiconductor behavior with nondegenerate characteristics. From these results, we determine to use the composition of $Cr_{0.80}Mn_{0.20}Si_2$ as *n*-type silicide phase for Si-silicide eutectic sample described later.

4.3.2 Determination of eutectic composition and microstructure

In order to determine a correct eutectic composition, we prepared P-doped $(Cr_{0.8}Mn_{0.2})_ySi_{100-y}$ samples of three different compositions with y = 15.5, 16.0, and 16.5. Fig. 4.4 shows the XRD patterns. The strong diffraction peaks corresponding to $CrSi_2$ and Si phases are observed, indicating that the arc-melted samples mainly compose of the two phases. Meanwhile, weak peaks of $MnSi_{1.74}$ phase are also observed for all the samples in spite that the Mn content is less than the solubility limit as mentioned. Coexistence with the Si-phase may affect the stability of $MnSi_{1.74}$ phase, but the details are unclear.

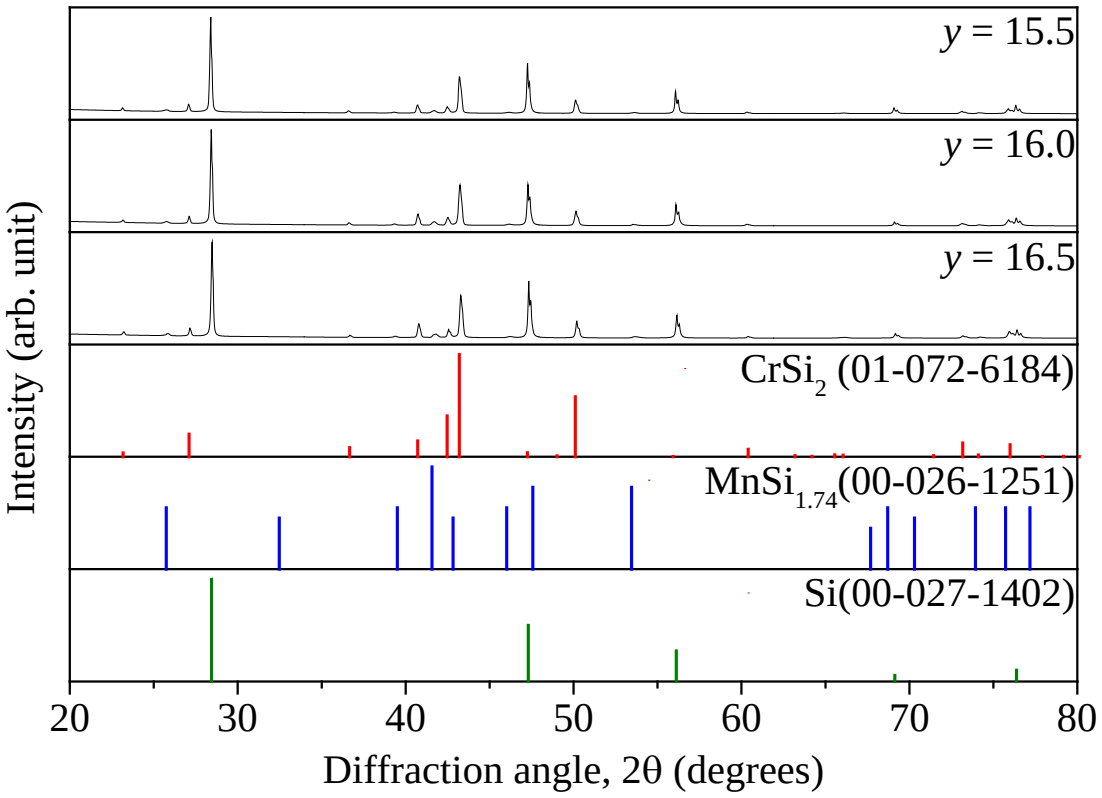

Figure 4.4 Powder XRD pattern of P-doped $(Cr_{0.8}Mn_{0.2})_ySi_{100-y}$ (y = 15.5, 16.0, 16.5) arc-melted samples

To identify the atomic distribution in the sample, EDX analysis was carried out and the images are shown in Fig. 4.5. The Si and (Cr,Mn)Si_2 phases are clearly separated. There is no deviation of Cr and Mn distribution in the silicide phase. Homogeneous silicide phase is obtained. SEM images in Fig. 4.6 show the microstructure of P-doped $(Cr_{0.8}Mn_{0.2})_ySi_{100-y}$ (y = 15.5, 16.0, 16.5) melt-spun samples. They have a fine lamellar structure. The white areas in the SEM images correspond to $CrSi_2$ phase and the grey areas to Si phase as shown in Fig. 4.5 (a). The lamellar structure is mainly observed for all the samples, however, relatively large grains of the Si phase are seen at y = 15.5 sample, similarly large petal-shape $CrSi_2$ phase grains are seen at y = 16.5 sample. At y = 16.0 sample there is no large grain, well-organized lamellar structure forms in almost all area. Thus, the eutectic composition for this system is determined to y = 16.0 in $(Cr_{0.8}Mn_{0.2})_ySi_{100-y}$.

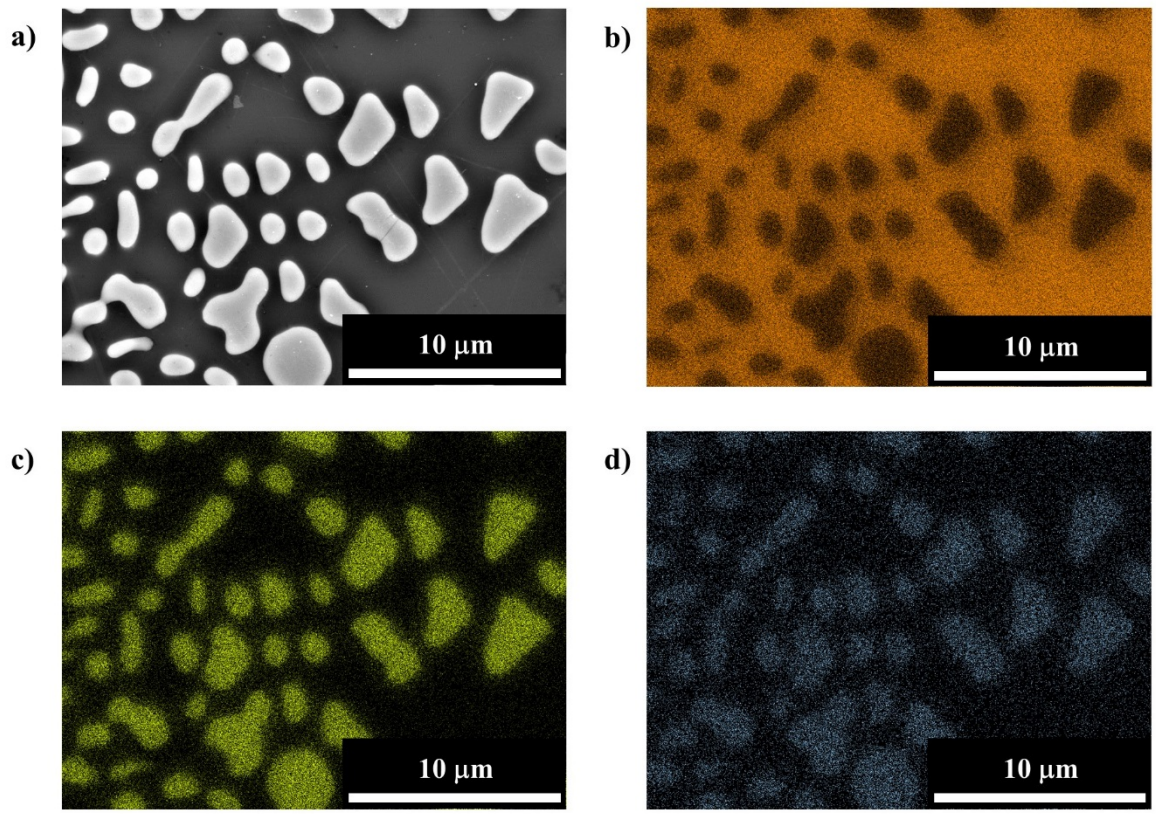

Figure 4.5 Surface image of arc-melted sample: (a) SEM image and EDX mapping images of (b) Si, (c) Cr, and (d) Mn, respectively. The white scale bars represent 10 μm

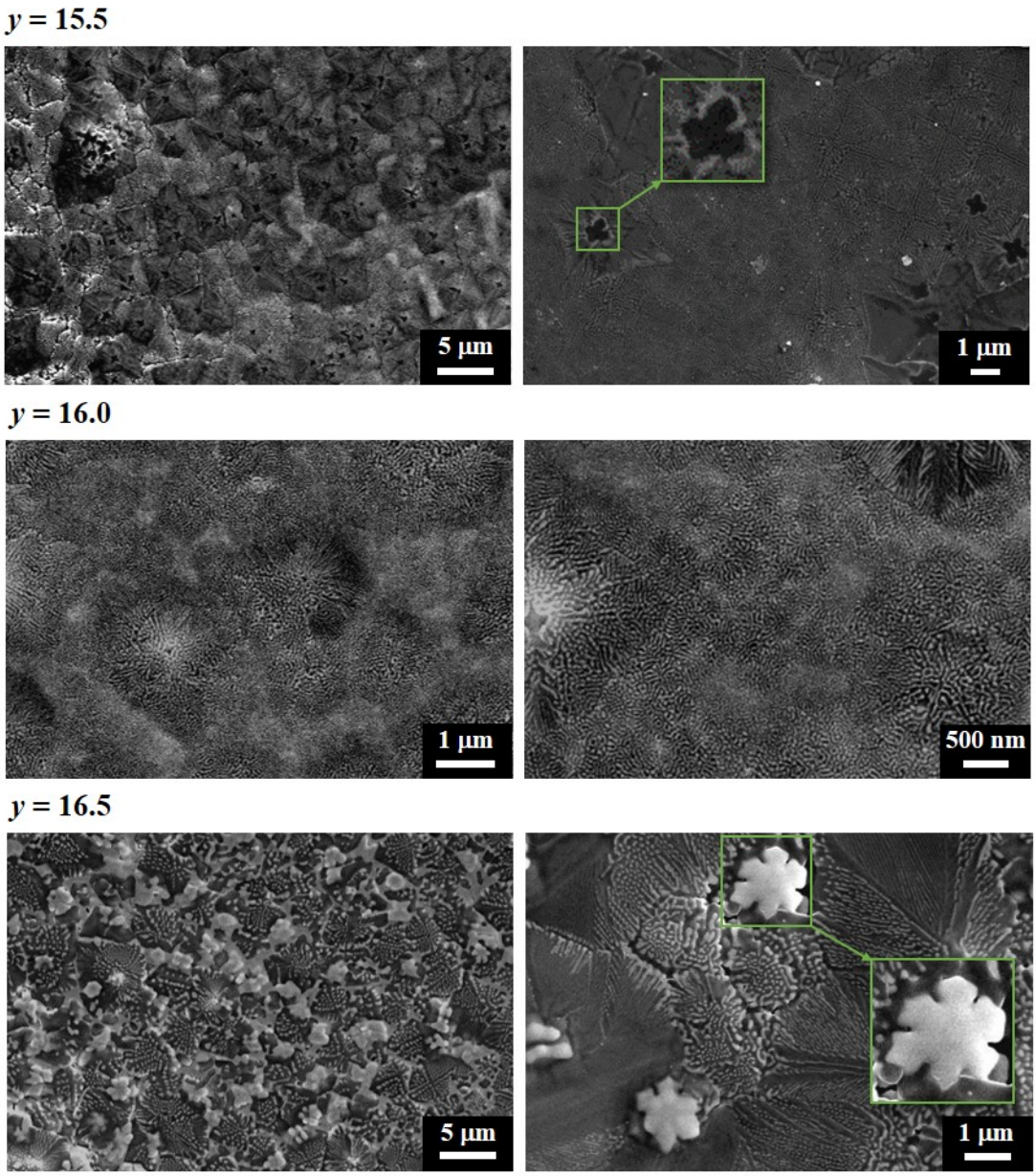

Figure 4.6 Scanning electron micrograph of the P-doped $(Cr_{0.8}Mn_{0.2})_ySi_{100-y}$ (y = 15.5, 16.0, 16.5) melt-spun samples

4.3.3 Fabrication and characterization of *n*-type P-doped Si/$Cr_{0.80}Mn_{0.20}Si_2$

According to the previous results, we fabricated $(Cr_{0.8}Mn_{0.2})_{16}(Si_{0.99}P_{0.01})_{84}$ eutectic samples. High density bulk samples were prepared by SPS using the powders synthesized by arc-melting and melt-spinning techniques. The relative density is 95% of theoretical density for AM-SPS and 97% for MS-SPS. Fig. 4.7 shows XRD patterns for the ribbon and SPS samples. The peaks of $MnSi_{1.74}$ phase were observed in all of the samples in addition to the

peaks of Si and $CrSi_2$ phases. For the MS4000 and MS4000-SPS samples, the $MnSi_{1.74}$ peaks were scarcely observed, which indicates that the high cooling rate suppressed nucleation of the $MnSi_{1.74}$ phase. In any case, the $MnSi_{1.74}$ peaks are very weak, hence the effects on the TE properties can be neglected. It is notable that the peak width of the XRD pattern is obviously broadened in the MS2000 and MS4000 samples as compared with the AM-SPS sample. It indicates that melt-spinning technique forms the very fine microstructure. SPS for MS4000 ribbon sharpen the XRD peaks, indicating grain growth occurred in the sample.

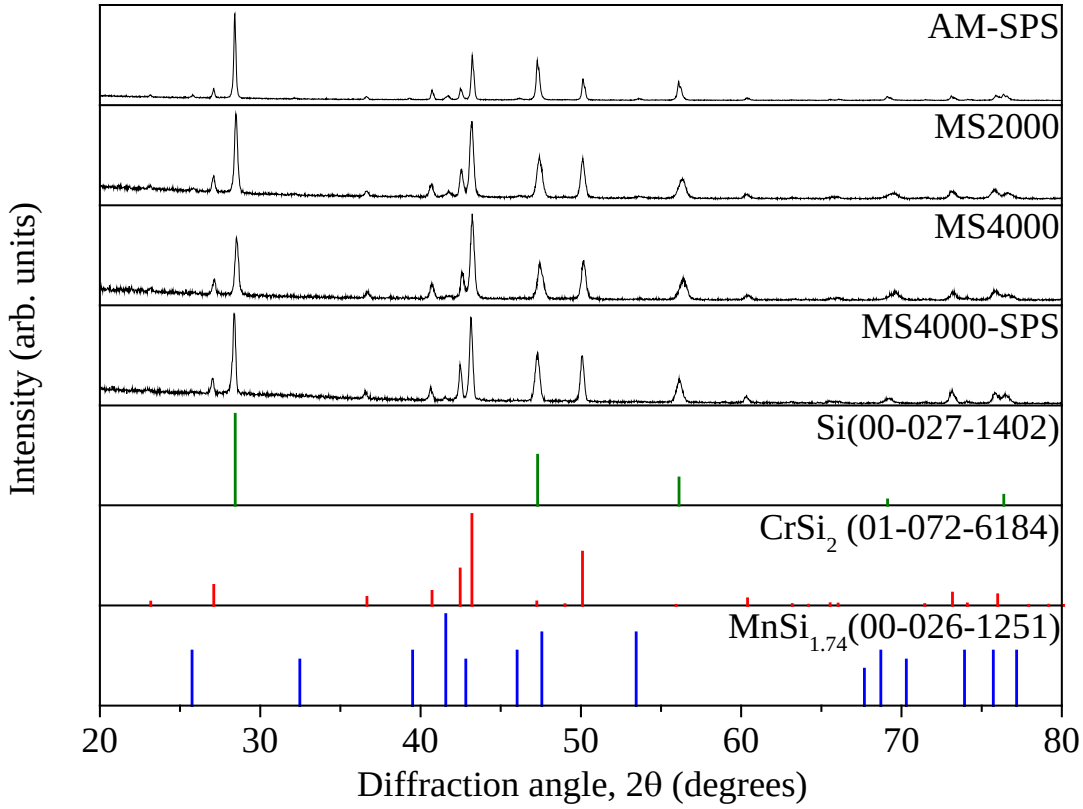

Figure 4.7 Powder XRD pattern of P-doped $(Cr_{0.8}Mn_{0.2})_{16}Si_{84}$ samples

In the SEM images of Figure 4.8, it is found that the MS2000, MS4000, and the MS4000-SPS samples, which were subjected to melt-spinning, have finer microstructure than of the comparative AM-SPS sample. Quantitatively looking at the eutectic intervals, AM-SPS is 1~2 μm while MS2000, MS4000 and MS4000-SPS are 70~130 nm, 20~40 nm, 100~200 nm respectively from their images. MS4000 sample has a finer structure than MS2000 sample because of the faster cooling rate. Marked grain growth was observed in MS4000-SPS, it is corresponding to the change in XRD peak width. Although grain growth occurred during the sintering, the microstructure of MS4000-SPS sample was successfully refined by about 1/10

than AM-SPS sample. The volume fraction of each phase for SPS sample was estimated by SEM image analysis. The estimated volume fraction of Si phase is 64%, which agrees with the calculated fraction from the molar ratio and density of each phase (Si: 2.33 g/cm^3, $Cr_{0.8}Mn_{0.2}Si_2$: 5.00 g/cm^3).

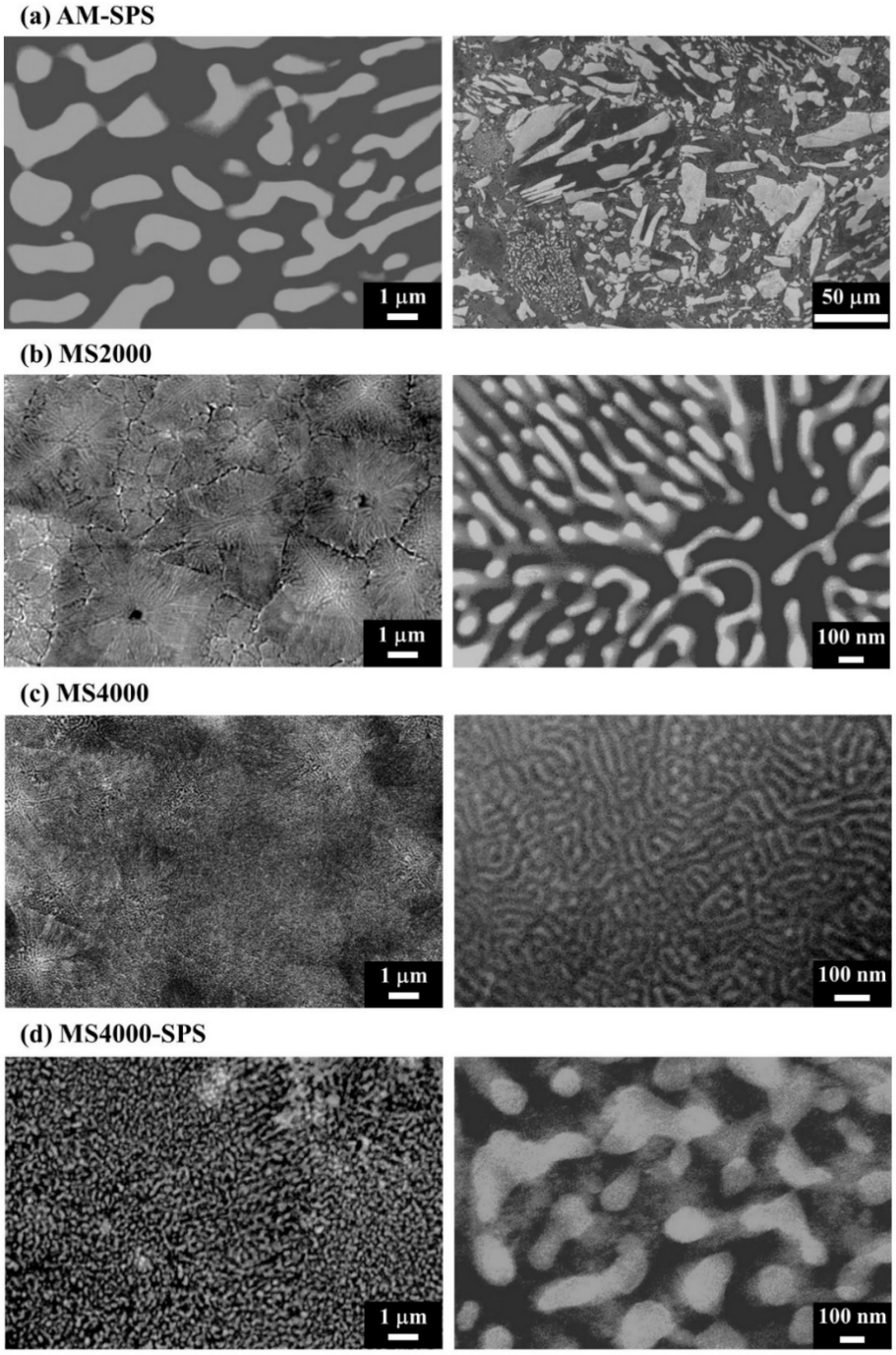

Figure 4.8 Scanning electron micrograph of the P-doped $(Cr_{0.8}Mn_{0.2})_{16}Si_{84}$ samples (a) AM-SPS, (b) MS2000, (c) MS4000, and (d) MS4000-SPS

Figure 4.9 shows the temperature dependence of Seebeck coefficient, electrical resistivity, and power factor for AM-SPS, MS4000 and MS4000-SPS samples. The sign of the Seebeck coefficient was negative for all the samples and in the measured temperature range. The *n*-type nano-eutectic composite samples could be obtained as intended. The absolute Seebeck value of MS4000-SPS is about 110~140 μV/K, the highest among the three samples. By comparing MS4000 with MS4000-SPS samples, MS4000 sample has lower Seebeck value and higher electrical resistivity. It may be explained by difference in density of interface between Si and silicide phases. The interfacial states provide electronic carriers, and the interfacial barrier potentials scatters the carriers. Because the MS samples have very high interface density, the carrier concentration and scattering rate are high, consequently they show lower Seebeck coefficient value and higher electrical resistivity. MS4000 sample shows the lowest power factor, the result indicates that the excessive-high interface density is not preferable for thermoelectric performance.

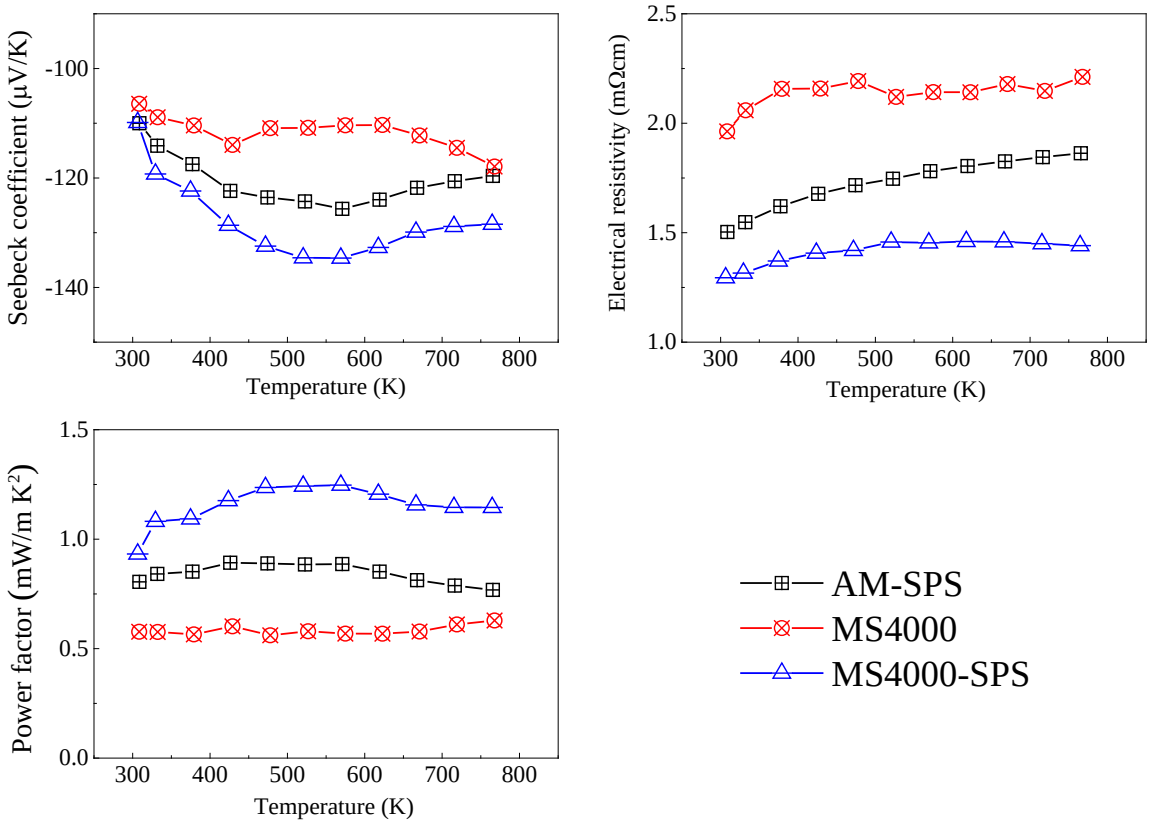

Figure 4.9 Temperature dependence of (a) Seebeck coefficient, (b) electrical resistivity, (c) power factor for P-doped $(Cr_{0.8}Mn_{0.2})_{16}Si_{84}$ samples

Regarding the temperature dependence, the absolute Seebeck coefficient decreases around 500 K. It is not seen for doped Si phase, hence that temperature dependence is caused by thermal carrier excitation in the $(Cr,Mn)Si_2$ phase as seen in Figure 4.3. The temperature dependence of MS4000 sample is complex, begin to decrease around 400 K and then increase around 650 K. The behaviour is difficult to explain. Carrier excitation from the interfacial states may affect the temperature dependence. Room temperature values of the Hall carrier concentration (nH) and Hall mobility (μH) of the bulk samples are shown in Table 4.1. The nH of the AM-SPS is lower than MS4000-SPS samples. This might be due to energy states generated at boundaries. As described, the MS4000-SPS sample had the smallest precipitates among the samples; thus, the MS4000-SPS sample exhibited the lowest μH values.

Table 4.1. Hall carrier concentration nH (300 K) and Hall mobility μH (300 K) of the AM-SPS and MS4000-SPS samples

Sample	Hall carrier concentration nH (10^{20} cm^{-3})	Hall mobility μH (cm^2 V^{-1} s^{-1})
AM-SPS	1.36 ± 0.02	30.6 ± 0.3
MS4000-SPS	3.08 ± 0.07	20.5 ± 0.5

By comparing AM-SPS with MS4000-SPS of the bulk samples, AM-SPS have slightly lower Seebeck value. This is considered due to evaporation of a tiny amount of dopant element of P at the MS process. Observing at the temperature dependence of Seebeck coefficient, both samples show almost same behaviour. The SPS process for MS sample reduced density of the interface and the interfacial states accompanied with the grain growth, which change the carrier concentration and scattering rate. In spite of the similar Seebeck coefficient value, the electrical resistivity of AM-SPS sample is lower than that for MS-SPS. It is caused by the difference in the sample density, 95% for AM-SPS and 97% for MS-SPS sample. With the results of Seebeck coefficient and electrical resistivity, it can be said that the microstructure of MS-SPS sample does not affect the electrical properties. Among the samples, MS4000-SPS sample shows the highest power factor of 1.2 mW/mK^2 around 500 K. The value is higher than those for the n-type $CrSi_2$ and $(Cr,Mn)Si_2$. The power factor is enhanced by combining the silicide with P-doped Si phase.

The thermal conductivity of MS4000 at room temperature and the temperature

dependence of the two bulk samples are shown in Figure 4.10. C_P for $Cr_{0.8}Mn_{0.2}Si_2$ measured by DSC is shown together. The fitted curve for C_P is expressed by following equation;

$$C_P = 0.5321 + 8.027 \times 10^{-4}T - 7.992 \times 10^{-7}T^2 + 36.02T^{-2} \text{ (J/gK)}. \quad (2)$$

The value is used to calculate C_P of the composite samples. Thermal conductivity of the ribbon samples MS4000 has relatively large variance, caused by non-uniformity of the sample thickness and structure size. The average value for MS4000 is about 17 W/mK. This show that the thermal conductivity can be reduced by about 30% compared with AM-SPS sample. Grain growth occurs MS4000-SPS sample, but the lattice thermal conductivity is reduced by about 24% compared to AM-SPS. It can be said that the lattice thermal conductivity was successfully reduced by the eutectic structure, prepared by liquid quenching.

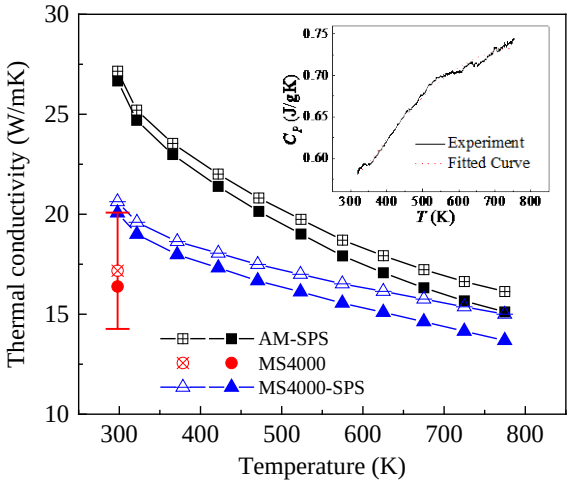

Figure 4.10 Temperature dependence of specific heat capacity for $Cr_{0.8}Mn_{0.2}Si_2$ sample and thermal conductivity for P-doped $(Cr_{0.8}Mn_{0.2})_{16}Si_{84}$ samples. The error bar for MS4000 shows standard deviation from 7 ribbon samples. The open symbols show total thermal conductivity and filled symbols lattice thermal conductivity

The temperature dependence of *ZT* in each sample is shown in Figure 4.11. MS4000-SPS sample shows the highest *ZT* among other samples in whole temperature range. The *ZT* increases with temperature, the maximum value of 0.054 is obtained at 773 K. The value is not high, however, compared with AM-SPS, we succeeded in improving by about 50% in all temperature range. By using liquid quenching at the eutectic composition, we succeeded in improving the *ZT* by reducing thermal conductivity and maintaining the electrical properties.

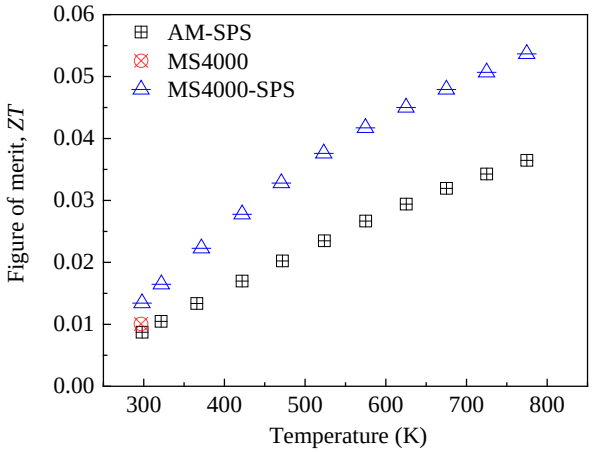

Figure 4.11 Temperature dependence of *ZT* for P-doped $(Cr_{0.8}Mn_{0.2})_{16}(Si_2)_{84}$ sample

4.4 Conclusion

Using the melt-spinning method at the eutectic composition, we successfully fabricated a ribbon-like lamellar structure *n*-type Si-(Cr,Mn)Si_2 composites with a spacing range of 20–40 nm. The appropriate Cr/Mn ratio and the correct eutectic composition were determined. Although the size of the morphology change to about 100 nm to 200 nm during sintering process, a fine nanostructure was obtained in the bulk sample (MS4000-SPS). It is demonstrated that κ were reduced by 20-30% by the structure refinement. The power factor was reduced in as-cast melt-spun ribbon sample, but it recovered by following sintering process. As a result, *ZT* value was improved about 50% compared to arc-melted sample. The rapid quenching at the eutectic composition is thought to be a promising method to synthesize fine-microstructure and improve the thermoelectric performance.

4.5 Reference

[1] Ohta M, Biswas K, Lo S-H, He J, Chung D Y, Dravid V P and Kanatzidis M G 2012 Enhancement of Thermoelectric Figure of Merit by the Insertion of MgTe Nanostructures in p-type PbTe Doped with Na2Te *Adv. Energy Mater.* **2** 1117–23

[2] Karvonen L, Tomeš P and Weidenkaff A 2011 Thermoelectric Performance of Perovskite-type Oxide Materials *Mater. Matters* **6** 92–9

[3] Snyder G J 2004 Application of the compatibility factor to the design of segmented and cascaded thermoelectric generators *Appl. Phys. Lett.* **84** 2436–8

[4] Molinari M, Tompsett D A, Parker S C, Azough F and Freer R 2014 Structural, electronic and thermoelectric behaviour of CaMnO 3 and CaMnO (3−δ) *J. Mater. Chem. A* **2** 14109–17

[5] Nishida I 1972 The crystal growth and thermoelectric properties of chromium disilicide *J. Mater. Sci.* **7** 1119–24

[6] Shinoda D, Asanabe S and Sasaki Y 1964 Semiconducting Properties of Chromium Disilicide *J. Phys. Soc. Japan* **19** 269–72

[7] Nishida I and Sakata T 1978 Semiconducting properties of pure and Mn-doped chromium disilicides *J. Phys. Chem. Solids* **39** 499–505

[8] Chad V M, Faria M I S T, Coelho G C, Nunes C A and Suzuki P A 2008 Microstructural characterization of as-cast Cr–Si alloys *Mater. Charact.* **59** 74–8

[9] Du Y and Schuster J C 2000 Experimental reinvestigation of the CrSi-Si partial system and update of the thermodynamic description of the entire Cr-Si system *J. Phase Equilibria* **21** 281–6

[10] Chang Y A 1968 Phase relations in the system chromium-silicon *Trans. Metall. Soc. AIME* **242** 1509–15

[11] Cohen M U 1935 Precision Lattice Constants from X-Ray Powder Photographs *Rev. Sci. Instrum.* **6** 68–74

[12] Norizan M N, Miyazaki Y, Ohishi Y, Muta H, Kurosaki K and Yamanaka S 2018 The

Nanometer-Sized Eutectic Structure of Si/CrSi2 Thermoelectric Materials Fabricated by Rapid Solidification *J. Electron. Mater.* **47** 2330–6

[13] Franck E U 1990 J. D. Cox, D. D. Wagman, V. A. Medvedev: CODATA - Key Values for Thermodynamics, aus der Reihe: CODATA, Series on Thermodynamic Properties. Hemisphere Publishing Corporation, New York, Washington, Philadelphia, London 1989. 271 Seiten, Preis: £ 28.00 *Berichte der Bunsengesellschaft für Phys. Chemie* **94** 93–93

[14] Parker D and Singh D J 2012 Very heavily electron-doped CrSi 2 as a high-performance high-temperature thermoelectric material *New J. Phys.* **14** 033045

[15] Dasgupta T, Etourneau J, Chevalier B, Matar S F and Umarji A M 2008 Structural, thermal, and electrical properties of CrSi2 *J. Appl. Phys.* **103** 113516

[16] Johnson V A and Lark-Horovitz K 1953 Theory of Thermoelectric Power in Semiconductors with Applications to Germanium *Phys. Rev.* **92** 226–32

[17] Zhou W, Sun T, Hng H, Zhang W, Zhao Y, Zhang H, Ma J and Yan Q 2012 Sign changes of seebeck coefficients due to extrinsic-to-intrinsic transition for PbTe nanocrystals *World J. Eng.* **9** 391–8

CHAPTER V

Thermoelectric Properties of *n*-Type BiSb/InSb Eutectic Alloy Fabricated by Melt-Spinning and Spark Plasma Sintering Technique

5.1 Introduction

Both bismuth (Bi) and antimony (Sb) are semimetals from group V metals with a similar crystal structure of A_7 structure (rhombohedral) of $R\bar{3}m$ space group [1]. $Bi_{100-x}Sb_x$ alloys form a solid solution over the entire composition range because Bi and Sb have similar chemical properties and lattice parameters [2]. Bi-Sb alloy is a *n*-type material (typically S = -100 μVK^{-1} at 300 K) and semiconducting inside the range $0.07 < x < 0.22$. The best ZT = 0.33 at 300 K along the trigonal direction was reported for single crystal with $0.09 < x < 0.16$ [3–6]. Nonetheless, the single crystals are mechanically weak, having difficulty in cleaving and growing, along with slow growth rate [6,7]. Poly-crystalline materials might be suitable but so far all have been reported to have lower ZT than the single crystals. The performance degradation is mainly caused by heterogeneity in the Bi/Sb composition inside the sample, which easily occurs at the cooling process. Hence several preparation methods of melt-quenching [6], arc melting [8,9], mechanical alloying [14], and rapid solidification with spark plasma sintering [15] process have been developed in order to enhance the homogeneity and ZT performance. Nevertheless, conventional water-quenching can not provide sufficient cooling rate, and oxidation and contamination occur in the material during the mechanical alloying process. These problems can be prevented in the rapid solidification process such as melt-spinning (MS) method.

Recently, we have synthesized nanometer-sized semiconductor eutectic composite using the MS method combined with subsequent spark plasma sintering (SPS) process for Si-$CrSi_2$ semiconductor system [16,17]. Very fine microstructure was obtained using both the natural phase separation at eutectic composition and liquid quenching by MS. The thermal conductivity was reduced and ZT was enhanced by the fabrication method. We focused on the Bi-Sb alloy - indium antimonide (InSb) semimetal system, which has a typical eutectic point

between Bi-Sb and InSb as shown in the phase diagram in Fig. 5.1. The eutectic phase has a lower melting point than its components. InSb is a narrow band gap semiconductor with a band gap of 0.18 eV at room temperature and possesses a high electron mobility [18] and also a high thermal conductivity [14]. In this work, we prepared the eutectic *n*-type $Bi_{0.88}Sb_{0.12}$/InSb TE material using MS technique and consequently sintered by SPS. The TE properties of the composites samples were measured, and the relationship between TE transport properties and microstructure was discussed.

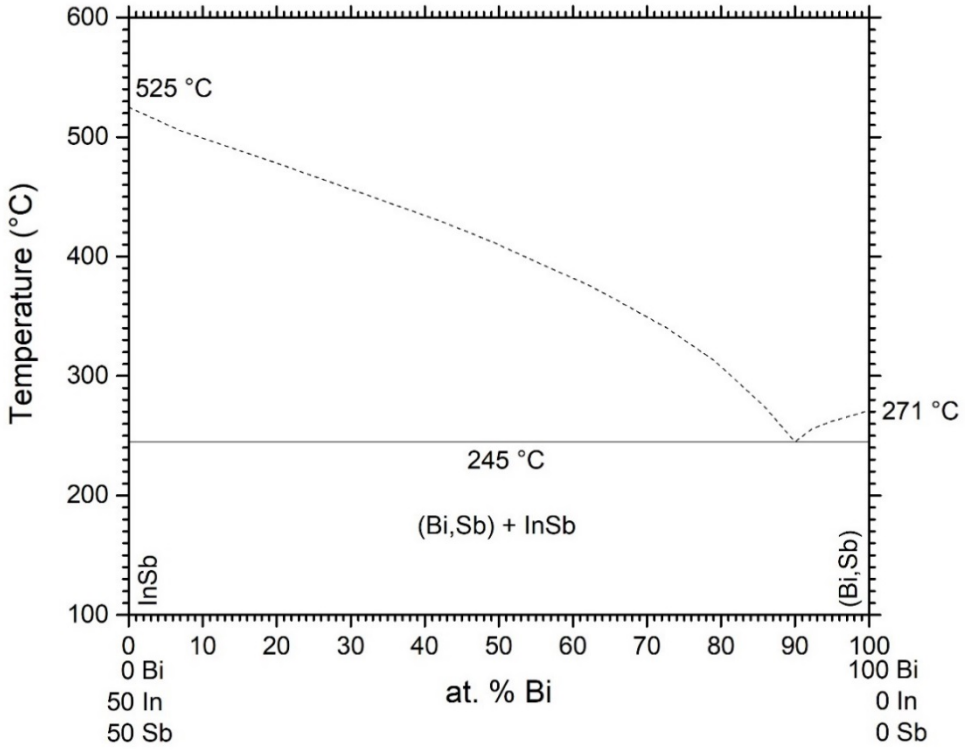

Figure 5.1 Pseudobinary phase diagram of the BiSb–InSb system

5.2 Experimental Procedures

As starting materials, Bi (5N), In (3N) and Sb (3N) were used to prepare a master ingots with a nominal composition of $(Bi_{0.88}Sb_{0.12})_{90}(InSb)_{10}$. The material have been carefully weighted out with the stoichiometric and loaded in the silica tubes. The silica tubes were sealed under vacuum using oxygen/hydrogen torch and transferred in the vertical furnace. The silica tubes have been heated with the melting condition (823K, 5 K/min for 12 hours holding) and then rapidly quenched by putting the heat treated silica tubes into cold water. The obtained

quench-melted (QM) ingot was then melted in a silica tube with a 0.6 mm diameter nozzle by induction heating. The MS technique was used with the melted ingot ejected under an argon (Ar) atmosphere of 0.1 MPa onto a copper roller that was operated at wheel linear speed of 2000 RPM and 4000 RPM. The obtained ribbon samples are represented as MS2000 MS4000, where the number indicates the rotation speed of the roller. Subsequently, the QM, MS2000 and MS4000 ribbon sample was pulverized in a tungsten carbide mortar and the obtained power sample was placed into a graphite die for SPS in Ar flow at 473K for 10 min under axial pressure of 50 MPa. The forming bulk samples are denoted as MS2000-SPS, and MS4000-SPS. A sample with same composition and same SPS conditions was prepared by QM and SPS to compare the morphology, denoted as QM-SPS.

The samples phase identification was characterized by powder X-ray diffraction (XRD) analysis using an X-ray diffractometer (Ultima IV, Rigaku Co.) with Cu Kα radiation at room temperature. The microstructure of all the sample was observed using a field-emission scanning electron microscope (FE-SEM, JEOL JSM-6500F) and energy dispersive X-ray spectrometry (EDX). The TE properties of the bulk sample were measured. The ρ and S of the samples were determined simultaneously in a He atmosphere at temperatures ranging from 300 K to 773 K by a four-point technique and a static direct-current method using a ZEM-3 instrument system (ULVAC-RIKO, Inc.). The κ, was determined using a formula of $\kappa = \alpha\ C_P\ d$, where α is the thermal diffusivity, C_P is the heat capacity, and d is the sample density. The α, was measured by laser flash method (Netzsch LFA-457) from 300 K to 773 K. $C_P = 3nR$, where n is the number of atoms per formula unit and R is the gas constant. d was calculated from the measured weight and dimensions of the samples.

5.3 Results and discussion

Fig. 5.2 shows the powder XRD patterns for the QM, MS and SPS samples. The powder XRD pattern confirms that all the patterns were well consistent with those of Bi and InSb. As shown in the Bi-Sb peaks, a simultaneous shift to higher angle was observed compared with peaks of pure Bi (JCPDS 01-085-1331). The peak split was not observed. These results confirm the solid solution formation for the Bi-Sb phase and volume reduction by the Sb addition. The volume change agrees with the smaller lattice parameters for pure Sb, as shown in Table 5.1.

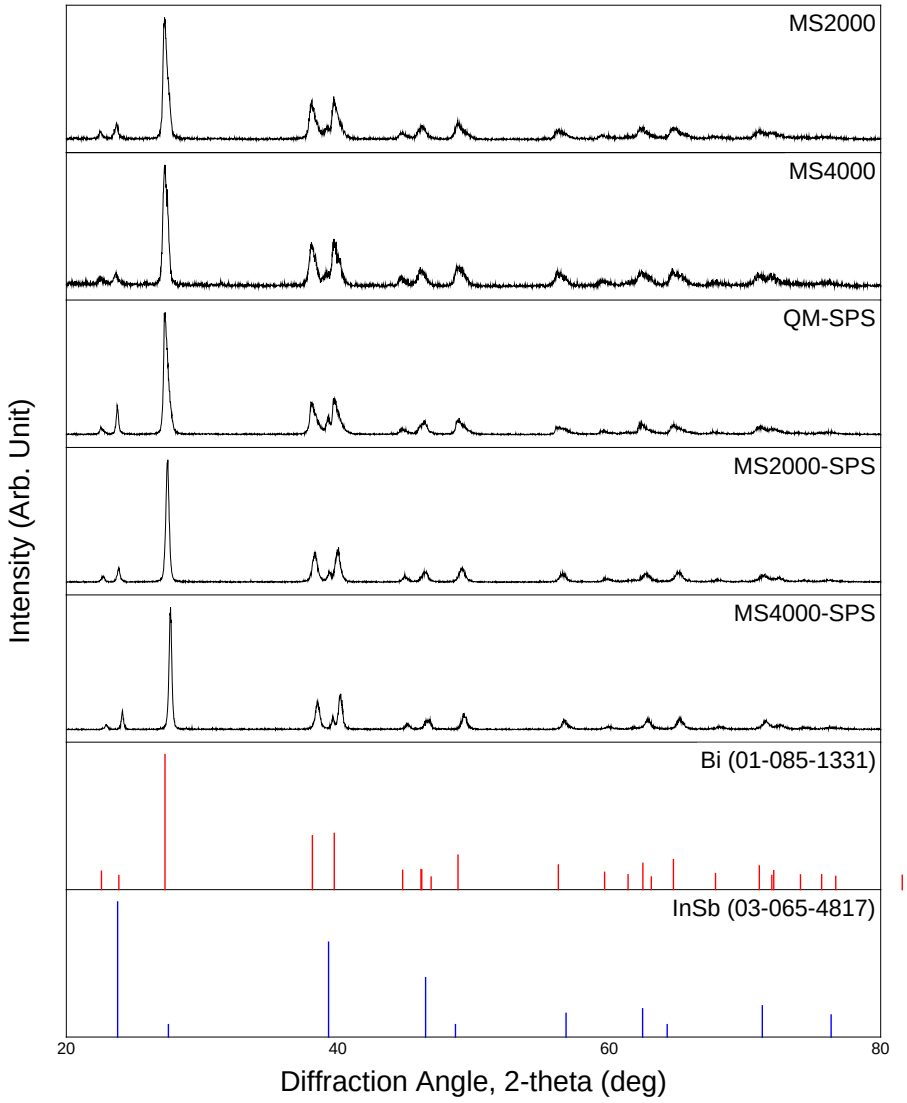

Figure 5.2 Powder XRD pattern of $(Bi_{0.88}Sb_{0.12})_{90}(InSb)_{10}$ samples

The peak width of the XRD pattern is noticeably broadened in the MS2000 and MS4000 samples as compared with the other SPS samples, indicating that melt-spinning technique forms the very fine microstructure. The XRD peaks sharpen for MS2000-SPS and MS4000-SPS, indicating grain growth occurred in the sintering process. Among the sintered samples, peaks for QM-SPS sample was broader and shows tailing. It may be caused by the heterogeneity in the Bi/Sb composition due to the insufficient cooling rate at the fabrication process. The lattice parameters of Bi-Sb phase calculated from the XRD patterns are shown in Table 5.1, which lies between the reference values for pure Bi and Sb [20]. The MS-SPS

samples show smaller lattice parameters than QM-SPS samples. The difference may be affected by the sample heterogeneity as mentioned above. Relative density was estimated from the volume fraction and calculated theoretical density of each phase. The volume fraction of InSb phase is about 18%. The relative densities for composite samples are higher than 97% of the theoretical values.

Table 5.1. Lattice parameters and densities of $(Bi_{0.88}Sb_{0.12})_{90}(InSb)_{10}$ and $Bi_{0.88}Sb_{0.12}$ samples at room temperature. Lattice parameters for pure Bi and Sb are also shown as reference.

Sample	Lattice parameter		Measured density (g/cm3)	Relative density (%)
	a (Å)	*c* (Å)		
QM-SPS	4.527	11.804	8.59	97.6
MS2000-SPS	4.510	11.761	8.68	97.7
MS4000-SPS	4.512	11.590	8.42	97.5
$Bi_{88}Sb_{12}$-QM-SPS	4.526	11.802	9.30	98.5
Bi [20]	4.546	11.862	-	-
Sb [20]	4.308	11.274	-	-

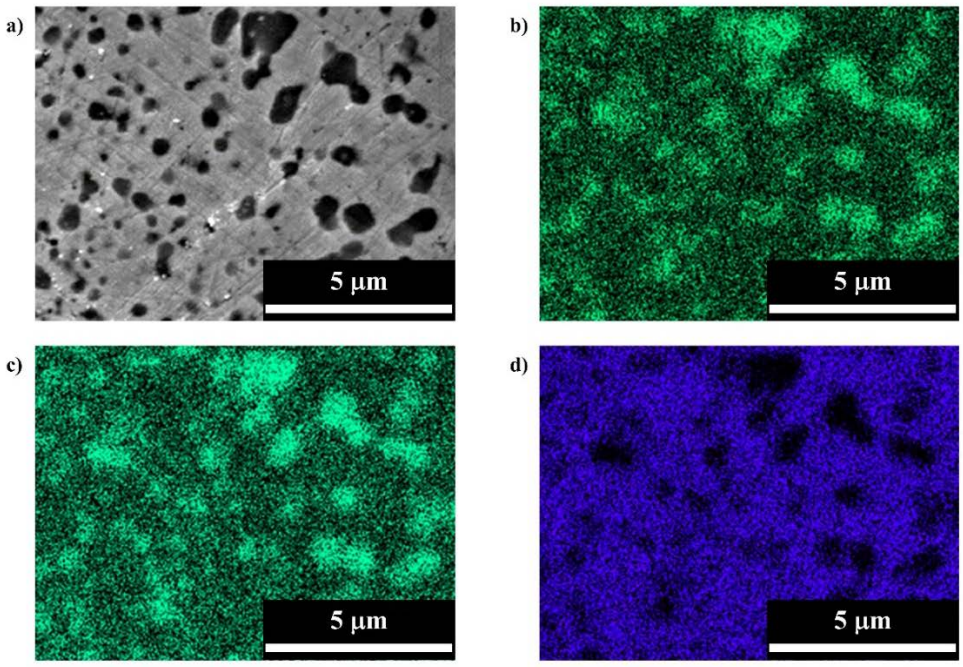

Figure 5.3 Surface image of MS4000-SPS sample: (a) SEM image and EDX mapping images of (b) In, (c) Sb, and (d) Bi, respectively. The white scale bars represent 5 μm

To identify the atomic distribution in the sample, EDS analysis was carried out for MS4000-SPS sample and the images are shown in Fig. 5.3. The Bi-Sb alloy and InSb phases are clearly separated and the elements are homogeneously distributed in each phase. The grey matrix areas in SEM image correspond to Bi-Sb phase and the dark region represents the InSb phase as shown in Fig. 5.3 (a). The microstructure observation confirms Bi-Sb alloy-InSb dual phase structure with spherical InSb embedded in the matrix of Bi-Sb alloy. The eutectic structure shape was determined by the volume fraction, surface tension, growth rate, and so on. The low volume fraction of InSb phase (18% < 28%) may generate that microstructure.

In the SEM images of Fig. 5.4, it is found that the MS2000-SPS and MS4000-SPS samples, which were subjected to melt-spinning, have finer microstructure than of the comparative QM-SPS sample. Although grain growth occurred during the sintering process, the size of InSb particle is 1~2 μm for MS2000-SPS sample and 0.5~1 μm for MS4000-SPS sample. Very fine microstructure was successfully generated by MS-SPS process for the sample at the eutectic composition.

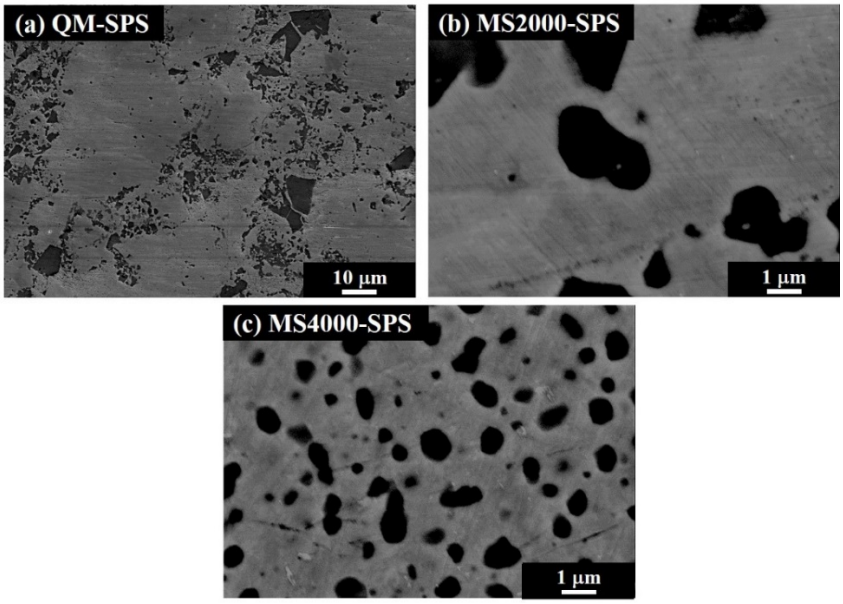

Figure 5.4 Scanning electron micrograph of the $(Bi_{0.88}Sb_{0.12})_{90}(InSb)_{10}$ samples (A) QM-SPS, (b) MS2000-SPS, and (c) MS4000-SPS.

Fig. 5.5 shows the temperature dependence of Seebeck coefficient *S*, electrical resistivity ρ, and power factor *PF* for $Bi_{0.88}Sb_{0.12}$ and $(Bi_{0.88}Sb_{0.12})_{90}(InSb)_{10}$ composite samples. For all the samples and over the entire temperature range, the sign of the *S* is negative

and ρ values increased with increasing temperature. The composite samples have larger absolute S and higher ρ than $Bi_{0.88}Sb_{0.12}$. It would be caused by existence of semiconducting InSb phase, which possess larger S and higher ρ values. The MS-SPS samples exhibited higher ρ values compared with those QM-SPS and reference sample, due to low carrier concentration. By comparing QM-SPS and MS4000-SPS, larger S value is observed for the MS sample. The rapid cooling rate at the MS process could improve the homogeneity in Bi-Sb phase, which increase the band gap and enhance the S value. On the other hand, the enhancement in S is not observed for MS2000-SPS sample, indicating that the cooling rate was insufficient in spite of the MS process. Same tendency was reported previously [15], considerably high cooling rate is needed for the Bi-Sb alloy. The higher cooling rate decreases the InSb particle size as shown in Fig. 5.4, which increases electron-interface scattering. Hence MS samples show higher electrical resistivity than QM-SPS sample. It is notable that *PF* of MS4000-SPS sample is nearly equal to that of QM-SPS in spite of the stronger electron-interface scattering, reached 2.6 mW/mK^2 at 300 K. It indicates that the interfaces between Bi-Sb and InSb phases are clean because natural eutectic phase separation occurs in this fabrication procedure, which maintain the electrical properties as TE materials.

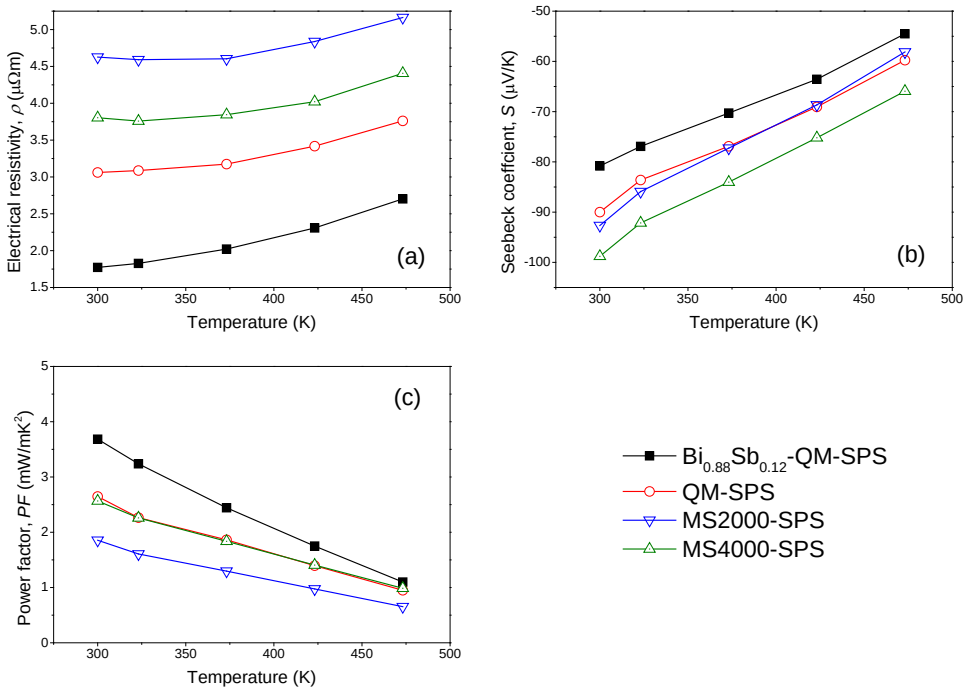

Figure 5.5 Temperature dependence of (a) electrical resistivity, (b) Seebeck coefficient, (c) power factor for $Bi_{0.88}Sb_{0.12}$ and composite samples

Fig. 5.6 shows the temperature dependence of thermal conductivities. The total thermal conductivity was lowered for the composite samples compared to $Bi_{0.88}Sb_{0.12}$. The sample MS4000-SPS has minimum thermal conductivity among the samples, 30-35% lower than Bi-Sb alloy. Electronic thermal conductivity was calculated using the Wiedemann-Franz law $\kappa_e = L \cdot \rho^{-1} \cdot T$, where L is the Lorenz number. Lorenz number depends on the Fermi level, hence estimated from the Seebeck coefficient. The values of around 2×10^{-8} $W \cdot \Omega \cdot K^{-2}$ are used. κ_l was obtained by subtracting κ_e from κ. The sample MS4000-SPS shows lower κ than other composite samples due to the fine microstructure, which provide frequent phonon-interface scattering. Nevertheless, the composite samples have higher lattice thermal conductivities than $Bi_{0.88}Sb_{0.12}$ alloy. It would be caused by the high thermal conductivity of InSb phase, around 18 W/mK at room temperature [14]. Further refining is needed to enhance the phonon-interface scattering and ignore the high thermal conduction in InSb phase.

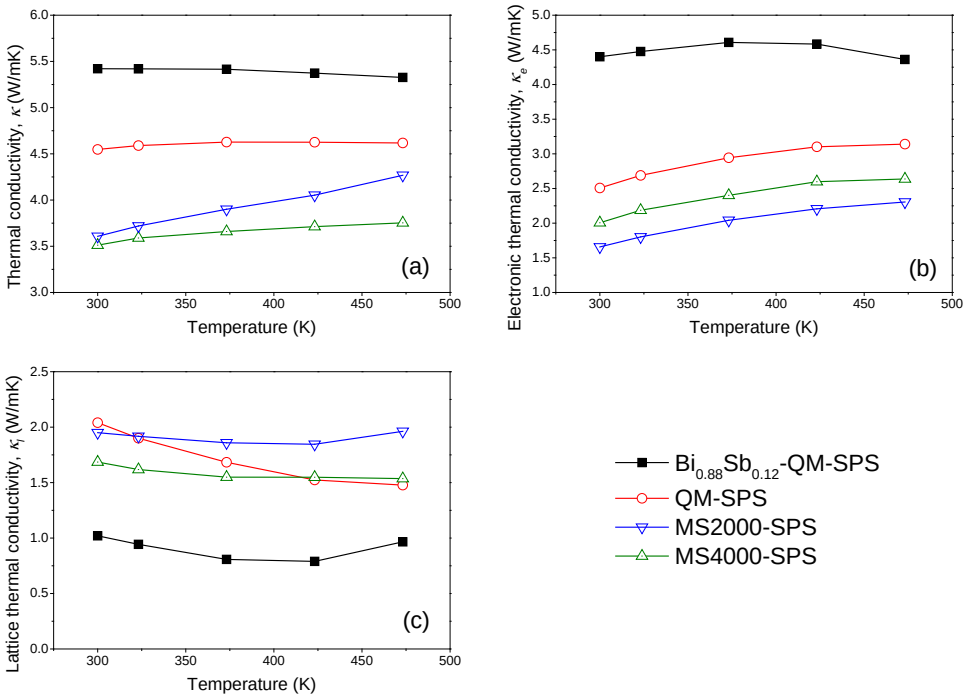

Figure 5.6 Surface image of arc-melted sample: (a) SEM image and EDX mapping images of (b) Si, (c) Cr, and (d) Mn, respectively. The white scale bars represent 10 μm

The temperature dependence of *ZT* in each sample is shown in Fig. 5.7. MS4000-SPS sample shows the highest *ZT* among other samples in entire temperature range. The *ZT*

decreases with temperature, the maximum value of 0.23 is obtained at room temperature. By comparison with QM-SPS sample, the *ZT* value improves by about 25% in all temperature range. It is achieved by reduction of thermal conductivity without degradation of power factor. It indicates that this microstructure refining technique, using liquid quenching and phase separation at the eutectic composition, is promising method to improve the *ZT* value. On the other hand, the *ZT* value is almost same as that for $Bi_{0.88}Sb_{0.12}$ alloy. Appropriate materials selection and more rapid cooling rate are needed to achieve further improvement of thermoelectric performance.

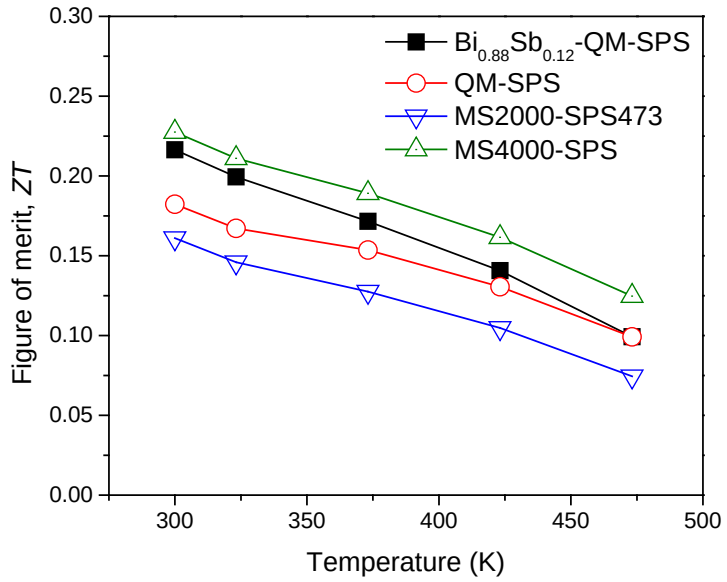

Figure 5.7 Temperature dependence of *ZT* for $Bi_{0.88}Sb_{0.12}$ and composite samples

5.4 Conclusion

We successfully fabricated $Bi_{0.88}Sb_{0.12}$/InSb eutectic alloy and their microstructure and thermoelectric properties were investigated. The power factor reached a maximum value of 2.6 mW/mK^2 at 300 K for the MS4000-SPS sample. Although the *ZT* is as same as the eutectic-free Bi-Sb matrix with the value of 0.23 at 300 K, we could reduce the thermal conductivity by 35%. Furthermore the thermal conductivity reduces while maintaining the power factor for the composite samples. Combination of rapid cooling by melt spinning and eutectic-phase separation is a promising method to synthesize high performance thermoelectric composites as the results is almost the same as previous Si study.

5.5 References

[1] Wolfe R and Smith G E 1962 EFFECTS OF A MAGNETIC FIELD ON THE THERMOELECTRIC PROPERTIES OF A BISMUTH-ANTIMONY ALLOY *Appl. Phys. Lett.* **1** 5–7

[2] Yim W M and Amith A 1972 Bi-Sb alloys for magneto-thermoelectric and thermomagnetic cooling *Solid. State. Electron.* **15** 1141–65

[3] Lenoir B, Demouge A, Perrin D, Scherrer H, Scherrer S, Cassart M and Michenaud J P 1995 Growth of Bi1 − xSbx alloys by the traveling heater method *J. Phys. Chem. Solids* **56** 99–105

[4] Lenoir B, Cassart M, Michenaud J P, Scherrer H and Scherrer S 1996 Transport properties of Bi-RICH Bi-Sb alloys *J. Phys. Chem. Solids* **57** 89–99

[5] Zemskov V ., Belaya A ., Beluy U . and Kozhemyakin G . 2000 Growth and investigation of thermoelectric properties of Bi–Sb alloy single crystals *J. Cryst. Growth* **212** 161–6

[6] Kitagawa H, Noguchi H, Kiyabu T, Itoh M and Noda Y 2004 Thermoelectric properties of Bi–Sb semiconducting alloys prepared by quenching and annealing *J. Phys. Chem. Solids* **65** 1223–7

[7] Zemskov V ., Belaya A ., Beluy U . and Kozhemyakin G . 2000 Growth and investigation of thermoelectric properties of Bi–Sb alloy single crystals *J. Cryst. Growth* **212** 161–6

[8] Brochin F, Devaux X, Ghanbaja J and Scherrer H 1999 Study of BiSb-SiO2 nanocomposite powders produced by an arc plasma processing *Nanostructured Mater.*

11 1–8

[9] Devaux X, Brochin F, Martin-Lopez R and Scherrer H 2002 Study of the microstructure influence on the transport properties of Bi86.5Sb13.5 polycrystalline alloy *J. Phys. Chem. Solids* **63** 119–25

[10] Martin-Lopez R, Lenoir B, Devaux X, Dauscher A and Scherrer H 1998 Mechanical alloying of BiSb semiconducting alloys *Mater. Sci. Eng. A* **248** 147–52

[11] Luo T, Wang S, Li H and Tang X 2013 Low temperature thermoelectric properties of melt spun Bi85Sb15 alloys *Intermetallics* **32** 96–102

[12] Norizan M N, Kurimoto T, Miyazaki Y, Ohishi Y, Kurosaki K and Muta H 2018 Fabrication and thermoelectric property of nanostructured Si/Cr 0.8 Mn 0.2 Si 2 eutectic alloy by melt-spinning *Mater. Res. Express* **6** 025702

[13] Yamaguchi S, Matsumoto T, Yamazaki J, Kaiwa N and Yamamoto A 2005 Thermoelectric properties and figure of merit of a Te-doped InSb bulk single crystal *Appl. Phys. Lett.* **87** 201902

[14] Zhang Q, Xiong Z, Jiang J, Li W, Xu G, Bai S, Cui P and Chen L 2011 Enhanced thermoelectric performance in In1−xGaxSb originating from the scattering of point defects and nanoinclusion *J. Mater. Chem.* **21** 12398

[15] Maciá-Barber E 2015 *Thermoelectric Materials - Advances and Applications* (Pan Stanford)

CHAPTER VI

Conclusion

6.1 Summary

In this thesis, the behavior of eutectic compound were investigated. Polycrystalline sample of *p*-type Si/$CrSi_2$, *n*-type Si/$Cr_{0.8}Mn_{0.2}Si_2$, and *n*-type $Bi_{0.88}Sb_{0.12}$/InSb eutectic alloy were successfully prepared by melt-spinning based rapid solidification technique. The high density samples were done by spark plasma sintering process. The thermoelectric properties have been investigated from room temperature at 300 K to around 473 K ~ 773 K.

Firstly in chapter III, we demonstrated the fabrication of *p*-type Si/$CrSi_2$ eutectic alloy based on a self-assembly process. The size of the eutectic microstructure are reduced to the nanometer scaled by using melt-spinning technique. It is noted that the lamellar structure has high stability upon solidification, so that no transition to an amorphous phase occurs. The average eutectic spacing of the samples increases with a decrease in the wheel speed. In a sample melt-spun at less than 10 m/s, virtually no aligned lamellar structure can be observed instead, a micrometer-sized structure with disordered interfaces is dominant. It is demonstrated that the thermal conductivity can be reduced to 1/3 that of the bulk eutectic alloy of the same composition, thus increasing *ZT*. The power factor does not decrease but rather increases significantly at higher temperatures.

Secondly in chapter IV, we successfully sintered the ribbon sample with spark plasma sintering process and convert the conduction type of *p*-type Si/$CrSi_2$ eutectic alloy to *n*-type conduction by doping Si with phosphorous and substitution of chromium atom with manganese. Although grain growth occurred during the sintering, the microstructure of MS-SPS sample was successfully refined by about 1/10 than AM-SPS sample. It may be explained by difference in density of interface between Si and silicide phases. The interfacial states provide electronic carriers, and the interfacial barrier potentials scatters the carriers. Because the MS samples have very high interface density, the carrier concentration and scattering rate are high, consequently they show lower Seebeck coefficient value and higher electrical

resistivity. Although the size of the morphology change to about 100 nm to 200 nm during sintering process, a fine nanostructure was obtained in the bulk sample MS-SPS. The power factor was reduced in as-cast melt-spun ribbon sample, but it recovered by following sintering process. It is demonstrated that thermal conductivity were reduced by 20%–30% by the structure refinement which are not as expected. As a result, ZT value was improved about 50% compared to arc-melted sample.

Finally in chapter V, we investigated system with other than Si and silicide which is the *n*-type BiSb/InSb. The submicrometer-sized composites were successfully obtained. Although, the structure can reduce the thermal conductivity by 35% and slightly increase *ZT* value but the reduction of the thermal conductivity are not as expected. This confirm that the novel idea of new fabrication technique can be apply to various thermoelectric material systems.

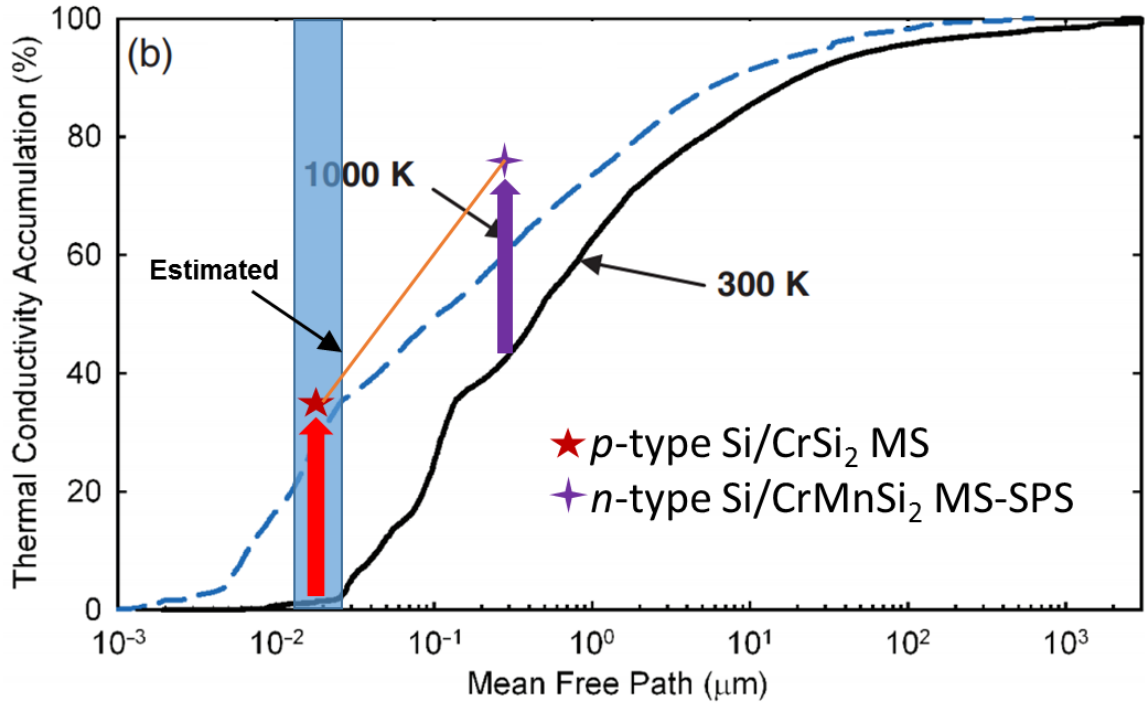

Figure 6.1 Percentage of thermal conductivity accumulation of theoretical Si at 300 K and 1000 K from A. Heng et. al. and current study.

Through these studies, we confirmed that thermal conductivity can be reduced while preserving the electrical properties using both melt-spinning rapid solidification technique and eutectic phase separation. One more important challenge in the same direction is the use of non-toxic and abundant materials that can be easily implemented in the actual consumer device. Although this approach has made great progress, higher efficiencies and lower manufacturing

costs are required. There is still room for new and disruptive developments in the field of thermoelectricity in this young research area.

6.2 Future Work

Fine nanostructure composites was obtained from the new fabrication method. However detailed electron microscopy indicates that grain growth occur in bulk sample during sintering. In the future, I consider that further improvement may be achieved by: 1) reduction of the nanostructure sizes down to ≤ 10 nm for 80-90% thermal conductivity reduction since the trend of accumulated thermal conductivity reduction of current alloy is lower than theoretical value as shown in Fig. 6.1, 2) optimizing the sintering condition to reduce the grain growth and 3) considering the coherent interface including low potential barrier.

Acknowledgement

I would like to express my gratitude to Professor Emeritus Shinsuke Yamanaka for his helpful advices, instructive support, kind guidance and valuable counsels on my study. I am grateful to have Associate Professor Dr. Hiroaki Muta as my supervisor for providing me instructive supports, patient guidance, insightful discussions and suggestions on my study during my Ph.D study. I would also like to thank Associate Professor Dr. Ken Kurosaki and Dr. Yuji Ohishi for their kind help and constructive comments. My sincere thank is expressed to the thesis committee, Professor Dr. Takao Yamamoto and Professor Dr. Takanori Kitada for their helpful suggestions on the present thesis. I thank Mrs. Mayumi Kashi and Mrs. Sumiko Furutani sincerely, for their kind help of dealing with all kinds of things in the lab.

My thankfulness is also extended to Ministry of Higher Education Malaysia and Universiti Malaysia Perlis who provide me the scholarship during my study in Japan. Not forgotten, all members in the laboratory for their helpful advice and encouragement in my student life. Finally, I would like to thank my family for their patience and great support in countless ways.

Research Achievements

Publication

1. **The Nanometer-Sized Eutectic Structure of Si/$CrSi_2$Thermoelectric Materials Fabricated by Rapid Solidification**
   Journal of Electronic Materials, **47,** 2330–6 (2018)
   Mohd Natashah Norizan, Yoshinobu Miyazaki, Yuji Ohishi, Hiroaki Muta, Ken Kurosaki, Shinsuke Yamanaka

2. **Fabrication and Thermoelectric Property of Nanostructured Si/$Cr_{0.8}Mn_{0.2}Si_2$ Eutectic Alloy by Melt-Spinning**
   Materials Research Express, **6,** 025702 (2018)
   Mohd Natashah Norizan, Takahito Kurimoto, Yoshinobu Miyazaki, Yuji Ohishi, Ken Kurosaki, Hiroaki Muta

3. **Fabrication and thermoelectric property of $Bi_{0.88}Sb_{0.12}$/InSb Eutectic Alloy by Melt Spinning and Spark Plasma Sintering**
   Material Transactions (Under review)
   Mohd Natashah Norizan, Yuji Ohishi, Ken Kurosaki, Hiroaki Muta

Domestic Conference

1. **Improved Thermoelectric Properties of Bismuth-Magnesium Eutectic Alloy by Melt Spinning and Spark Plasma Sintering**
   14th Annual Meeting of The Japan Society of Thermoelectronics Academic Conference (TSJ 2017)

International Conference

1. **Improved Thermoelectric Properties of Bismuth-Magnesium Eutectic Alloy by Melt Spinning and Spark Plasma Sintering**
   2018 TMS Annual Meeting & Exhibition (TMS 2018)

2. **Fabrication and Thermoelectric Properties of InSb/Bi Eutectic Alloy by Melt Spinning and Spark Plasma Sintering**
   5th Southeast Asia Conference on Thermoelectrics (SACT2018)

Award

1. Best Oral Presenter Award **at 5th Southeast Asia Conference on Thermoelectrics (SACT2018)**